

August 2013

Modeling, Analyses and Assessment of Microgrids Considering High Renewable Energy Penetration

Qiang Fu

University of Wisconsin-Milwaukee

Follow this and additional works at: <https://dc.uwm.edu/etd>



Part of the [Electrical and Electronics Commons](#)

Recommended Citation

Fu, Qiang, "Modeling, Analyses and Assessment of Microgrids Considering High Renewable Energy Penetration" (2013). *Theses and Dissertations*. 248.

<https://dc.uwm.edu/etd/248>

This Dissertation is brought to you for free and open access by UWM Digital Commons. It has been accepted for inclusion in Theses and Dissertations by an authorized administrator of UWM Digital Commons. For more information, please contact open-access@uwm.edu.

**MODELING, ANALYSES AND ASSESSMENT OF
MICROGRIDS CONSIDERING HIGH RENEWABLE
ENERGY PENETRATION**

by

Qiang Fu

A Dissertation Submitted in
Partial Fulfillment of the
Requirements for the Degree of

Doctor of Philosophy
in Engineering

at

The University of Wisconsin-Milwaukee

August 2013

ABSTRACT

MODELING, ANALYSES AND ASSESSMENT OF MICROGRIDS CONSIDERING HIGH RENEWABLE ENERGY PENETRATION

by

Qiang Fu

The University of Wisconsin-Milwaukee, 2013

Under the Supervision of Prof. David C. Yu

Microgrids are receiving attention due to the increasing need to integrate distributed generations and to ensure power quality and provide energy surety to the customers. Since renewables need to be in the mix for energy surety, a high renewable-energy penetrated microgrid is analyzed in this paper. The standard IEEE 34 bus distribution feeder is adapted and managed as a microgrid by adding distributed generation and load profiles. The 25kV system parameters are scaled down to 12kV and renewable sources including solar PV and wind turbines, an energy storage system, and a natural gas generator have been added to the 34-bus system. The distribution generations (DG) and renewables are modeled in detail

using PSCAD software and practical constraints of the components are considered. The droop control and autonomous control for microgrid normal operation in islanded mode and grid-tied mode have been proposed and studied. A novel comprehensive supervisory control scheme has been defined to manage the microgrid transition from or to the bulk grid, and to minimize the transients on voltage and frequency. Detailed analyses for islanding, reconnection, and black start are presented for various conditions. The proposed control techniques accept inputs from local measurements and supervisory controls in order to manage the system voltage and frequency. The monitoring of the microgrid for measuring power quality and control requirements for DGs and storage are modeled. The power quality issues are discussed and indexes are calculated. A novel probabilistic assessment of microgrid reliability has been proposed. At last, several extended researches are presented. An experimental system has been built which includes three 250kW inverters emulating natural gas generator, energy storage, and renewable source. The simulation and experimental results are provided which verifies the analytical presentation of the hardware and control algorithms.

© Copyright by Qiang Fu, 2013
All Rights Reserved

DEDICATION

*Dedicated to my parents and my wife
for their infinite love, support, and encouragement*

ACKNOWLEDGEMENTS

As I reflect on my PhD journey at University of Wisconsin - Milwaukee (UWM), I am reminded of countless support and blessing from my advisors, colleagues, friends, and my family, for whom I am most thankful.

I must first express a heartfelt appreciation to my major advisor Dr. David Yu for devoting his time and attention to this effort. His guidance and support have always helped me to think innovatively and work out difficulties. I sincerely appreciate for all those great discussions and conversations which have been invaluable. I would also like to specifically thank my co-advisors Dr. Adel Nasiri and Dr. Vijay Bhavaraju, for all their support, direction, and advice. Without them, this dissertation would not have been possible to be accomplished. Their broad knowledge on the aspects of research and development of power electronics tremendously improved the quality of the work. They have taught me how to be a researcher as well as an engineer. Special thanks as well to other committee members Dr. Chiu Tai Law and Dr. Hossein Hosseini. Thanks all for their precious time and valuable questions and suggestions.

Additionally, I would like to thank all my friends and colleagues for their insightful ideas, advices, and interest in my work. Special recognition is in order to Ashish Solanki, Luis Montoya, Tiefu Zhao, Yakov Familiant, Zeljko Jankovic, Carl Westerby, and Gary Huang.

Finally, I would extend a heartfelt thank you to my parents and my wife for their unconditional love, support, and encouragement.

Contents

List of Figures	x
List of Tables	xvii
1 Introduction	1
1.1 Research Background	1
1.1.1 Drivers Behind Microgrids	2
1.1.2 Benefits and Barriers	4
1.1.3 Microgrids Under Development	5
1.2 Scope and Objectives	8
2 Microgrid Configuration	10
2.1 Introduction of IEEE 34-Bus Distribution System	11
2.2 Scaling of IEEE 34-Bus Distribution System	12
2.2.1 Lumped Line Impedance	12
2.2.2 Distributed Line Impedance	13
2.3 Microgrid Components	14
2.4 Power Profiles and Capacity Sizing of Generations and Loads	16
2.5 Summary of Proposed Microgrid	20
3 Modeling of Microgrid Components	21
3.1 Wind Turbine	22

3.2	Solar PV	28
3.3	Natural Gas Generator	34
3.4	Zinc-Bromide Energy Storage System	39
3.5	General-Purpose Inverter	46
3.6	Other Basic Components	48
4	Microgrid Operation and Management	51
4.1	Power Management For Renewable Energy	52
4.2	Autonomous Control for Microgrid in Grid-tie Mode	62
4.3	Droop Control for Microgrid in Island Mode	67
4.4	Supervisory Control for Microgrid Transitions Using Low Bandwidth Communication	77
4.4.1	An Overview of the Proposed Supervisory Control Scheme . .	77
4.4.2	Matlab Interface Designed for PSCAD	82
4.4.3	Microgrid Islanding	85
4.4.4	Microgrid Reconnection	99
4.4.5	Microgrid Black Start	103
5	Power Quality and Reliability Assessment	105
5.1	Power Quality Definition	106
5.2	Power Quality Assessment	107
5.3	Probabilistic Load Flow for Microgrid Reliability Assessment	111
5.3.1	Data Based PLF Assessment	111
5.3.2	Model Based PLF Assessment	118
6	Extended Research	144
6.1	Modeling of Fort Sill Microgrid	145
6.2	Modeling of Extended FSMG	151

6.3 Testing of A 1MW Multi-Inverter Based Microgrid	157
7 Conclusion	163
References	165
Curriculum Vitae	171

List of Figures

2.1	One-line diagram of IEEE 34 bus test system.	11
2.2	Scaling of lumped line impedance for line 302	13
2.3	Scaling transmission lines with distributed line impedance, (a) original case, (b) Impedance reduced in half, (c) line length is reduced to half, and (d) line length is reduced to half and capacitance is quadrupled.	14
2.4	A typical microgrid backbone diagram	15
2.5	Load power profile for a single day	17
2.6	The power profile for a 250kW solar PV plant.	17
2.7	The power profile for a 750kW wind turbine.	18
2.8	The configuration of proposed microgrid using IEEE 34 bus test system.	20
3.1	One line diagram of a 2 mile long cable with uniform distribution	23
3.2	A 750kW wind turbine model with cut-in and cut-out functions.	27
3.3	Simulation results for 750kW HAWT using 24 hours real data.	27
3.4	Wind speed vs. Output power	28
3.5	A more complex equivalent circuit for a PV cell	29
3.6	Series and parallel resistances in the PV equivalent circuit	30
3.7	The I-V curve and power output for a PV module. At the maximum power point the module delivers the most power that it can under the conditions of sunlight and temperature for which the I-V curve has been drawn.	31

3.8	The PV array and MPPT function in PSCAD.	32
3.9	The I-V curve of 25kW PV array.	33
3.10	The waveforms of solar irradiation profile, PV output power and terminal voltage at MPPT in a perfect day.	33
3.11	The waveforms of solar irradiation profile, PV output power and terminal voltage at MPPT in a cloudy day.	34
3.12	The basic block diagram of a natural gas generator	35
3.13	The block diagram of AC8B AC exciter.	36
3.14	The model of 1.5MVA natural gas generator in PSCAD.	37
3.15	Simulation results for the natural gas generator in off-grid operation when load steps are applied at 10s and 20s: from top, Real (blue in MW) and reactive power (green in MVar), terminal voltage (pu), and rotor speed (pu).	38
3.16	simulation results for the natural gas generator in grid-tie operation when power command steps are applied at 10s and 20s: from top, Real (blue in MW) and reactive power (green in MVar), terminal voltage (pu), and rotor speed (pu).	39
3.17	Three basic types of modeling of battery.	41
3.18	The electrical model of ZESS.	42
3.19	The ZESS model in PSCAD.	43
3.20	The waveform of charging current.	44
3.21	The waveform of state of charge in percentage.	44
3.22	The waveforms of OCV and terminal voltage.	44
3.23	The curve of OCV versus SOC.	45
3.24	The curve of Rs versus SOC.	45
3.25	The block diagram of the controls for voltage and frequency of storage inverter.	47

3.26	The proposed inverter model in PSCAD.	48
3.27	The model of variable load in PSCAD.	49
3.28	The model of regulator in PSCAD.	50
4.1	The one-line diagram of an example distributed system with adding a renewable energy generation via line impedance.	52
4.2	The power profile of the 500kW PV solar.	55
4.3	The per unit voltage at PV terminal.	55
4.4	The real and reactive power received from the grid.	56
4.5	The solar PV power profile after real power curtailment applied.	57
4.6	The per unit voltage at PV terminal after power curtailment.	57
4.7	Active and reactive power received from the grid after power curtailment.	58
4.8	The managed real and reactive power profile of solar PV.	59
4.9	The per unit voltage at PV terminal after power curtailment and reactive power control.	59
4.10	Real and reactive power received from the grid after power curtailment and reactive power control.	59
4.11	The results for wind power and bus voltage without wind power curtailment: from top, turbine active and reactive power, bus voltage, and wind speed.	60
4.12	The results for wind power and bus voltage with wind power curtailment: from top, turbine active and reactive power, bus voltage, and wind speed.	61
4.13	The results for wind power and bus voltage with wind power curtailment and reactive power control: from top, turbine active and reactive power, bus voltage, and wind speed.	62
4.14	The real and reactive power of the solar PV in grid-tie mode.	64

4.15	Voltages at renewable source buses in grid-tie mode.	65
4.16	The real and reactive power of the wind turbine on bus 840 in grid-tie mode.	65
4.17	The real and reactive power delivered by the grid to the system. . . .	66
4.18	Voltage profile at bus 822 of the system during grid-tie mode.	66
4.19	The real power droop mechanism for natural gas generator and battery in the microgrid.	68
4.20	The reactive power droop mechanism for natural gas generator, solar PV and battery in the microgrid.	69
4.21	The real and reactive power delivered by 0.25MW solar PV.	70
4.22	The real and reactive power delivered by one of the 750kW wind turbines.	71
4.23	The real and reactive power delivered by two 250kW battery storage systems.	71
4.24	The real and reactive power delivered by 1.5MVA natural gas generator.	72
4.25	Voltage profile at bus 822 of the system.	72
4.26	Voltage profile of all sources in the system.	73
4.27	The real power, reactive power, voltage, and frequency of	74
4.28	Voltage profile of sources when a regulator is added	75
4.29	Voltage profile of bus 822 when a regulator is added to the system . .	76
4.30	Voltage profile of sources when storage is moved to bus 832.	76
4.31	Total generation, load, and loss in the system when storage is moved to bus 832.	76
4.32	The diagram of proposed supervisory control scheme.	78
4.33	The flow chart of supervisory control unit.	79
4.34	The proposed data format for the signal transmitted from SCU to natural gas generator.	80
4.35	An example of Matlab interface module in PSCAD.	82

4.36	The result power waveform returned by Matlab and plotted in PSCAD.	83
4.37	Screenshot of the parameters setting for Matlab interface module. . .	83
4.38	Screenshot of the configuration window for Matlab interface module. .	84
4.39	The block diagram of the controls for voltage and frequency of storage inverter.	86
4.40	The block diagram of frequency and voltage controls for natural gas generator.	87
4.41	The general algorithm for microgrid intentional islanding.	89
4.42	Real and reactive power delivered by grid, natural gas generator . . .	90
4.43	Profiles of voltage at source buses and frequency during	91
4.44	Real and reactive power delivered by the grid and five sources	93
4.45	Profiles of voltage at source buses and frequency during	93
4.46	Unintentional islanding: total load (including losses) and	95
4.47	Profiles of voltage at source buses and frequency during	97
4.48	Unintentional islanding: total load (including losses) and	98
4.49	Profiles of voltage at source buses and frequency during	98
4.50	The shifting droop control diagram for active power and	99
4.51	Waveforms of power delivered by grid, natural gas generator	100
4.52	Frequencies of the main grid and microgrid during reconnection. . . .	101
4.53	Instantaneous angle (Phase A) of the main grid and microgrid	102
4.54	Real power of total load, battery and natural gas generator.	104
4.55	Waveforms of voltage and frequency at PCC.	104
5.1	Histogram of voltage at bus 822.	112
5.2	The cumulative distribution of voltage at bus 822.	113
5.3	Column chart of case 1.	116
5.4	Column chart of case 2.	117

5.5	Column chart of case 3.	117
5.6	VESTAS V82 wind turbine power curve.	121
5.7	Wind farm modeling by Monte Carlo and 5PEM	129
5.8	The results comparison between MC and 5PEM	130
5.9	The comparison of CDF of bus 38 voltage magnitude before and after VAR compensation.	131
5.10	Bivariate distribution model for wind farms	132
5.11	The CDF comparison between dependent and independent situation.	133
5.12	The comparison of cumulative distribution of voltage at bus 822 in three cases.	139
5.13	The column chart of case 1.	142
5.14	The column chart of case 2.	142
5.15	The column chart of case 3.	143
6.1	The one-line diagram of Fort Sill Microgrid.	146
6.2	Measured wind speed data and corresponding power delivered by wind turbine.	147
6.3	Measured solar irradiation data and corresponding power delivered by Solar PV.	147
6.4	Real and reactive power delivered by natural gas generator, battery, wind turbine and Solar PV.	148
6.5	Waveforms of system voltage and frequency.	149
6.6	Real power delivered by grid, battery and natural gas generators (upper);	150
6.7	The microgrid and bulk grid frequencies (upper);	150
6.8	Real power delivered by grid, battery and natural gas generators (upper);	150
6.9	The microgrid and bulk grid frequencies (upper);	150
6.10	The schematic of extended Fort Sill Microgrid.	152

6.11	Power curves during islanding with 200kW opening power.	153
6.12	Voltage at 13.2kV feeder.	154
6.13	System frequency.	154
6.14	Power curves during islanding with 550kW opening power.	155
6.15	Voltage at 13.2kV feeder.	155
6.16	System frequency.	155
6.17	Diagram of power flow between FSMG and WWTP via AC flex-bus inverter.	156
6.18	Real power delivered by AC flex-bus inverter and WWTP, and local load within FSMG.	156
6.19	A picture of the test setup, synchronizer and passive loads for the experimental setup.	158
6.20	The schematic of the experimental test setup.	159
6.21	Traces of microgrid frequency and output power of energy storage and renewable during unintentional islanding when transitioning from grid-tie to island mode.	160
6.22	Instantaneous waveforms for voltage, load current (red), and grid current (light blue) during unintentional islanding.	161
6.23	Traces of microgrid voltage, frequency, and generator and storage power in black start moving to island and grid tie modes.	162
6.24	Microgrid operation from black start to island mode under step loading conditions.	162

List of Tables

3.1	The key parameters of PV array	31
3.2	The key parameters of PV array	35
3.3	The comparison of properties of Zinc-Bromide battery	40
3.4	The settings for regulators and compensators.	50
4.1	The true table of commands for natural gas generator.	81
5.1	Power quality parameters for three cases	109
5.2	Summary of classified probabilities of selected bus voltages in case 1 .	114
5.3	Summary of classified probabilities of selected bus voltages in case 2 .	115
5.4	Summary of classified probabilities of selected bus voltages in case 3 .	116
5.5	Parameters of two wind farms	128
5.6	RMS error between MC and 5PEM	130
5.7	25 point distribution of two dependent wind turbines	134
5.8	Summary of classified probabilities of selected bus voltages in case 1 .	140
5.9	Summary of classified probabilities of selected bus voltages in case 2 .	140
5.10	Summary of classified probabilities of selected bus voltages in case 3 .	141
6.1	Parameters of 240kVA natural gas generator used in FSMG	146
6.2	List of capacities of main components within EFSMG	151
6.3	Power delivered by WWTP, FSMG and Grid before and after islanding	154
6.4	Power delivered by WWTP, FSMG and Grid before and after islanding	154

Chapter 1

Introduction

1.1 Research Background

Over the past few decades, energy has played an increasingly important role in the technological and economic development. The global electrical energy demand is seen to be increasing in recent years and it is expected to double in the next 20 years [1]. Fossil fuels that have been used as a source of energy till date are rapidly depleting requiring us to look towards more alternative sources of energy. Wind and Solar PV are two of the major alternative sources of energy being utilized in many parts of the world [2].

According to American Wind Energy Association (AWEA) as of September 2012, the total installed wind power capacity was at 51,630 MW in the U.S. The U.S. government has a vision to generate 20% of electricity using wind energy by 2030 [3–5]. Solar PV is also a large source of renewable energy and the U.S. now has over

6,400 MW of installed solar electric capacity, which is enough to power more than 1 million average American households [6]. However on the other hand, U.S. relies on an aging electrical grid and pipeline distribution systems, some of which originated in the 1880s. The U.S. grid was graded a low score of D+ by the American Council of Civil Engineers in 2013 [7]. Integration of renewable energy and DGs will support better utilization of the existing systems, reduce consumption of fossil based fuels, reduce transmission and distribution losses, and improve voltage quality. However, higher penetration of DGs creates technical and non technical issues which include power quality, power surety, reliability, power management, overall system efficiency, interconnection of grid and regulations [8, 9]. Ongoing generation, transmission and distribution permitting issues, weather related events, and limited maintenance have contributed to an increasing number of failures and power interruptions. They are some of the driving forces behind the microgrid concept [10–13]. Transmission constraints requiring supplies closer to loads, lower cost of solar PV installations, energy storage and natural gas and military demand for more energy surety and security are several other driving factors.

1.1.1 Drivers Behind Microgrids

A microgrid provides a solution to manage DGs and renewable energy and it has ability to maximize the overall system efficiency, power quality and power surety to

critical loads. Microgrid is a cluster of DGs, renewables and local loads connected to the utility grid. Microgrid can operate in parallel to the grid or as an island. The most compelling feature of a microgrid is the ability to separate and isolate itself from the utility's distribution system unintentionally during events (i.e., faults, voltage collapses, black-outs). It may also intentionally disconnect during grid maintenance and also when the quality of power from the grid falls below certain standards. Microgrid can be reconnected to the utility grid without any interruption once the utility is recovered.

There are several technical drivers behind the idea of microgrids, including (i) transmission constraints requiring supplies closer to loads [13], (ii) demand for improved power reliability, efficiency, and quality, [14] (iii) demand for energy security, [15] (iv) integration of renewable energy and DER, (v) military demand for enhanced energy security: Surety, Survivability, Supply, Sufficiency, and Sustainability [16], and (vi) overall systems efficiency (e.g. use of generation waste heat in a combined heat and power installation) [17]. In addition, the lower costs of solar PV installations, natural gas, and energy storage devices have been supporting further expansion of distributed generations and microgrids.

1.1.2 Benefits and Barriers

The distribution system will continue to play a primary role in grid evolution due to its size, value, diversity and direct interface with the customer. The microgrid concept enables the distribution system to operate in a coordinated fashion to support customer with high level of power quality and reliability. A market estimation made by DOE indicates that microgrids can attain a 5.5GW market in 2020 [18] and deliver approximately \$1 billion in public benefits.

An envisioned microgrid is providing added value to society, the grid, and to customers by [19]: 1) improving reliability, 2) reducing the cost of energy and managing price volatility, 3) Assisting in optimizing the power delivery system, including the provision of services, 4) Providing different levels of service quality and value to customers segments at different price points, 5) Helping to manage the intermittency of renewables, 6) Promoting the deployment and integration of energyefficient and environmentally friendly technologies, and 7) Increasing the resiliency and security of the power delivery system by promoting the dispersal of power resources.

However, some technical and non-technical barriers must be overcome to provide these benefits. The greatest challenge from technical side is on the monitoring, control, and protection areas. A high efficient and reliable supervisory and monitoring system has to be developed to accommodate a wide range of load and generation

change. The communication and information layers play a critical role of supervisory management of microgrids. Other technical challenges include: microgrid sizing and planning, steady-state and dynamic performance, utility system and equipment upgrades, interconnection requirements, and so on.

Additionally, to ensure microgrids operate as legal entities, regulatory barriers need to be resolved [20], including 1) regulatory policies, 2) microgrid ownership models, 3) choice of voltage level, 4) the legality of microgrids, 5) service territories, 6) utility tariffs, and 7) environmental and siting laws.

1.1.3 Microgrids Under Development

Several microgrid projects are currently under research and development in the U.S., including the 100kW Consortium for Electric Reliability Technology Solutions (CERTS) microgrid test bed near Columbus, OH [12]; the 3 MW Santa Rita correctional facility test site in Alameda County, CA [21], the Smart Power Infrastructure Demonstration for Energy Reliability and Security (SPIDERS) microgrids [22], the 700kW Fort Sill microgrid project [23], and the Illinois Institute of Technology's Perfect Power System [24]. The CERTS microgrid test bed uses one of the advanced control techniques to perform seamless islanding and reconnection and apply peer-to-peer and plug-and-play concept for devices. One of the goals of the SPIDERS program is to provide reliable backup power during emergencies by integrating renewables and

other distributed generation sources into the microgrid and to ensure that critical operations can be sustained during prolonged utility power outages. In the Fort Sill microgrid project, the objective is to demonstrate a field-scale, renewables-focused, intelligent microgrid, which serves critical mission power requirements in a sustainable, reliable, and secure manner. This microgrid includes two natural gas generators, one 500kWh energy storage element, small wind and solar PV systems, various loads, and a static switch.

Other world-wide existing experimental microgrid and test systems are listed as follows [25–28]:

- Boston Bar - BC Hydro, Canada: Radial microgrid driven by two hydro plants with a peak load of 3MW. Controlled by autonomous controller.
- Boralex planned islanding - Hydro Quebec (HQ), Canada: Microgrid formed to facilitate replacement of 40km feeder serving 3000 customers with a peak load of 7MW. The microgrid is served by a thermal power plant and is controlled autonomously.
- Bronsbergen Holiday Park microgrid - Netherland: Mesh type microgrid driven by several PV DGs with central energy storage. The peak generation capacity is 315 kW and the microgrid is centrally controlled.
- The Residential Microgrid of Am Steinweg in Stutensee - German: Mesh type microgrid driven by several PV DGs, CHP with available electric power of 28kW and

a lead acid battery rated at 880 Ah. Agent based control is implemented.

- CESI RICERCA DER test microgrid - Italy: Low voltage(400V) DC radial microgrid is driven by 14kW PV DG, 10kW solar thermal DG, 10kW biomass based CHP DG, 100kW microturbine based CHP DG and 3 different battery energy storage units.the system is also equipped with a flywheel for power quality purposes. Agent based control is implemented.

- Kythnos island microgrid - Greece: Centrally controlled Radial microgrid driven by 12kW PV DG, 53kWh battery bank, and 5 kW diesel DG.

- Microgrid system at National Technical University of Athens (NTUA) - Greece: Laboratory scale microgrid driven by two PV generators, one wind turbine, and battery energy storage. Agent based control is implemented.

- DeMoTec test microgrid system - German: SCADA controlled test microgrid driven by two battery units, two diesel generators and a wind generator.

- University of Manchester microgrid/flywheel energy storage laboratory prototype - UK: 20kVA radial laboratory microgrid prototype driven by a synchronous generator coupled to an induction motor. The system is also equipped with a flywheel connected through an inverter.

- Kyoto eco-energy project (Kyotango project) - Japan: Mesh type centrally controlled microgrid driven by gas turbines totaling 400kW, 350kW of fuel cells, two PV systems and a 50kW small wind turbine.

- Hachinohe project - Japan: Radial centrally controlled microgrid with 5 PV units 130kW in all, 4 wind turbines 20kW in all, and 3 diesel generators rated at 170kW each.
- Microgrid testbed in Hefei University of Technology (HFUT) - China: Mesh type microgrid driven by PV generators, 3-phase wind generation simulators, fuel cell, battery bank, ultra capacitor bank, conventional generators used to simulate small hydro and fossil generators. The system is controlled using an agent based controller.
- The microgrid demonstration project in Xinjiang - China: is built by Mitsubishi, which is a remote microgrid composed of batteries with inverters, PVs and diesel-based microturbines. The operation result shows that the microgrid has attained the control requirement with limited voltage magnitude and frequency fluctuations.

1.2 Scope and Objectives

The primary objective of this research is to model a general-purpose microgrid which can serve as a benchmark for microgrid planning, controls, testing and assessment. The following are the key components of the research:

- In order to accurately study the behavior of the renewable energy systems, natural gas generation, and energy storage systems and their effects on the voltage and frequency in a microgrid, a standard IEEE 34-bus distribution system is adopted

and scaled in order to match the properties of in-building microgrid at Fort Sill, OK.

- Sizing capacities for distributed generations, renewable energies, and energy storage systems is discussed. A 100% penetration level of renewable energy is selected in order to evaluate the impact on the microgrid.

- Detailed modeling of microgrid components in PSCAD is presented, including a 750kW Horizontal Axis Wind Turbine, a 250 solar PV panel, a 1.5MVA natural gas generator, a 250kW Zinc-Bromide energy storage system, a universal voltage/current controlled inverter, transformers/regulators, transmission line/distribution cables, and various types of loads, etc.

- The microgrid operation and management are studied. A supervisory control scheme is proposed to manage microgrid transitions to or from the bulk grid. Several novel techniques and algorithms for microgrid control and operation are proposed. The simulation results as well as experiments results are presented.

- A common used power quality indexes and a novel probabilistic assessment approach are proposed to evaluate and compare the microgrid reliability in different cases.

- Some extended researches are presented. The Fort Sill Microgrid and extended system are modeled and studied. A 1MW multi-inverter based microgrid built at EATON power lab is tested. Several experiments have been conducted to verify the proposed algorithms.

Chapter 2

Microgrid Configuration

In order to accurately study the behavior of the renewable energy systems, energy storage device and natural gas generator, and their effects on the voltage and frequency in a microgrid, a standard 25kV IEEE 34 bus system is adopted in this paper [29, 30] to model and represent a general proposed microgrid. The system configuration needs to meet the requirements as follows: (i) it is a medium-low voltage distributed system which comprises of balanced/unbalanced three-phase loads and single phase loads. (ii) A considerable complexity of system structure is needed to analyze and evaluate the impact of distributed generations as well as line losses. (iii) A high level of renewable energy penetration is considered. (iv) The system is able to operate in both island mode and grid-tie mode. Therefore, IEEE 34 bus test system is scaled and modified. This chapter discusses the microgrid configuration and capacity sizing for generations.

2.1 Introduction of IEEE 34-Bus Distribution System

The IEEE 34 bus test feeder mimics an actual feeder in Arizona with all its electrical characteristics [31]. The one-line diagram of IEEE 34 bus test feeder system is shown in Figure 2.1. This IEEE 34-Bus test distribution system is a 60Hz, 24.9kV, 12MVA with different fixed loads connected to the utility main at bus 800 and no DG on the system. The load types include constant active/reactive power loads and constant distributed impedance loads (three-phase and single phase). There are several single phase branches in the system, for instance branch of bus 816 to 822 is phase A to Neutral.

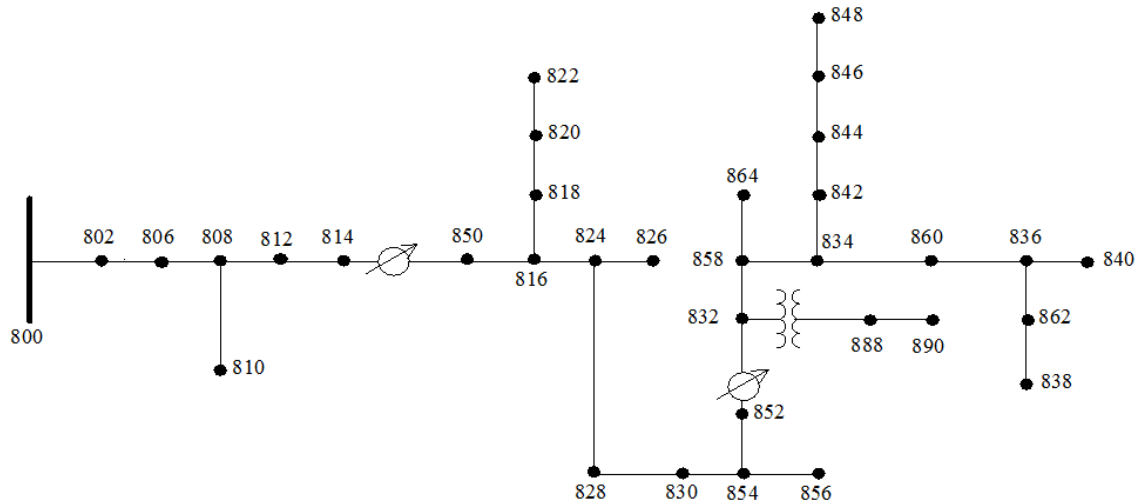


Figure 2.1: One-line diagram of IEEE 34 bus test system.

2.2 Scaling of IEEE 34-Bus Distribution System

In order to match the properties of the system with a microgrid under construction at Fort Sill, OK, the nominal voltage of the system is changed to 12kV and other components of the system including loads and line impedances have been scaled accordingly. The base parameters of the system are changed to 12kV, 6MVA. The transformer on bus 832 is scaled down to 12kV/4.16kV and the two voltage regulators at bus 832 and 814 are also scaled to 6.9 kV, phase voltage.

The power ratings of the fixed PQ loads are reduced to half of their original values. The same also applies to the single-phase PQ loads. To scale the constant impedance loads, their impedances are reduced to half. Since the voltage is also half of the original value, their power rating is reduced to half. There are two types of the transmission lines in this system namely, lumped line impedance and distributed line impedance. Below is the description on scaling these lines.

2.2.1 Lumped Line Impedance

To keep the same voltage drop, the line impedances should be halved since the line carries the same current as described by 2.2.1 and 2.2.2.

$$I = \frac{P/2}{V/2} \quad (2.2.1)$$

$$V_{drop}\% = \frac{V_{drop}/2}{V/2} = \frac{I(R_{line}/2)}{V/2} \quad (2.2.2)$$

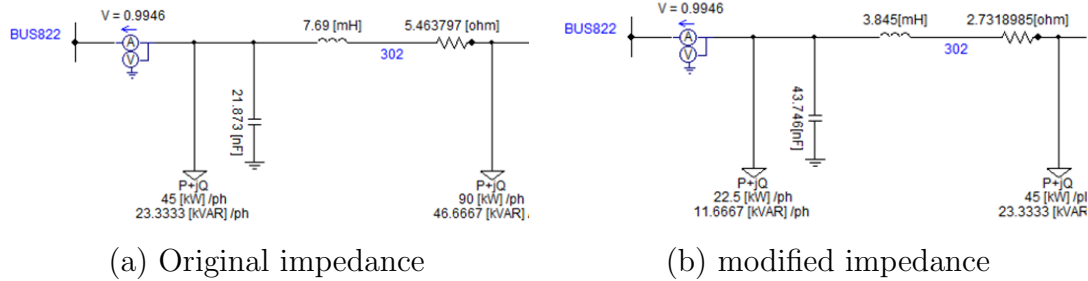


Figure 2.2: Scaling of lumped line impedance for line 302

When the voltage level is scaled down from 24.9kV to 12kV, the distance between phase to phase and phase to earth is reduced, which means that the equivalent capacitance increases. In this case, we have reduced resistances and inductances to half and doubled the capacitance for each lumped line impedance. Figure 2.2 shows an example for the scaling of line 302 connected to bus 822.

2.2.2 Distributed Line Impedance

The case for distributed line impedance is different. We have considered three ways to change the line impedances, when scaling from 24.9kV to 12kV system: (i) halving the R/L matrix, (ii) halving the length of lines, and (iii) halving the length of line and quadrupling the capacitance matrix. Methods (i) and (ii) yield similar results but the voltage drop is larger than the original case. Method (iii) cuts the line power flow in half and at the same time keeps the nodal voltages in per unit the same. Therefore, we have used method (iii) to scale the distributed line impedances.

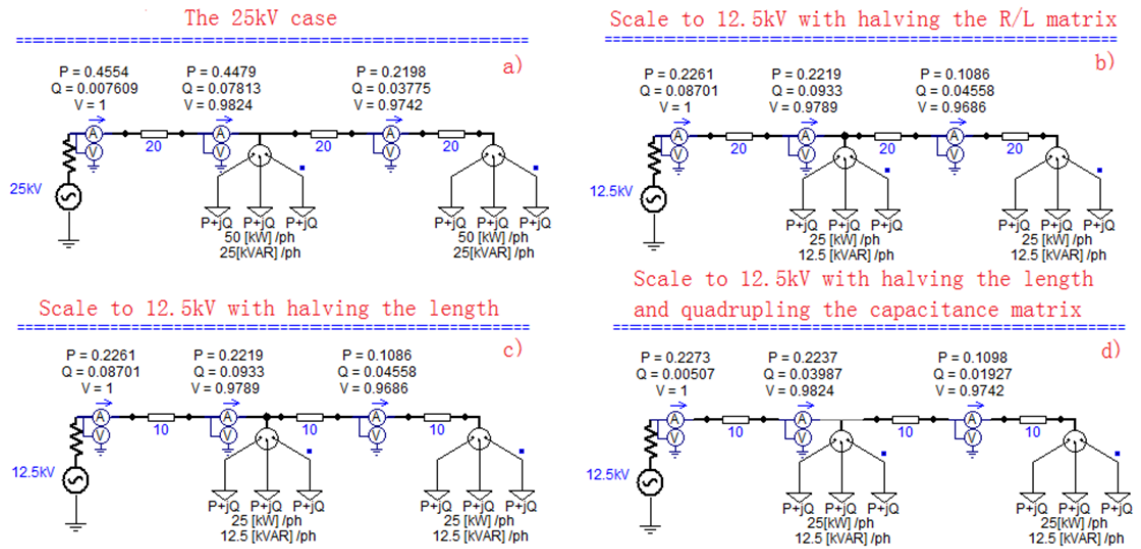


Figure 2.3: Scaling transmission lines with distributed line impedance, (a) original case, (b) Impedance reduced in half, (c) line length is reduced to half, and (d) line length is reduced to half and capacitance is quadrupled.

Figure 2.3 shows the original case and all the three methods for the line. The number 10 and 20 in the figure shows the length of the line. Case (d) provide similar per unit voltage as case (a) while halving active and reactive power.

2.3 Microgrid Components

A backbone of a typical microgrid is shown in figure 2.4. As similar to a traditional distribution system, a general microgrid includes all the basic components that distribution system has such as distribution feeder circuits, protective equipments and switches, primary circuits, distribution transformers and regulators, different types of customers (loads). Other than that, since microgrid is able to be islanded

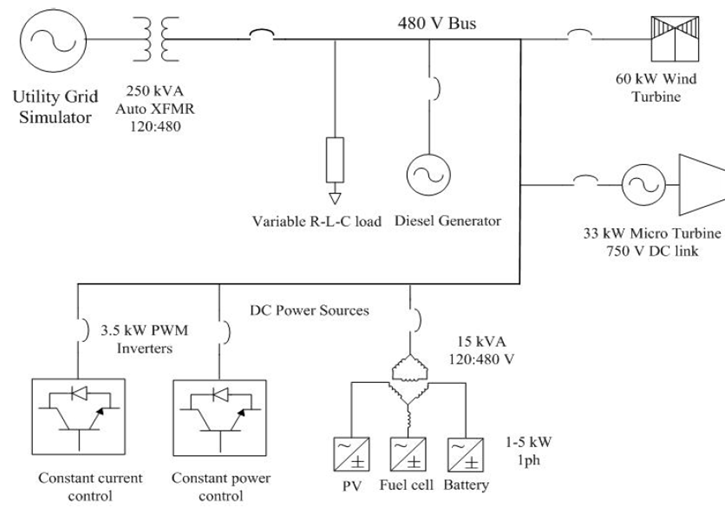


Figure 2.4: A typical microgrid backbone diagram

from the bulk grid, it is required to install other components and devices so that a high performance power management for steady states and transitions operations can be realized. These components are: distributed generations, advanced metering and monitoring, supervisory control units, and interconnectivity devices. Distributed generations which play an important role of supporting local loads within the microgrid are necessary to be added to the system. There are typically three types of power generations installed in the microgrid. First are the renewable energy generations, as they are the green energy and one benefit of the microgrid is that the microgrid provides the most promising means of integrating a large amount of renewable energies in the system. In this paper two 750kW wind turbines and one 250kW PV are added to the system. The sizing issue and power profiles are describe in the following section. Second are the energy storage systems, as they play a role of smoothing the

intermittency of renewable energy, and a key part of managing power flow and voltage stability in the microgrid. They can be either in forms of chemical such as chemical battery, kinetic energy such as flywheel, or potential energy such as supercapacitors. In the paper, two 250kW 500kWh zinc bromide batteries are used and modeled. The third ones are backup generations, which only operate in the island mode and/or in the situation of lacking of renewable energies. A 1.5MVA natural gas generator is developed and used for the proposed microgrid.

2.4 Power Profiles and Capacity Sizing of Generations and Loads

Before discussing the capacity sizing approach for generations, let's define the power profiles of loads as well as generations. It is worth noticing that all the data used for loads, wind and solar PV plants are actual measured data of existing systems that are scaled for the microgrid in this paper. According to the loads, the system includes a total of 53 loads, consisting of fixed and variable PQ loads and fixed impedance loads. The load profile for a single load at bus 848 and total microgrid load are shown in Figure 2.5. The peak load occurs at 7PM and it is 1420kW. The minimum load occurs at 2AM and it is 1120kW.

The solar PV system is modeled using solar irradiation data from Solar Advisor

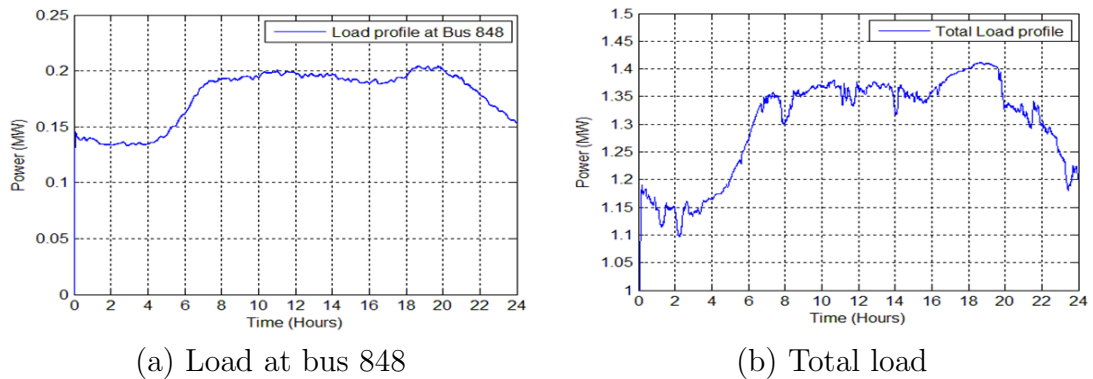


Figure 2.5: Load power profile for a single day

Module (SAM) for the city of Milwaukee, WI. The PV power model contains a 24 hours insulation profile for the summer of 2012. Maximum Power Point Tracking (MPPT) for the panels was developed and simulated using PSCAD software, which will be discussed in Chapter III. Figure 2.6 shows the output power profile for the 250kW system.

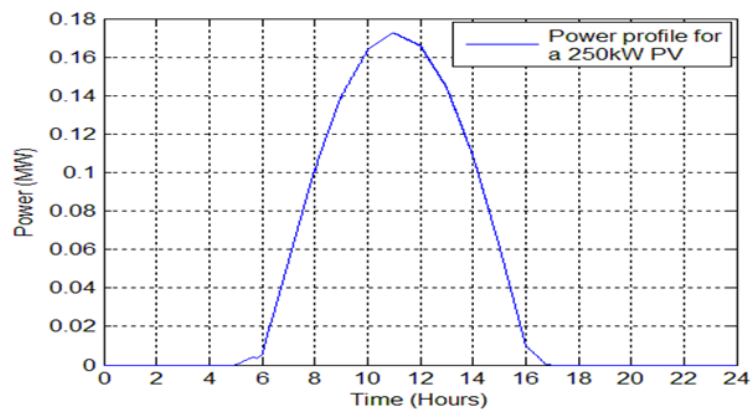


Figure 2.6: The power profile for a 250kW solar PV plant.

The wind turbine power profile is also modeled using measured wind speed data

near the city of Milwaukee WI. The turbine is modeled using PSCAD software considering the turbine efficiency factor (CP) and the mechanical and electrical efficiencies.

Figure 2.7 shows the power profile for a 750kW wind turbine for a 24 hour period.

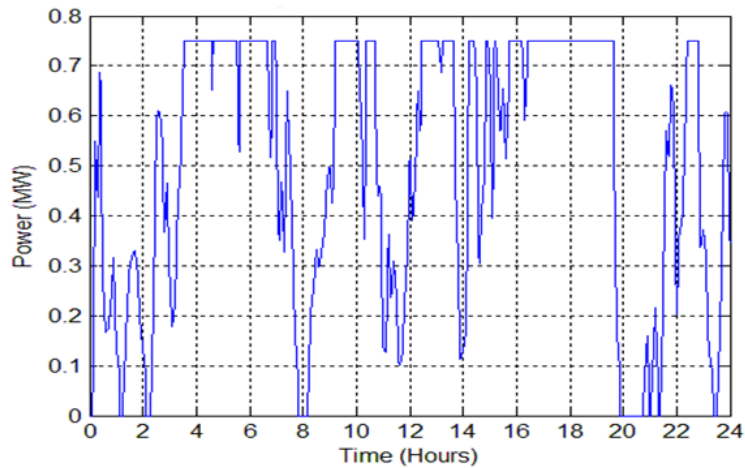


Figure 2.7: The power profile for a 750kW wind turbine.

A first order approach is used in this paper to size the generation capacities. The restrictions for sizing the capacity of generations are stated as follows:

$$P_{NG} + P_{Battery} \geq Peak\ Load\ Demand \quad (2.4.1)$$

$$P_{Battery} \geq Critical\ Load\ Demand \quad (2.4.2)$$

$$P_{Wind} + P_{PV} \leq Peak\ Load\ Demand \quad (2.4.3)$$

$$kWh\ of\ Battery \geq (Peak\ Load\ Demand - P_{NG}) \times Duration\ of\ Zero\ Renewable\ Energy\ for\ 24hrs \quad (2.4.4)$$

Equation 1 gives an operation condition for microgrid without renewable energies. Equation 2 means during transitions when natural gas generator hasn't been ready to provide power, the critical loads are still able to survive. Equation 3 restricts the over sizing of renewable energies. Equation 4 shows a long term planning of battery energy capacity by looking at the probability distribution of renewable energy in order to ensure that the battery has enough energy to support the system during zero renewable energy for a period of time.

The maximum load demand, as shown in Figure 2.5, is 1.42MW. To size the natural gas generator and energy storage, as it was aforementioned, they should meet the total load demand considering line losses without renewable energy sources. Two energy storage systems with total rating of 500kW for two continuous hours are considered for the system to meet the critical load demand. This storage system is a zinc-bromide battery that has been tested and modeled by the research team [32].

The natural gas generator rating is selected at 1.5MVA to meet the total load demand including maximum 0.4MW line loss. The ratings of the renewable sources are selected so that their total capacity does not exceed the total system demand. Wind speed and solar irradiation pattern near city of Milwaukee have been used to calculate the capacity factors for both wind and solar PV systems. The capacity factors for location and device specific data have been calculated at 0.29 for solar PV and 0.34 for wind turbines [33]. Considering an average energy cost of 210/ MWh

for solar PV and 90/ MWh for wind energy [34], required capacities for PV and wind energy are determined to meet the peak load demand. Capacities of 250kW for solar PV and 1.5MW (two 750kW turbines) for wind energy are calculated.

2.5 Summary of Proposed Microgrid

As a summary of the proposed microgrid configuration, a one line diagram of the system is shown in Figure 2.8. One 1.5MVA natural gas generator is added to bus 800

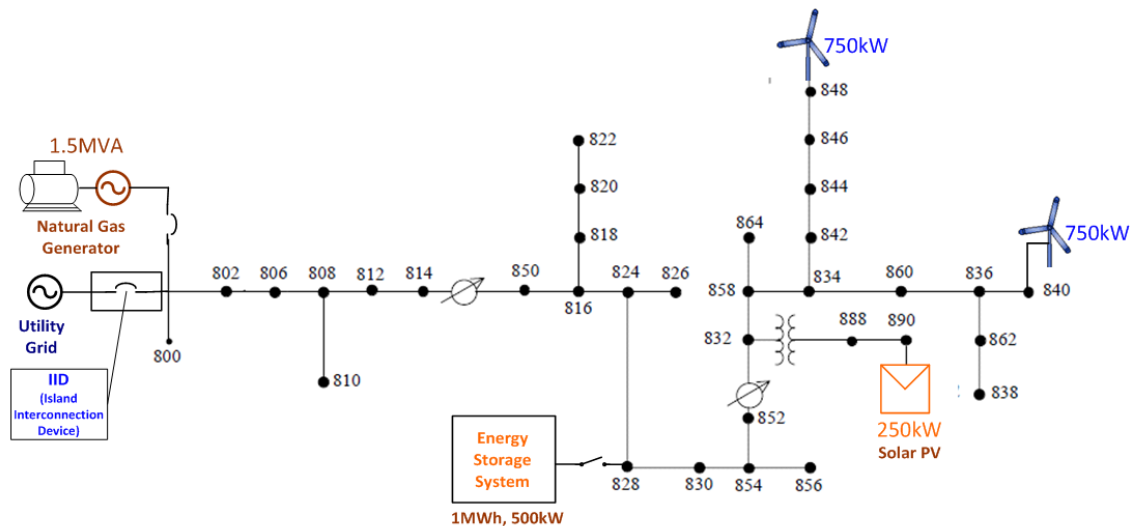


Figure 2.8: The configuration of proposed microgrid using IEEE 34 bus test system.

replacing the utility grid when the microgrid moves to island operation. Two 750kW wind turbines are added to bus 848 and bus 840 respectively and one 250kW solar PV plant is added to bus 890. Two battery parallel together as one energy storage system is added to bus 828 with rating of 1MWh, 500kW.

Chapter 3

Modeling of Microgrid Components

In this chapter, all the important microgrid components including generations, power conversions, and loads, as well as regulator and transformers are introduced and modeled. As aforementioned in previous chapter, there are 4 types of generations within the proposed microgrid which are wind turbine, solar PV plant, natural gas generator, and energy storage system. Except for natural gas generator, the other three generations need a power conversion device to perform a power transportation and control from the different resources to electricity. So a general propose inverter is developed and modeled considering low frequency harmonics which is easy to scale and modified for different generation and is able to switch control strategy to meet the power management.

3.1 Wind Turbine

A total of 1.5MW wind power is needed in the system to meet the sizing demand as we discussed in chapter 2. By considering the limitation of the maximum power transfer and the cable size, we decided to build two wind power plants instead of one 1.5MW wind turbine. The cable used for the laterals in IEEE 34 bus system is ACSR type of conductor. The size is #2 6/1 which has the allowable ampacity of 194 amps. The line impedance is around $1.9+j1.4$ ohms per mile according to the data specs. Let us calculate the K factor of this type of cable so we can evaluate the percentage voltage drop when we consider 1.5MW or 0.75MW power flow on this cable.

The impedance of one mile of line is

$$Z = 1.9 + j1.4\Omega \quad (3.1.1)$$

The current taken by 1kVA at 0.85 lagging power factor is given by:

$$\begin{aligned} I &= \frac{1kVA}{\sqrt{3} \cdot kV_{LL}} \angle -\cos^{-1}(PF) = \frac{1}{\sqrt{3} \cdot 12} \angle -\cos^{-1}0.85 \\ &= 0.0481125 \angle -31.778 \text{ A} \end{aligned} \quad (3.1.2)$$

The voltage drop is computed to be

$$V_{drop} = Re[Z \cdot I] = Re[(1.9 + j1.4) \cdot 0.0481125 \angle -31.778] = 0.113181 \text{ V} \quad (3.1.3)$$

The nominal line-to-neutral voltage is

$$V_{LN} = \frac{12000}{\sqrt{3}} = 6928.2 \text{ V} \quad (3.1.4)$$

The K_{drop} factor is then:

$$k_{drop} = \frac{0.113181}{6928.2} \times 100 = 0.0016336\% \text{ drop/kVA-mile} \quad (3.1.5)$$

In order to evaluate the voltage drop and compare the differences between two selections (a single 1.5MW wind power plant or 2 of 750kW wind power plants), a 2 miles long cable with 1.5MVA uniform distribution loading condition is selected to study. The diagram is shown in Figure 3.1.

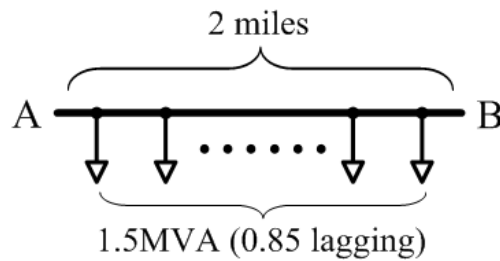


Figure 3.1: One line diagram of a 2 mile long cable with uniform distribution of a total 1.5MVA load.

Considering a 1.5MVA generation added to point A, the per unit voltage at Point B is computed to be:

$$V_B = 1p.u. - K_{drop} \cdot kVA \cdot miles = 0.0016336 \cdot 1500 \cdot 2 = 95.1\% \quad (3.1.6)$$

Instead, if two 750kVA generation are added to point A and point B, the per unit voltage at the middle point of the cable is computed to be:

$$V_{mid} = 1p.u. - K_{drop} \cdot kVA \cdot miles = 0.0016336 \cdot 750 \cdot 2 = 97.55\% \quad (3.1.7)$$

Obviously, if a 1.5MVA generation is adopted to provide power through this cable, the voltage drop is significant. Therefore the power quality would be a big concern.

According to IEEE 34 bus system structure and by evaluating the voltage sensitivity of each bus, two wind power plants are added to bus 840 and bus 848 respectively.

The popular Horizontal Axis Wind Turbine (HAWT) is studied and modeled in PSCAD for wind power plant. The kinetic energy of a 'packet' of air with mass m moving at velocity v is computed to be

$$KE = \frac{1}{2}mv^2 \quad (3.1.8)$$

Dived by time and get power

$$\text{Power through area } A = \frac{1}{2} \left(\frac{m \text{ passing through } A}{t} \right) v^2 \quad (3.1.9)$$

The mass flow rate is

$$\dot{m} = \frac{m \text{ passing through } A}{t} = \rho Av \quad (3.1.10)$$

where ρ is air density.

Combining 3.1.9 and 3.1.10,

$$\begin{aligned} \text{Power through area } A &= \frac{1}{2}(\rho Av)v^2 \\ \Rightarrow P_W &= \frac{1}{2}\rho Av^3 \end{aligned} \quad (3.1.11)$$

where,

$P_W(\text{Watts}) = \text{power in the wind}$

$\rho(\text{kg/m}^3) = \text{air density (1.225kg/m}^3 \text{ at } 15^\circ\text{C and 1atm)}$

$A(m^2)$ = the cross – sectional area that wind passes through

$v(m/s)$ = wind speed

The equation (3.1.11) gives the power in the wind. The wind turbine extracts energy by slowing the wind down. The theoretical maximum amount of energy in the wind that can be collected by a wind turbine’s rotor is approximately 59%. This value is known as the Betz limit. In practice, the collection efficiency of a rotor is not as high as 59%. A more typical efficiency is 35% to 45%. A complete wind energy system, including rotor, transmission, generator, storage and other devices, which all have less than perfect efficiencies, will (depending on the model) deliver between 10% and 30% of the original energy available in the wind. An efficiency factor C_p is defined as:

$$C_p = \frac{\text{power output by wind turbine}}{\text{power in the wind}} \quad (3.1.12)$$

Which can be roughly estimated:

$$C_p = \eta_{rotor} \times \eta_{mechanical} \times \eta_{electrical} = 40\% \times 80\% \times 90\% = 28.8\% \quad (3.1.13)$$

Finally, the electrical power equation for A HAWT is obtained:

$$P_{out} = \frac{1}{2} \rho \pi r^2 v^3 C_p \quad (3.1.14)$$

The radius is derived to be

$$r = \sqrt{\frac{2P_{out}}{\rho \pi v^3 C_p}} \quad (3.1.15)$$

Considering 12 m/s as the rated speed, a 750kW wind turbine has a blade radius of

$$r = \sqrt{\frac{2 \cdot 750000}{1.225 \cdot 3.1416 \cdot 12^3 \cdot 0.288}} \approx 28m \quad (3.1.16)$$

According to the above calculations, a 750kW HAWT is modeled in PSCAD shown in Figure 3.2 with consideration of cut-in and cut-out functions. The principle of wind speed vs. output power is shown in Figure 3.4, where there are four operation regions. In region 1 wind turbine cannot generate useable power when the wind speed is less than 4m/s, which is usually called cut-in speed. In region 2, the output power is proportional to the wind speed until the wind speed reach 12m/s, which is called rated wind speed or nominal speed. In region 3, the blade pitch is controlled so that the output power keep constant until the wind speed reaches cut-out speed, which is 25m/s defined in the model. In region 4, the wind turbine ceases power generation and shut down because a very high wind speed may damage the rotation components of the wind turbine.

A 24 hours real wind data near Milwaukee area is imported. The simulation results are shown in Figure 3.3. For simulation purpose, the 24-hour data is scaled to 240sec.

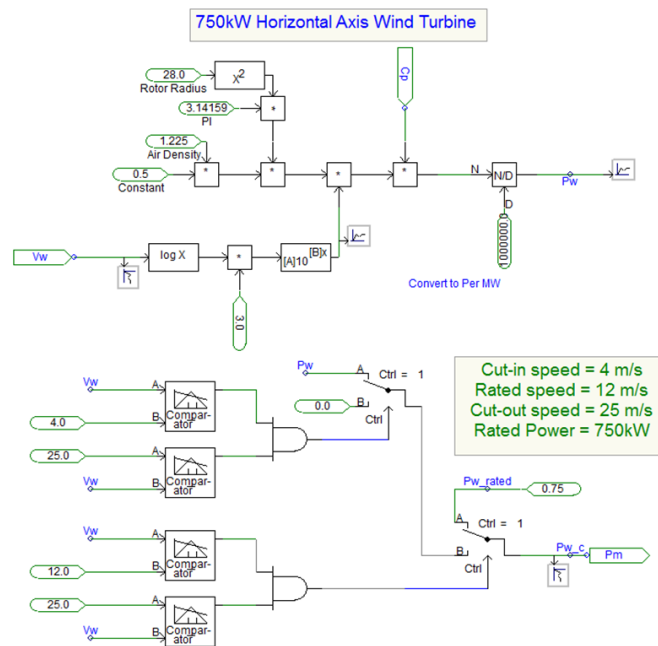


Figure 3.2: A 750kW wind turbine model with cut-in and cut-out functions.

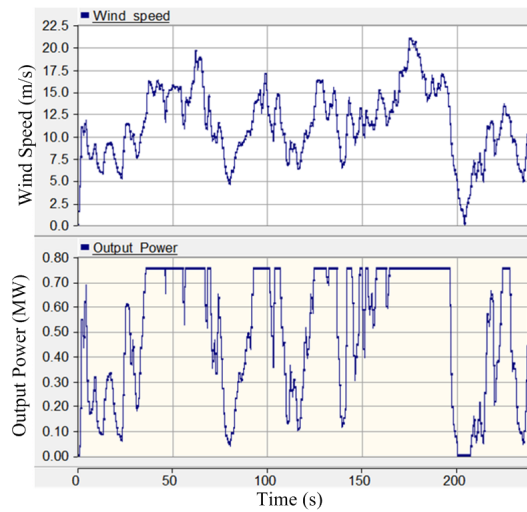


Figure 3.3: Simulation results for 750kW HAWT using 24 hours real data. Top: Wind speed(m/s); Bottom:Output Power(MW)

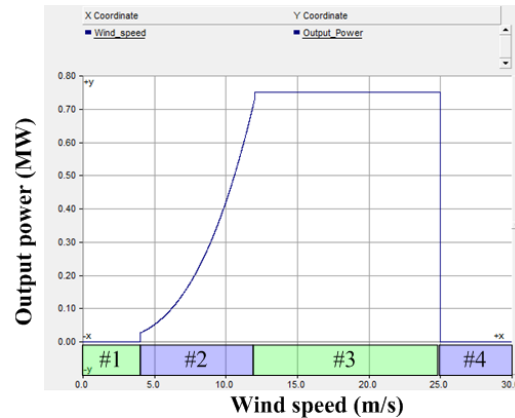


Figure 3.4: Wind speed vs. Output power

3.2 Solar PV

Comparing with wind energy, solar power plant has its unique merits such as residential friendly, no pollution and no noise, easy to deliver and install, almost zero maintenance cost, and reliable and safe to use. However, as the solar resource is not as good as wind power at Milwaukee-Wisconsin area, combining different practical considerations which has been discussed in Chapter 2 section 4, a 250kW solar PV is selected to be added to the proposed microgrid. In this section, the modeling of 250kW solar PV plant in PSCAD is presented.

A commonly used equivalent circuit of solar cell is shown in figure 3.5. The PV cell is deemed to be a current source whose value equals to I_{SC} paralleling with a forward diode. Forward current that flows through the diode is viewed as dark current I_d in the PV cell. R_s and R_p are the series and parallel resistance of the PV cell.

R_s is made up of surface resistance of the roof of the proliferation, body resistance of the cell, resistance between the top and bottom electrode and PV cell as well as resistance of the metal conductor. R_p is mainly caused by the following factors: the surface leakage current along the edge of the cell, which is caused by the surface spots; the leakage current along the small bridge that caused by the disfigurement of the micro-cracks, grains and crystal after the electrode metal processing, or caused by the dislocation and the irregular spread of the grains.

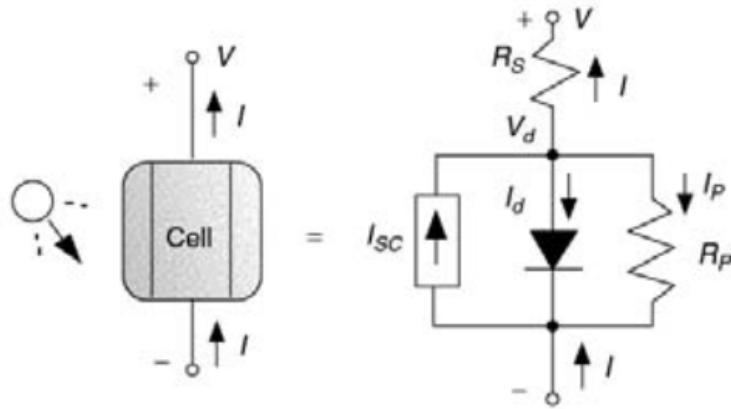


Figure 3.5: A more complex equivalent circuit for a PV cell includes both parallel and series resistances.

The output current I is computed to be

$$I = I_{SC} - I_0 \left\{ \exp \left[\frac{q(V + I \cdot R_s)}{kT} \right] - 1 \right\} - \left(\frac{V + I \cdot R_s}{R_p} \right) \quad (3.2.1)$$

where,

I_{SC} : Short-circuit current

I_0 : Saturation current

q : Electron charge, $1.6e^{-19}$

k : Boltzman constant, $1.38e^{-23}$

T : Absolute temperature

R_s : Series parasitic resistance

R_p : Shunt parasitic resistance

According to equation (3.2.1), the I-V curve is able to be obtained if R_p and R_s are known. The effects of R_p and R_s on I-V curve are shown in figure 3.6. Obviously, series and parallel resistances in the PV equivalent circuit decrease both voltage and current delivered. To improve cell performance, high R_p and low R_s are needed.

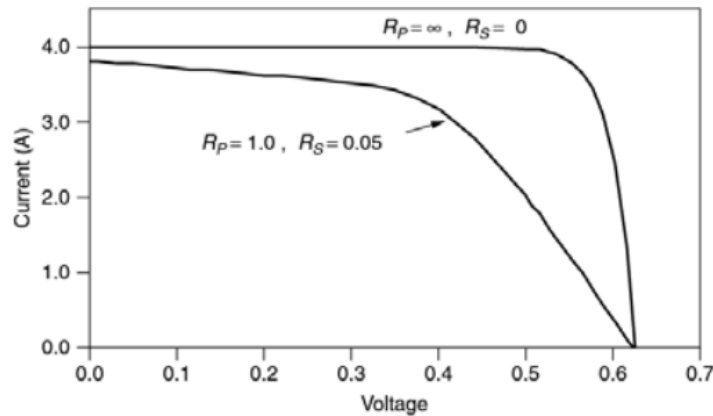


Figure 3.6: Series and parallel resistances in the PV equivalent circuit decrease both voltage and current delivered.

In order to achieve maximum power output, an appropriate operation point in I-V curve is necessary to be located, which is called maximum power point tracking. Figure 3.7 illustrates where the point is in a typical I-V curve. Various literatures studied on this problem and developed a lot of tracking methods. In this paper,

an incremental conductance method is developed in PSCAD. The basic idea of this control is to measure incremental changes in array current and voltage to predict the effect of a voltage change.

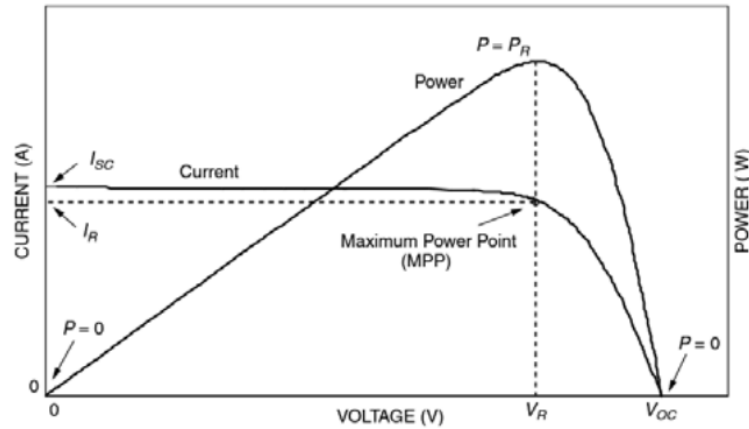


Figure 3.7: The I-V curve and power output for a PV module. At the maximum power point the module delivers the most power that it can under the conditions of sunlight and temperature for which the I-V curve has been drawn.

Table 3.1: The key parameters of PV array

Rated Power	25kW
# of modules in series per module	2
# of modules in parallel per module	3
# of cells in series per module	50
# of cells in parallel per module	52
Reference Irradiation (W/m^2)	1000
Reference temperature (C)	25
Open circuit voltage (V)	83.47
Short circuit current (A)	390

The PV array and MPPT function are modeled in PSCAD shown in Figure 3.8. The key parameters are listed in table 3.1. The I-V curve of this 25kW PV array is tested and shown in Figure 3.9.

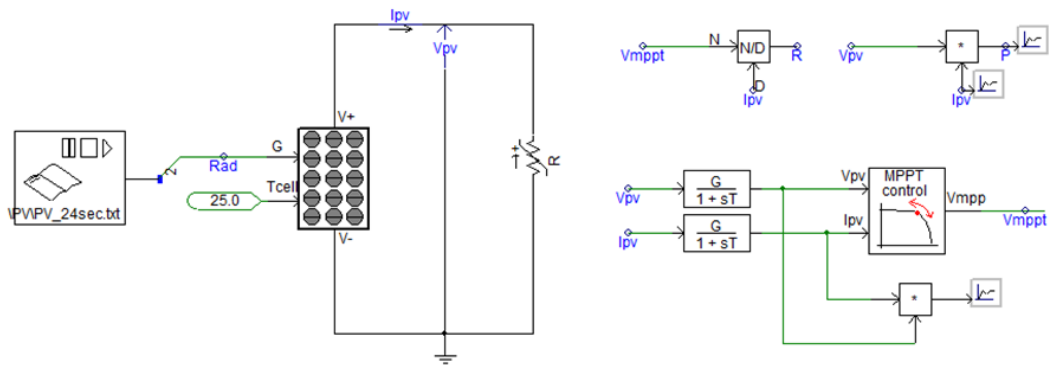


Figure 3.8: The PV array and MPPT function in PSCAD.

Practically, to build a 250kW solar power plant, 10 arrays with converters will be paralleled on a DC bus and connected to AC bus via an inverter. However, since the main focus of the project is the operation and management of microgrid, to simplify the problem and reduce the simulation time, the average models for inverters are developed. Therefore the 250kW PV model is built by scaling of output power of the proposed 25kW PV array. The scaled power command received from PV array is power reference for the inverter attached to the PV generation.

The irradiation profiles of a perfect sunny day and a typical cloudy day is tested and simulated. The waveforms of irradiation profiles, power profiles and MPPT voltages for two cases are shown in Figure 3.10 and Figure 3.11 respectively.

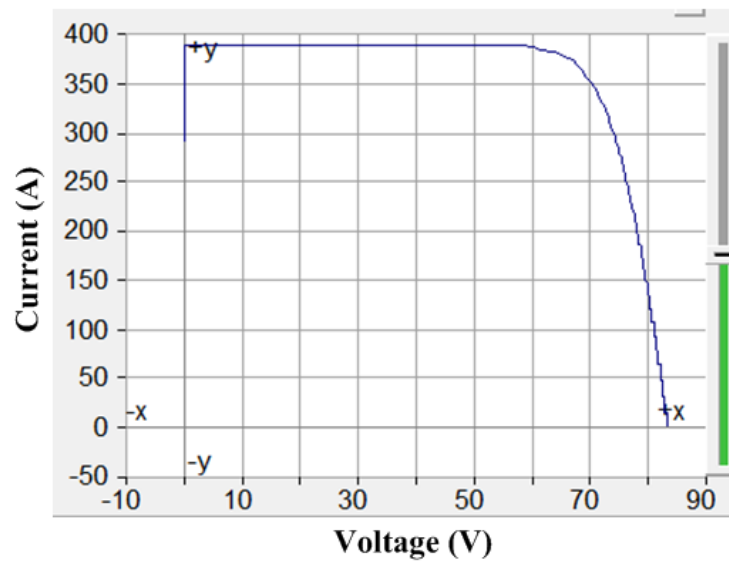


Figure 3.9: The I-V curve of 25kW PV array.

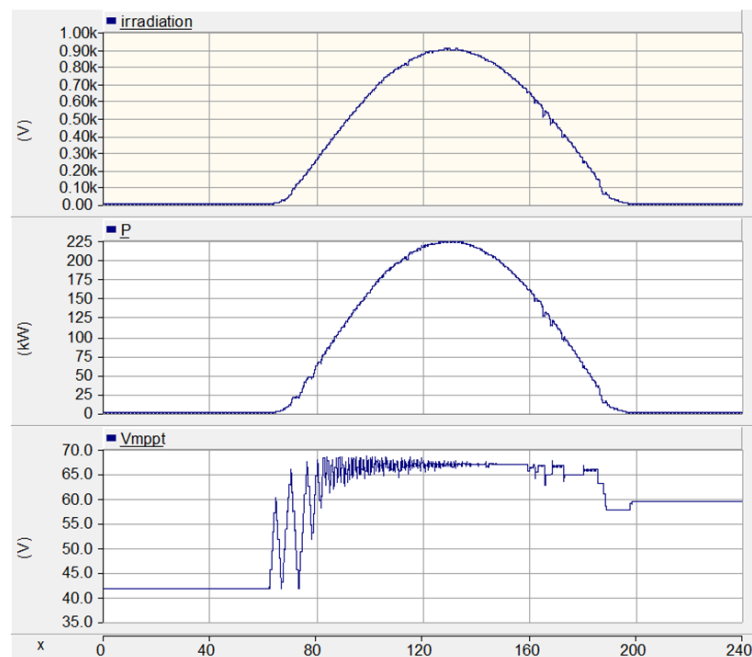


Figure 3.10: The waveforms of solar irradiation profile, PV output power and terminal voltage at MPPT in a perfect day.

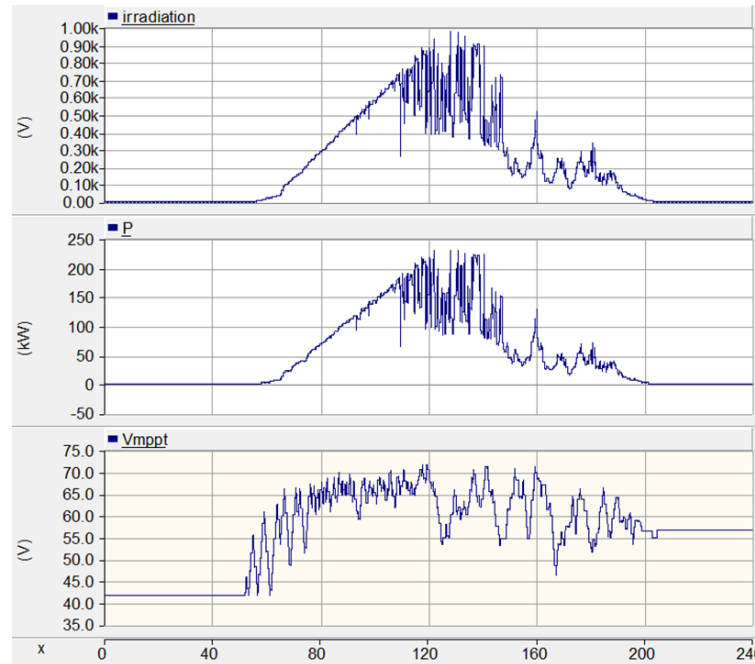


Figure 3.11: The waveforms of solar irradiation profile, PV output power and terminal voltage at MPPT in a cloudy day.

3.3 Natural Gas Generator

Natural gas generator plays a very important role in microgrid. It controls the voltage and frequency in the microgrid in island mode. Other sources use it as a reference for frequency. Whenever a load is applied to or removed from the microgrid, the voltage and frequency experience a transient before settling at the steady state values. The magnitude and duration of this transient depends on the generator exciter and engine governor controls. During sudden changes in the load, the natural gas generator must be able to maintain the voltage and frequency within the limits. The

same is also true when there is sudden change in the renewable energy generations.

Figure 3.12 shows the basic block diagram of a natural gas generator connected to a grid or microgrid. The exciter is in charge of regulating output voltage and the governor adjusts engine speed, which is translated to output frequency.

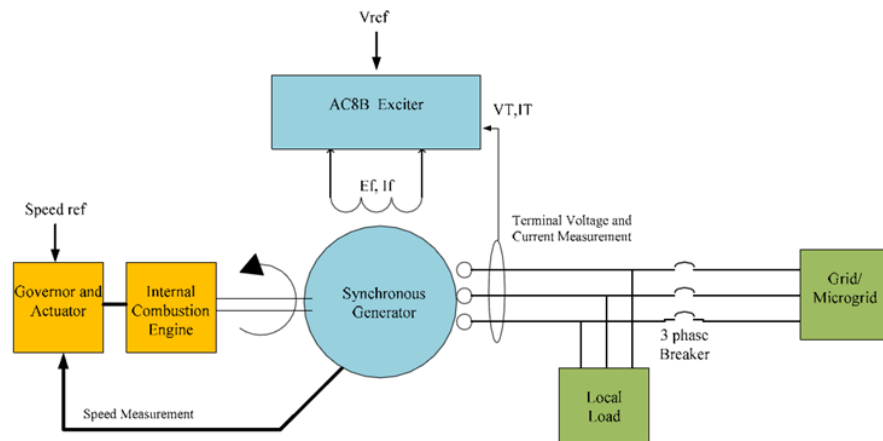


Figure 3.12: The basic block diagram of a natural gas generator connected to a grid/microgrid.

Table 3.2: The key parameters of PV array

Rated RMS Line to Neutral Voltage	6.9282 [kV]
Rated RMS Line Current	0.09 [kA]
Base Angular Frequency	376.991118 [rad/sec]
Armature Time Constant [T_a]	0.332 [pu]
Poitier Reactance [X_p]	0.011 [pu]
D:Unsaturated Reactance [X_d]	0.13 [pu]
D:Unsaturated Transient Reactance [X_d']	0.03 [pu]
D:Unsaturated Transient Reactance Time (open) [T_d0']	5.2 [s]
D:Unsaturated Sub Transient Reactance [X_d'']	0.022 [pu]
D:Unsaturated Sub Transient Reactance Time (open) [T_d0'']	0.029 [s]
Q:Unsaturated Reactance [X_q]	0.51 [pu]
Q:Unsaturated Transient Reactance [X_q']	0.228 [pu]

There is one natural gas generator in our microgrid system. The properties of this 1.5MVA machine are provided in Table 3.2. In order to accurately study the behavior of the synchronous machine for the power system stability studies, it is essential that the excitation system of the machine is modeled with sufficient details. The desired model must be suitable for representing the actual excitation equipment performance for large, severe disturbances as well as for small perturbations. IEEE Standard 421.5 recommends three distinctive types of excitation systems including DC type excitation systems, AC type excitation systems, and static type excitation systems. Due to fairly small size of the machines in this paper, we have chosen AC8B: Alternator Supplied Rectifier Exciter with Digital Control #2 exciter type. Figure 3.13 shows the block diagram of this exciter.

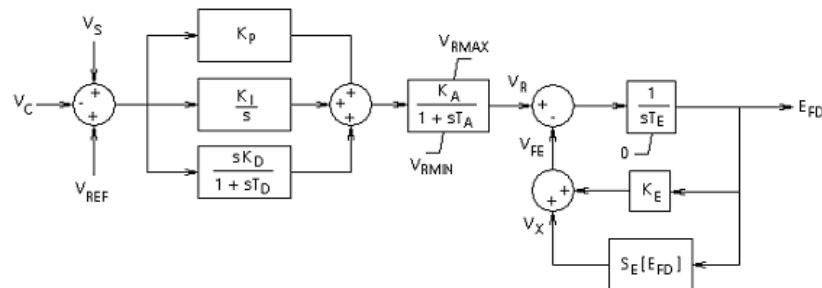


Figure 3.13: The block diagram of AC8B AC exciter.

Where, V_S is the terminal voltage transducer and load compensation elements [pu], V_{REF} is the voltage regulator reference (determined to satisfy initial conditions) [pu], V_C is the combined power system stabilizer and possibly discontinuous control output after any limits or switching, as summed with terminal voltage and reference

signals [pu], E_{FD} is the Exciter output voltage [pu].

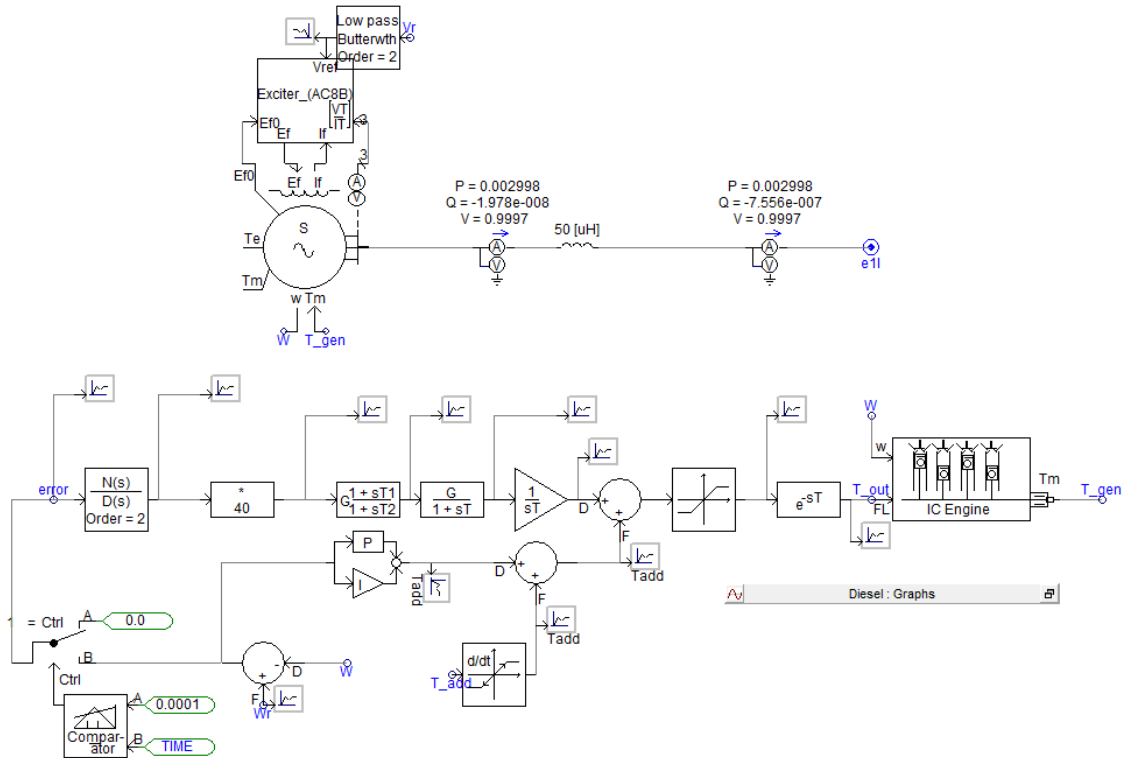


Figure 3.14: The model of 1.5MVA natural gas generator in PSCAD.

The model of this 1.5MVA natural gas generator in PSCAD is shown in Figure 3.14. Several tests have been conducted. Figure 3.15 shows the simulations results for the natural gas generator when load steps occur at 10 and 20 seconds. The machine starts at no load. At 10s, a 100% step load with a power factor of 0.85 is applied, where real power is 1.275MW and reactive power is 0.79MVar. The speed and terminal voltage of the machine drop as indicated. At 20s, the load is removed and the voltage and frequency spike. It should be noted that these results are only for the natural gas generator and a load.

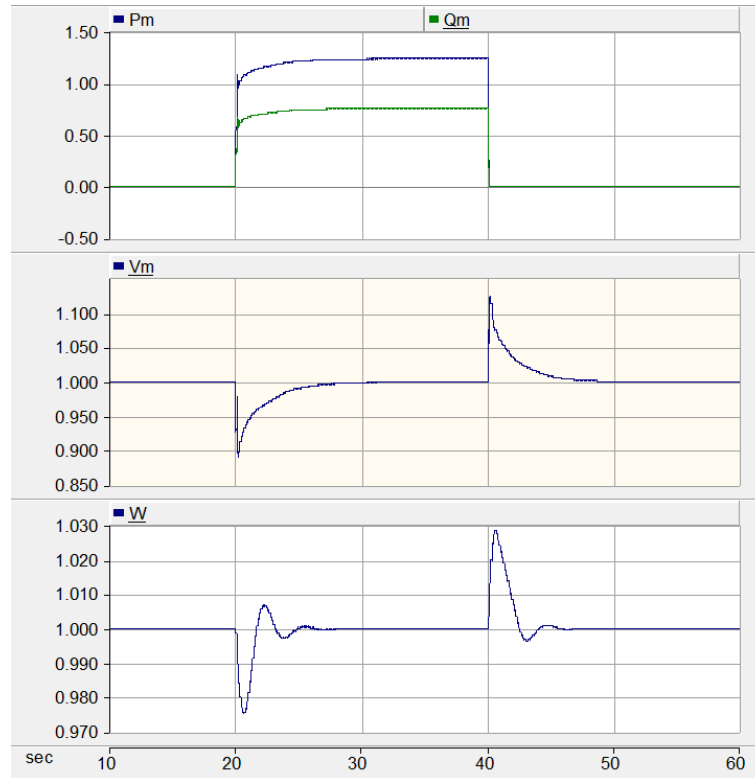


Figure 3.15: Simulation results for the natural gas generator in off-grid operation when load steps are applied at 10s and 20s: from top, Real (blue in MW) and reactive power (green in MVar), terminal voltage (pu), and rotor speed (pu).

Figure 3.16 shows the simulation results for the natural gas generator when it is connected to the grid and has 100% power command change with 0.85 power factor at 20s and 60s.

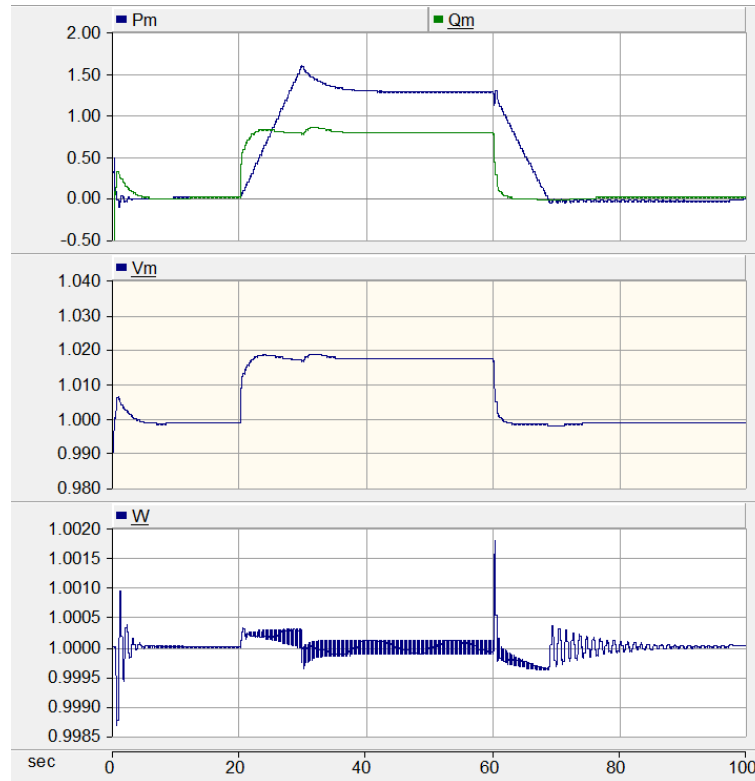


Figure 3.16: simulation results for the natural gas generator in grid-tie operation when power command steps are applied at 10s and 20s: from top, Real (blue in MW) and reactive power (green in MVar), terminal voltage (pu), and rotor speed (pu).

3.4 Zinc-Bromide Energy Storage System

In Fort Sill Microgrid project, a 250kW Zinc Bromide Battery designed and provided by ZBB Energy Corporation is used as the energy storage unit. Therefore, in this general purposed microgrid the same 250kW Zinc Bromide battery is modeled and installed in the system. To meet the capacity requirement discussed in Chapter 2, 2 units of 250kW battery are paralleled to have 500kW, 1MWh installed at Bus

828.

Compared with other batteries such as lead-acid battery or Lithium-ion battery, Zinc Bromide battery has a longer cycle life. [32] The comparison of properties are listed in Table 3.3. Although Zinc Bromide battery has less power and energy density than Lithium-ion, which means with the same power rating, Zinc Bromide has the bigger dimension, it has 4 times of cycle life than Lithium-ion which is more important for the application of microgrids.

Table 3.3: The comparison of properties of Zinc-Bromide battery and other batteries

Battery	Energy Density (Wh/kg)	Power Density (W/kg)	Cycle Life
Lead-Acid	30-50	100-200	200-300
Lithium-Ion	150-190	300-1500	300-500
Nickel Metal Hydrate	60-120	250-1000	300-500
Zinc Bromide	85-90	300-600	2000

Generally, there are three basic categories of modeling battery: Thevenin based, impedance based and runtime based, as shown in Figure 3.17. A Thevenin based model shown in Figure3.17(a) uses a series resistor (R_{series}) and RC parallel network ($R_{transient}$ and $C_{transient}$) to predict battery response to transient load evens at a particular state of charge, by assuming the open-circuit voltage (V_{oc}) is constant. Impedance based models shown in Figure3.17(b), employ the method of electrochemical impedance spectroscopy to obtain an ac-equivalent impedance in the frequency domain, and then use a complicated equivalent network (Z_{ac}) to fit the impedance

spectra. Runtime based models shown in Figure 3.17(c) use a complex circuit network to simulate battery runtime and dc voltage response for a constant discharge current in SPICE-compatible simulators.

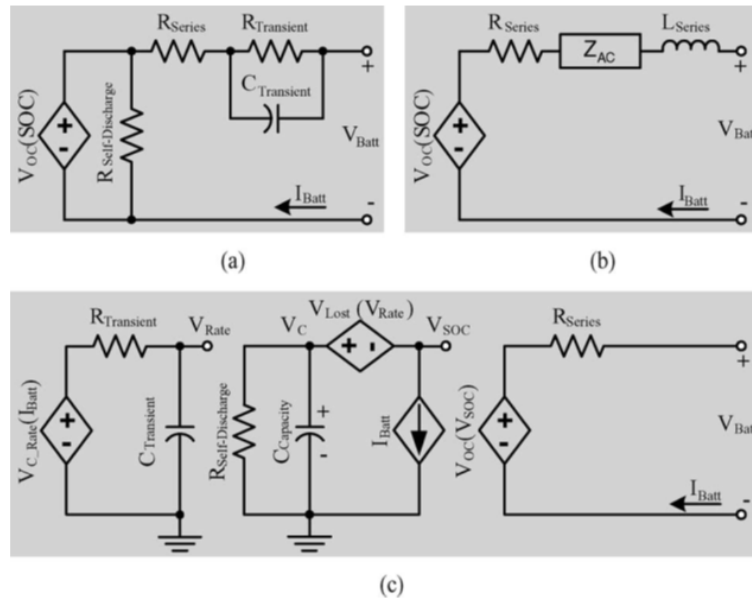


Figure 3.17: Three basic types of modeling of battery. (a)Thevenin based, (b)Impedance based, (c)Runtime based.

Refer to paper [32], after conducting a series tests, a Thevenin equivalent circuit with non-linear components is developed to model the Zinc Energy Storage System (ZESS), as shown in Figure 3.18. By measuring OCV at different values of SOC, the relationship between OCV and SOC is fitted by 4th order polynomial function in equation (3.4.1).

$$\begin{aligned}
 OCV(SOC) = & 1.8781 \times 10^{-6} \cdot SOC^4 + 5.2857 \cdot 10^{-4} \cdot SOC^3 \\
 & - 0.0535 \cdot SOC^2 + 2.3386 \cdot SOC + 63.0936
 \end{aligned} \tag{3.4.1}$$

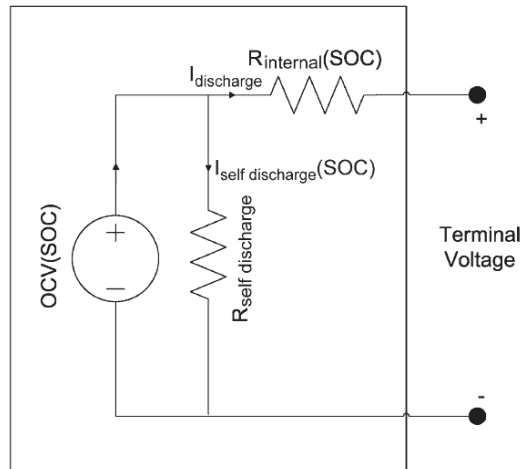


Figure 3.18: The electrical model of ZESS.

The internal resistance is a function of many variables but it mainly depends on the cell and ambient temperatures as well as the SOC. According to the test data, an exponential function representing $R_{internal}$ is obtained:

$$R_{internal}(SOC) = 5.9415e^{-0.13493 \cdot SOC} + 0.06254e^{-5.7711 \times 10^{-3} \cdot SOC} \quad (3.4.2)$$

The self-discharge resistance is supposed to be a constant value independent to SOC, which is measured as 5.12 Ohm.

To sum up, the equations for the terminal voltage and state of charge can be computed as:

$$V_t(SOC) = OCV(SOC) + R_{internal}(SOC) \cdot i_t \quad (3.4.3)$$

$$SOC = 1 - \int_0^t i_t \times dt_i \quad (3.4.4)$$

where, V_t is terminal voltage; i_t is discharging current.

Based on the equations aforementioned, the ZESS has been modeled in PSCAD as shown in Figure 3.19.

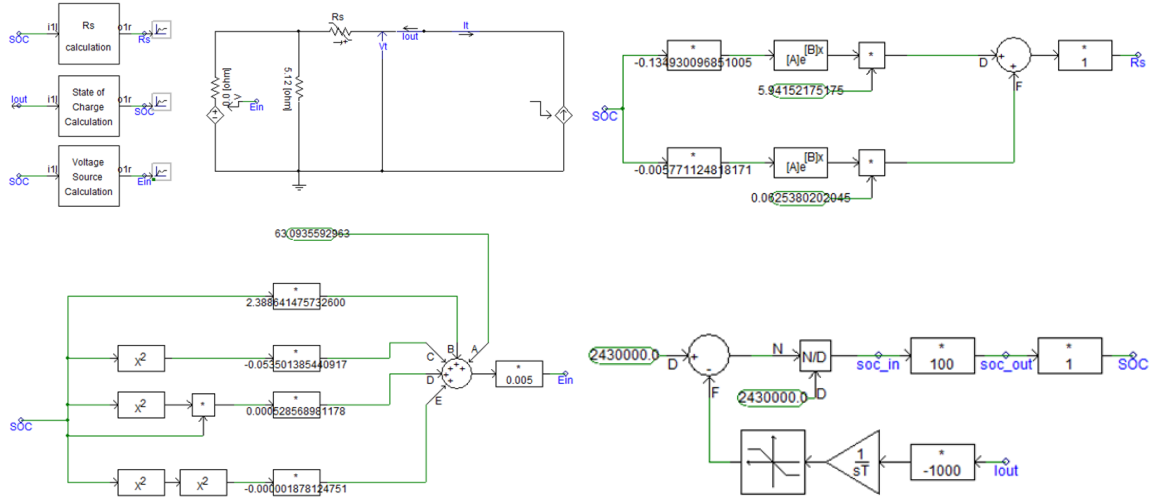


Figure 3.19: The ZESS model in PSCAD.

A constant current charging and discharging tests have been conducted for the proposed model. Figure 3.20 shows the discharging terminal current. Figure 3.21 shows the waveform of state of charge. Figure 3.22 shows the terminal voltage and the battery open circuit voltage. Figure 3.23 shows the waveform of OCV versus SOC. Figure 3.24 shows the waveform of internal resistance versus SOC.

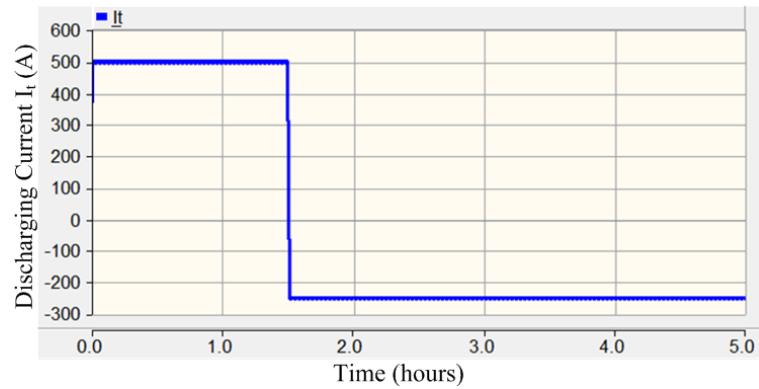


Figure 3.20: The waveform of charging current.

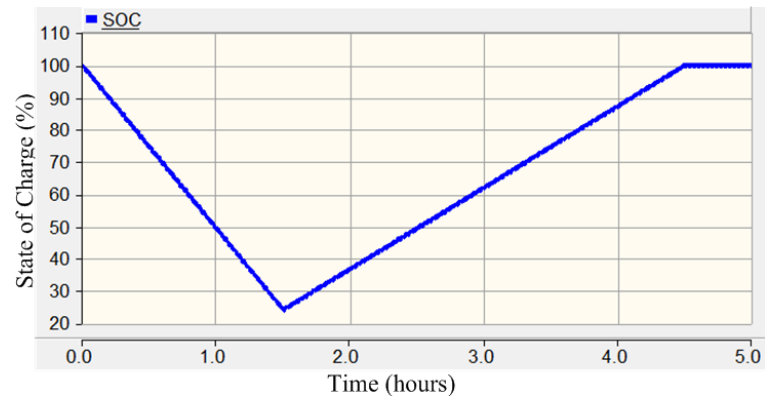


Figure 3.21: The waveform of state of charge in percentage.

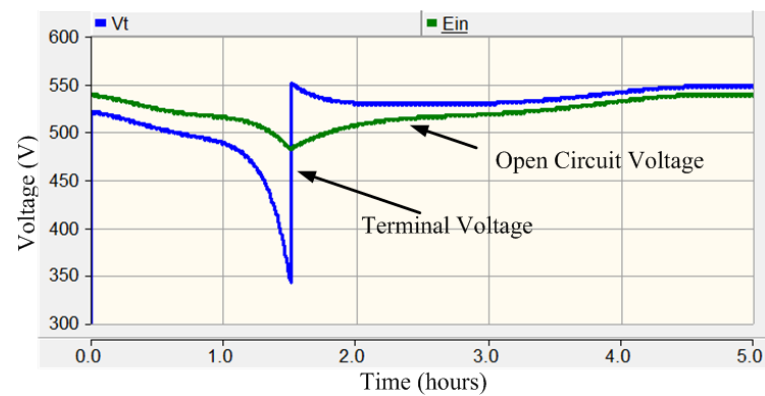


Figure 3.22: The waveforms of OCV and terminal voltage.

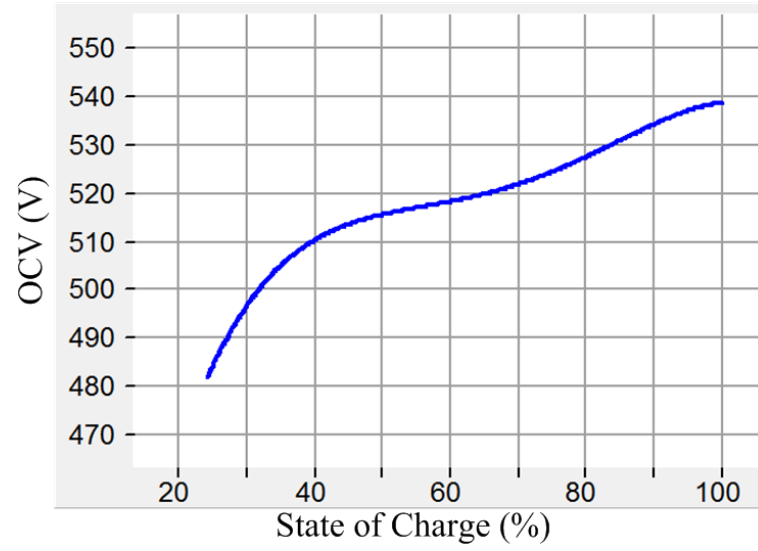


Figure 3.23: The curve of OCV versus SOC.

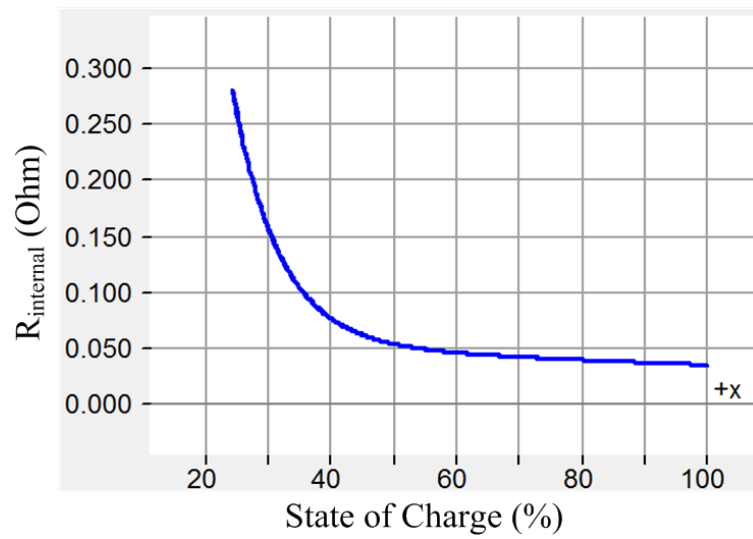


Figure 3.24: The curve of R_s versus SOC.

3.5 General-Purpose Inverter

Most DGs within microgrid are inverter based generations such as solar PV, battery, wind power, micro-turbine, etc. A general purposed inverter is designed to be able to interface with different generations with different power ratings. As we know, active and reactive controls functions for DGs are different in grid-tie and island modes, in addition, different DGs may require different control modes such as P/Q control and v/f control. In the paper, three DGs need inverters: PV, Wind and Battery. Among these DGs, battery is expected to be capable of regulating real and reactive power flow as well as voltage magnitude and frequency, while PV and Wind basically only need to be able to regulate real and reactive power. Figure 3.25 shows the block diagram of the energy storage inverter control proposed and applied in this study. The active and reactive power delivered are adjusted by regulating the output voltage magnitude and angle relative to microgrid bus voltage. The controller can adjust the output voltage (and consequently active and reactive power) according to measured voltage and frequency as well as commands from a supervisory controller. To apply this inverter to PV and wind, several changes are necessary: (i) with different power ratings, LCL filter needs to be re-designed; (ii) disable voltage and frequency control functions; (iii) communication is not necessary for renewable energies as a secondary power management method is proposed and applied for PV and Wind, which will be discussed in Chapter 4.

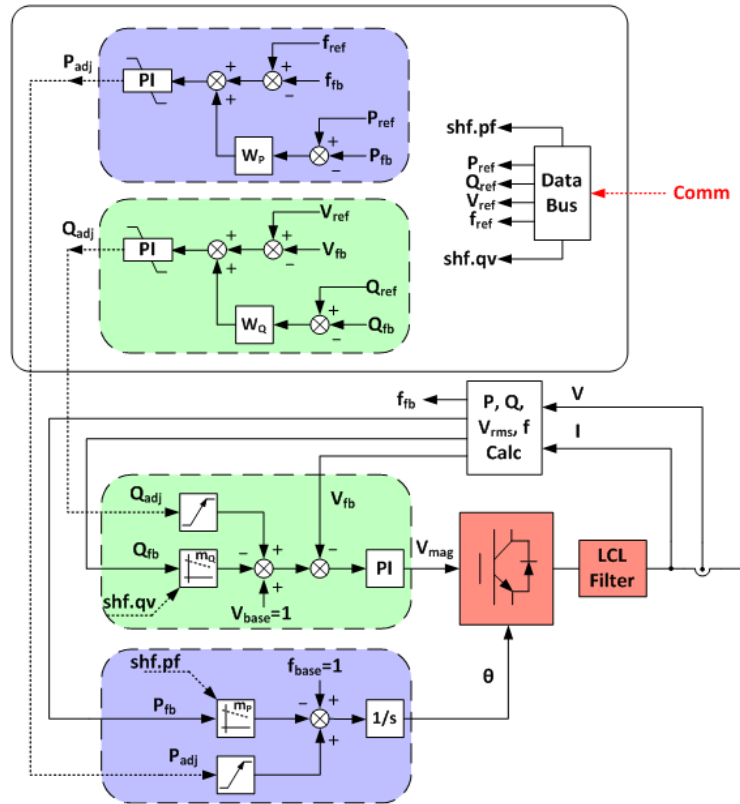


Figure 3.25: The block diagram of the controls for voltage and frequency of storage inverter.

The PSCAD model of the proposed inverter is shown in Figure 3.26. This control algorithm is also applied to a 1MW Multi-inverter based microgrid [35].

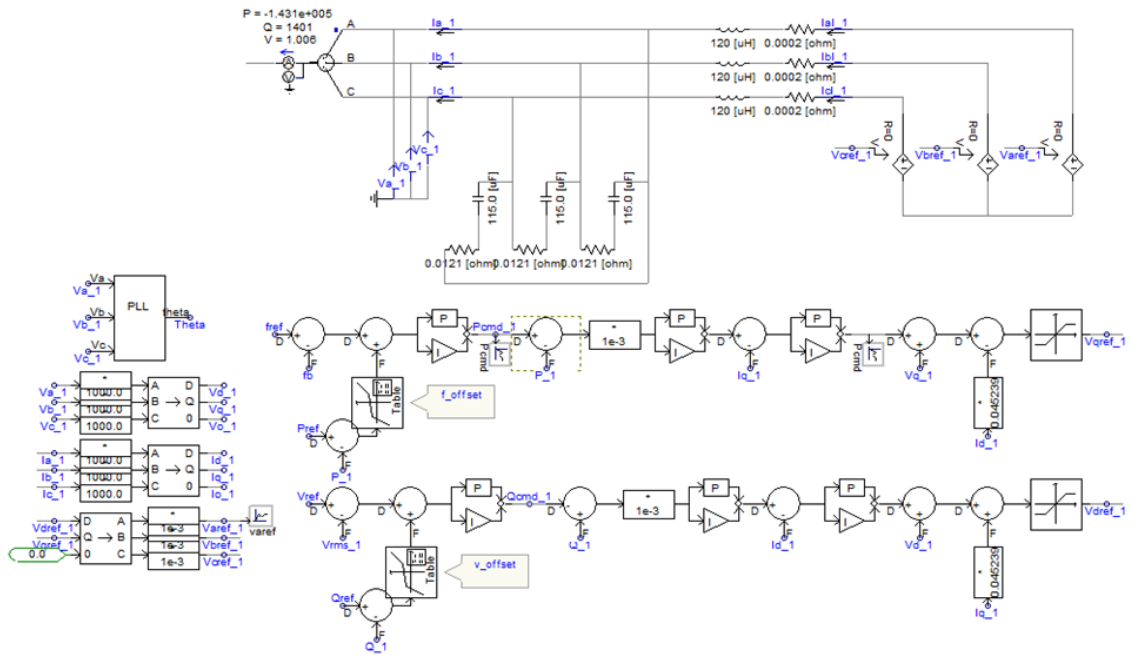


Figure 3.26: The proposed inverter model in PSCAD.

3.6 Other Basic Components

Modeling of Load

One of the most important basic components is load. As we know there are typically three types of loads: impedance load, current load, and power load. The static load can be modeled using equations:

$$P = P_o \cdot \left(\frac{V}{V_o}\right)^{NP} \cdot (1 + K_{PF} \cdot dF) \quad (3.6.1)$$

$$Q = Q_o \cdot \left(\frac{V}{V_o}\right)^{NQ} \cdot (1 + K_{QF} \cdot dF) \quad (3.6.2)$$

where,

P = equivalent load real power,

P_o = rated real power,

V = load voltage,

$NP = dP/dV$ voltage index for real power,

$K_{PF} = dP/dF$ frequency index for real power,

Q = equivalent load reactive power,

Q_o = rated reactive power,

$NQ = dQ/dV$ voltage index for reactive power,

$K_{QF} = dQ/dF$ frequency index for reactive power.

By giving different values of NP and NQ, all types of fixed loads are able to be modeled. According to the variable loads, a dynamic variable inductance and resistance are used to achieve the desired real and reactive power. A single phase variable load is shown in Figure 3.27.

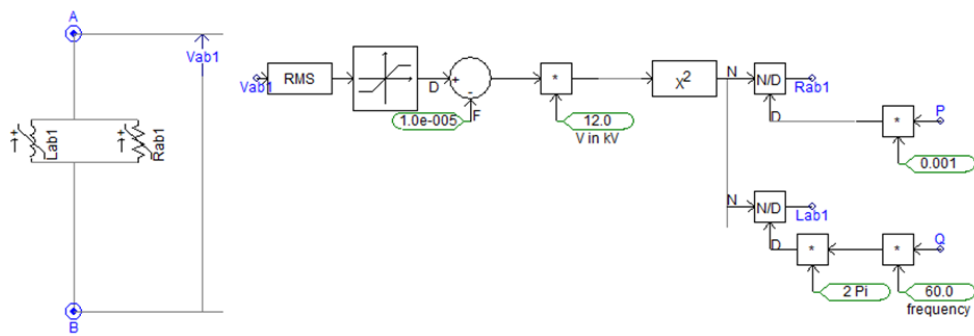


Figure 3.27: The model of variable load in PSCAD.

Regulators

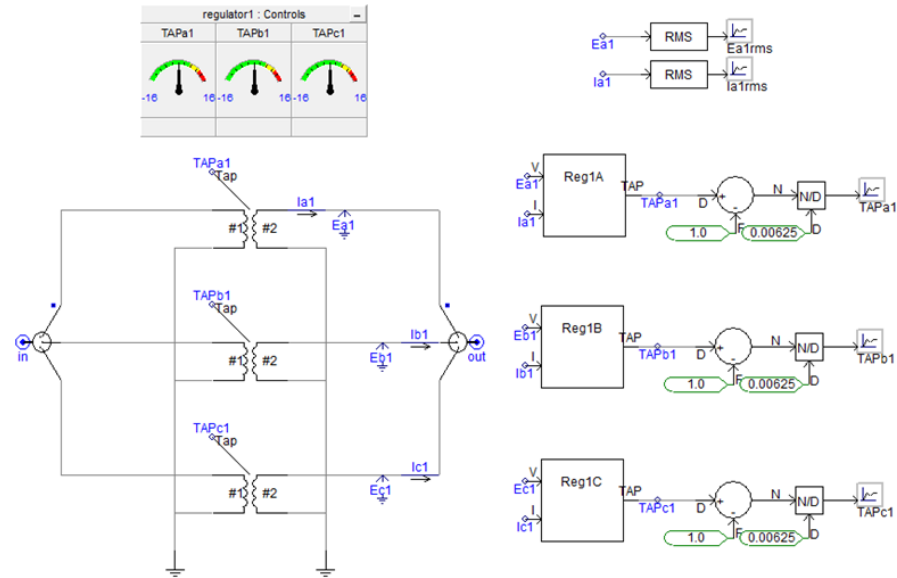


Figure 3.28: The model of regulator in PSCAD.

There are two regulators in IEEE 34 bus test system. The parameters are shown in Table 3.4. The PT ratio is 120 scaling phase voltage of 6.9282kV to 57.735V. Taps range is from -16 to 16 representing a voltage bandwidth of 2 Volts. The model is shown in Figure 3.28.

Table 3.4: The settings for regulators and compensators.

	Regulator 1	Regulator 2
PT Ratio	120	120
Primary CT Rating	100	100
CT Ratio	500	500
Bandwidth	2V	2V
R for compensator	2.7V (or $2.7/0.2=13.5\text{ohm}$)	2.5V (or $2.5/0.2=12.5\text{ohm}$)
X for compensator	1.6V (or $1.6/0.2=8\text{ohm}$)	1.5V (or $1.5/0.2=7.5\text{ohm}$)
Voltage level	122V	124V

Chapter 4

Microgrid Operation and Management

The microgrid is defined as a group of interconnected loads and distributed energy resources within clearly defined electrical boundaries that acts as a single controllable entity with respect to the bulk grid. It allows to be operated with connect to or disconnect from the bulk grid. Generally, four operation modes for microgrid are discussed and studied, that are grid-tie, island, islanding, and reconnection. In this chapter, a detailed discussion and analyses for microgrid operations are presented, including control strategies, modeling and simulation results according to each mode. The Chapter is organized as follows: Section 4.1 introduces a novel power management applied to the controls for wind and PV generations within the proposed microgrid. Section 4.2 and 4.3 present control and management for microgrid in grid-tie and island mode. In section 4.4, a novel comprehensive supervisory control unit (SCU) is proposed for managing microgrid transitions.

4.1 Power Management For Renewable Energy

When the renewable energy systems provide power to a microgrid, due to line impedance (which is significant in resistive component), they can change the bus voltage and move them out of range that will result in load tripping. Therefore, a novel power management for renewable energy has been implemented to regulate bus voltage. Figure 4.1 shows a one-line diagram of a distributed system with adding a renewable energy generation via line impedance. A considerable inductive line impedance and reactive load demand will lead to a dramatic voltage drop from feeder through load to renewable energy, as the renewable energy is typically regarded as current controlled source which doesn't provide voltage regulation. On the contrary, a dramatic voltage rise may occur due to an over generation of real power in a case of high penetration of renewable energy. In a word, a lack of providing reactive power most likely leads to low voltage issue, while an over providing of real power leads to high voltage problem.

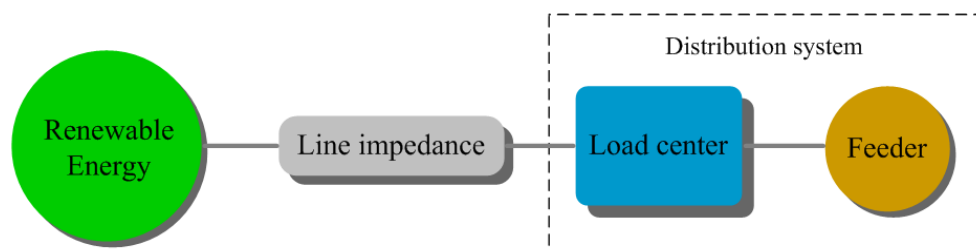


Figure 4.1: The one-line diagram of an example distributed system with adding a renewable energy generation via line impedance.

The renewable energy resources such as solar PV and wind power are usually inverter based sources which are able to control real and reactive power separately. However, in the industry, inverters designed for PV and wind are required to do only current control of q-axis in d-q frame to manage real power, while leaving reactive power by giving zero reference to d-axis. If an accurate decoupling is added to the control loop, a unit power factor will be achieved, which means the output reactive power is targeted as zero. Any inaccurate settings of decoupling function or variations of the parameters in the output filter due to the temperature deviation lead to an uncontrollable reactive power offset. The higher the real power is output, the higher the reactive power deviation is observed. In this paper, a decoupled P/Q controlled inverter with voltage and frequency constraints is designed and implemented, which has been discussed in Chapter 3. It allows the renewable resource to regulate not only real power but also reactive power. But it is worthy to notice that to manage the reactive power for renewable energy resources, four constraints are required to be applied as described in equations 4.1.1 - 4.1.4.

$$\sqrt{(P_{out}^2 + Q_{out}^2)} \leq S_{inv} \quad (4.1.1)$$

$$PF \geq 0.5 \quad \text{When } P_{out} \geq 0.29p.u. \quad (4.1.2)$$

$$Q_{out} \leq 0.5 \quad \text{When } P_{out} < 0.29p.u. \quad (4.1.3)$$

$$\begin{aligned} \frac{1}{2\pi(6f_{ac})C_{dc}} \cdot \frac{Q_{out}}{V_{dc}} &\leq V_{max_ripple} = \eta\%V_{dc} \\ \implies Q_{max_out} &\leq 12\pi f_{ac}C_{dc}\eta\%V_{dc}^2 \end{aligned} \quad (4.1.4)$$

Firstly and obviously, the total delivered apparent power must not exceed the rating of the inverter (equation 4.1.1). Equation 4.1.2 and 4.1.3 give out the reactive power limits for different conditions that a border line for power factor (PF) of 0.5 and 0.5 per unit of reactive power is selected. It aims to reduce the stress on the diodes of the inverter. When the inverter has sufficient real power to output (0.29 per unit as calculated), the reactive power is limited by the power factor of 0.5 (both lagging and leading conditions). When inverter provides the real power less than 0.29 per unit, the output reactive power is limited by a hard limiter of ± 0.5 per unit. In addition, the maximum output reactive power is also limited to the requested limitation of DC-link voltage ripple, which can be approximately calculated in equation 4.1.4 [36], where C_{dc} is the capacitance of DC-link and η is the allowable percentage of DC voltage ripple.

The objective of power management for renewable energy is to regulate its terminal voltage within an allowable range (eg. 0.96p.u. - 1.04 p.u.) as much as it can by manipulating the output reactive power considering the constraints, and by curtailing the real power if necessary. The control priority of reactive power is higher than that of real power as a high power penetration of renewable energy is always wanted. A selectable voltage PI regulator for real and reactive power is designed and added to

the inverter for renewable energy.

A series comparison of with and without the proposed power management for renewable energy are shown in following figures. Figure 4.2 shows the power profile of a 500kW solar PV plant when it is installed at bus 848. From 7AM through 1PM, the voltage of the PV bus exceeds 1.05 per unit in Figure 4.3. Figure 4.4 gives the active and reactive power received from the grid through bus 800. The signature of the solar PV generation can be seen on the imported grid power curve.

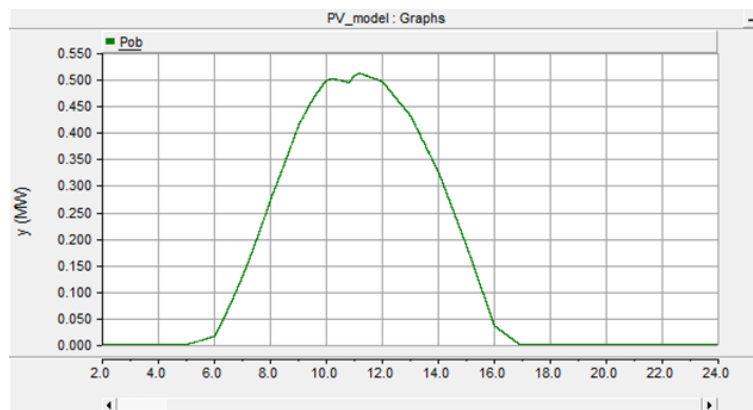


Figure 4.2: The power profile of the 500kW PV solar.

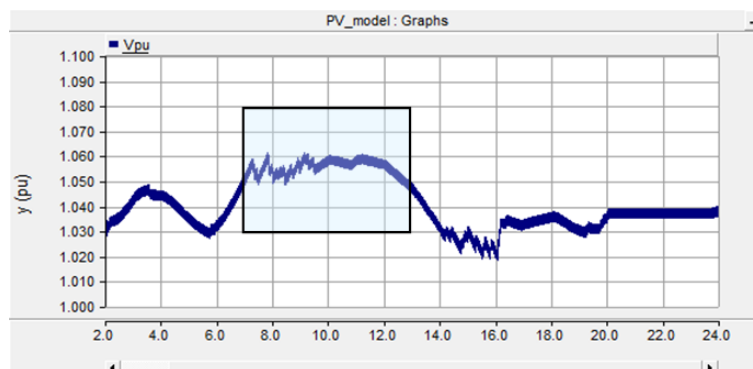


Figure 4.3: The per unit voltage at PV terminal.

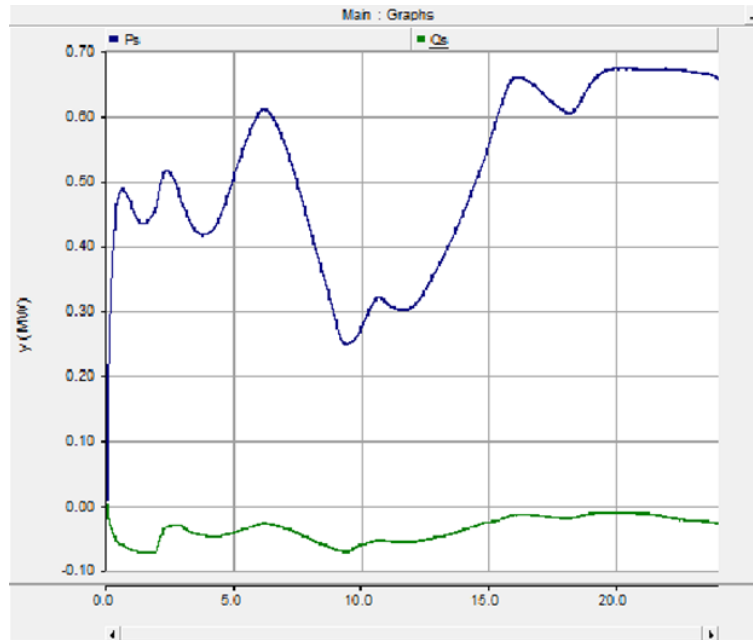


Figure 4.4: The real and reactive power received from the grid.

Figure 4.5 through 4.7 show the waveforms of the system when power curtailment is applied. In order to reduce the PV power, the inverter increases the terminal voltage of the PV array. This will move the PV away from its MPPT and reduces the generated power. As indicated in Figure 4.5, the power curtailment is activated right before 8AM. By reducing the PV power, the voltage at bus 848 is limited at 1.05 per unit as indicated in Figure 4.6. The comparison should be made in the highlighted windows on Figure 4.3 and 4.6. Figure 4.7 shows the active and reactive power received from the grid in this case. The imported power from the grid increases compared with previous case presented in Figure 4.4.

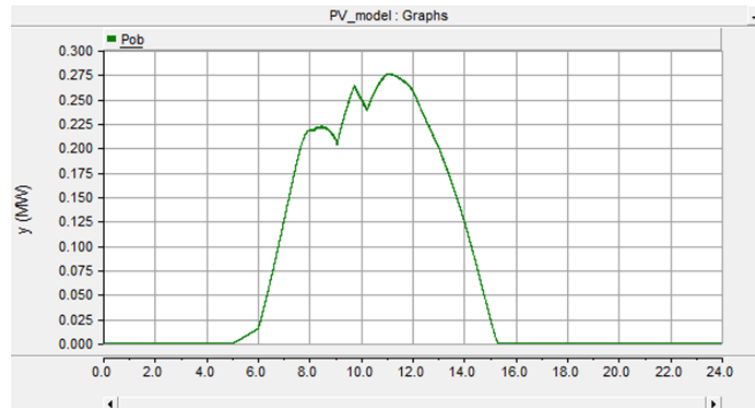


Figure 4.5: The solar PV power profile after real power curtailment applied.

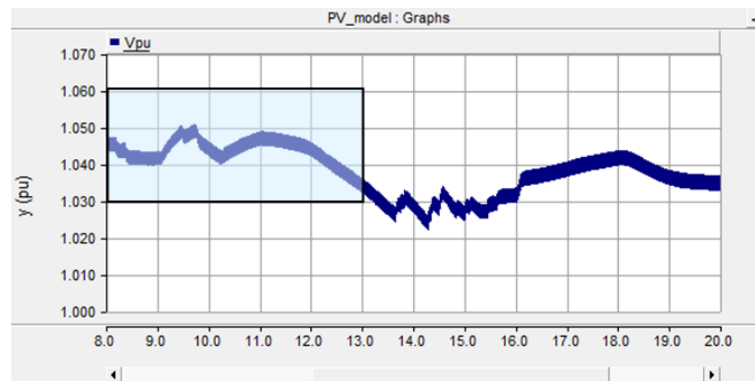


Figure 4.6: The per unit voltage at PV terminal after power curtailment.

In addition to curtailing the active power, the voltage can be regulated by adjusting reactive power. However, the total apparent power of the inverter cannot exceed its nominal rating. If the wind or solar inverter absorbs reactive power while curtailing the active power, we can increase the active power delivered by the renewable sources and keep the bus voltages within the limits. Figures 4.8 through 4.10 show the results when both power curtailment and reactive power management are applied. The PV inverter absorbs reactive power to lower the bus voltage in order to

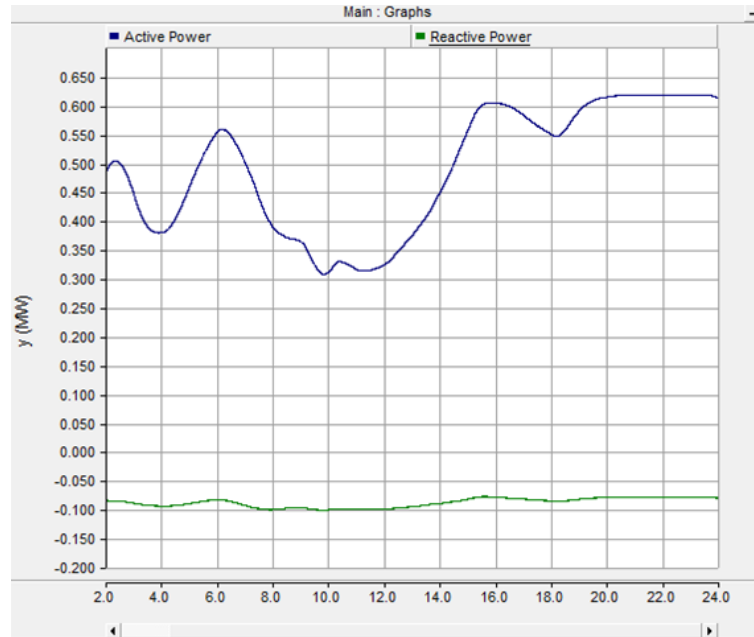


Figure 4.7: Active and reactive power received from the grid after power curtailment.

inject more power to the microgrid. Figure 4.8 shows the active and reactive power delivered by the solar PV system. The PV bus voltage is limited at 1.05 per unit as indicated in Figure 4.9. Figure 4.10 shows the reduction in active power and increase in reactive power received from the grid.

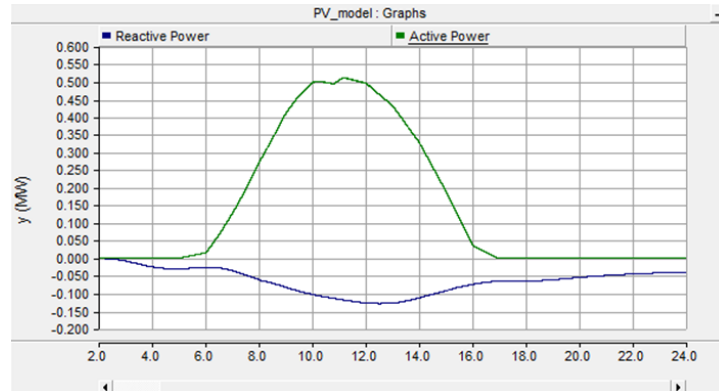


Figure 4.8: The managed real and reactive power profile of solar PV.

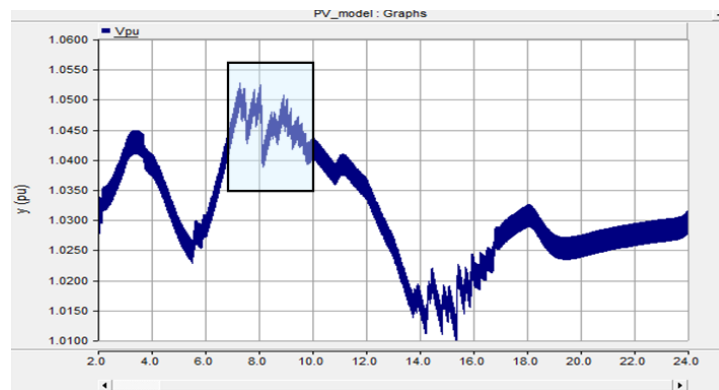


Figure 4.9: The per unit voltage at PV terminal after power curtailment and reactive power control.

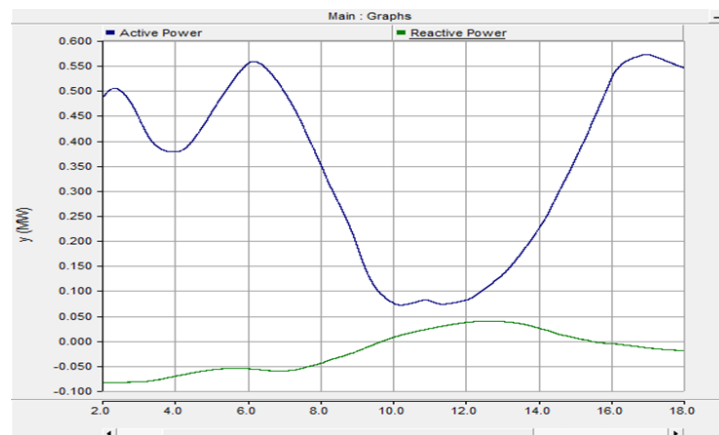


Figure 4.10: Real and reactive power received from the grid after power curtailment and reactive power control.

To sum up the three cases shown in Figure 4.2 - 4.4, Figure 4.5 - 4.7, and Figure 4.8 - 4.10, respectively, it is obviously that the last case is the best one because the terminal voltage is controlled in the designed safe range compared with first case, and also the output real power is higher than that of in second case as the high penetration is always expected.

The similar simulation and comparisons are also conducted for a 1MW wind power installed at bus 890 shown as follows. Figure 4.11 shows the wind power profile and voltage at bus 890 for a 24-hour period. The nominal wind speed of the turbine is 12m/s. The wind power reaches and stays at 1MW starting 12PM. The wind turbine bus voltage exceeds 1.05 per unit starting 11AM.

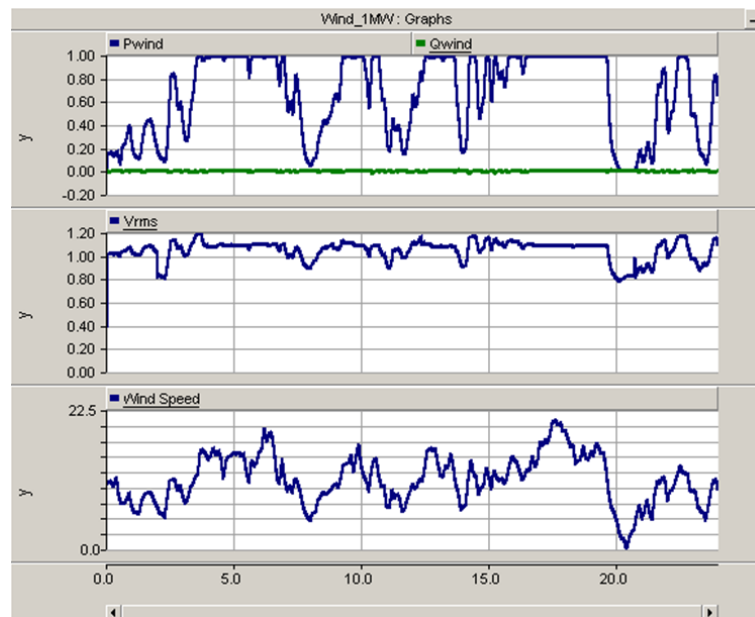


Figure 4.11: The results for wind power and bus voltage without wind power curtailment: from top, turbine active and reactive power, bus voltage, and wind speed.

Figure 4.12 shows the power profile and wind turbine bus voltage after power curtailment control is applied. In order to reduce the output power of the turbine, the grid side converter reduces the power export to the grid. This will increase the rotor speed since the incoming wind power is unchanged. To reduce the mechanical incoming power, pitch control is applied to increase the pitch angle. Utilizing this control, the bus voltage is maintained under 1.05 per unit.

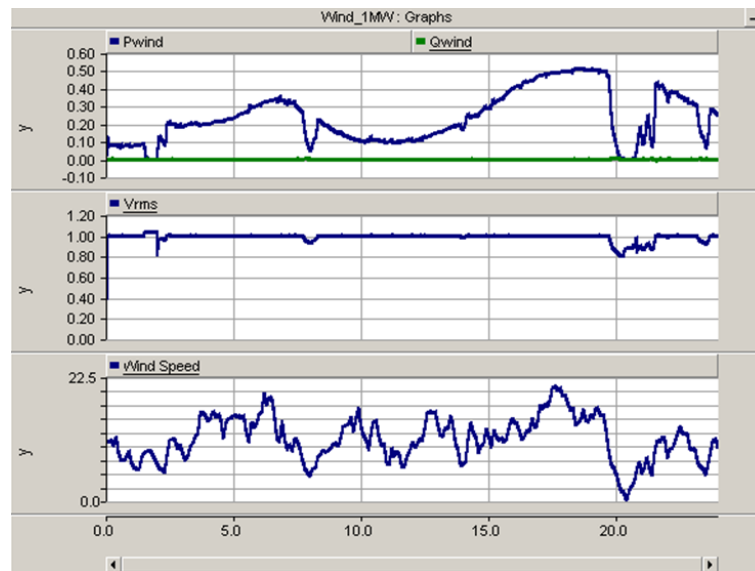


Figure 4.12: The results for wind power and bus voltage with wind power curtailment: from top, turbine active and reactive power, bus voltage, and wind speed.

Figure 4.13 shows the case for power curtailment and reactive power control for the 1MW wind turbine. The bus voltage is kept under 1.05 per unit and the active power delivery is significantly increased compared with the case in Figure 4.12.

In addition to preventing the over voltage cases, the reactive power compensation can support the microgrid in case of under voltage. This can be seen in Figures 4.11

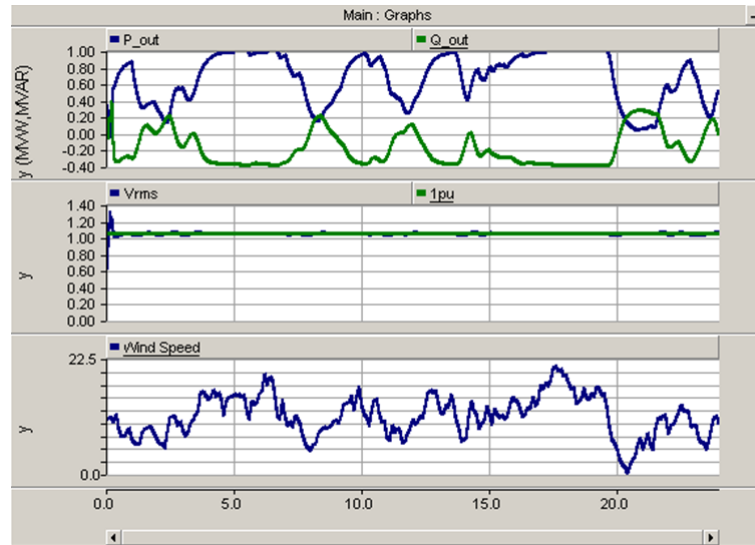


Figure 4.13: The results for wind power and bus voltage with wind power curtailment and reactive power control: from top, turbine active and reactive power, bus voltage, and wind speed.

- 4.13 around hour 21.

4.2 Autonomous Control for Microgrid in Grid-tie Mode

When the microgrid is connected to the grid, the operation of distributed generations and power management are straightforward. In this mode, natural gas generator is disabled but stood by for islanding. Energy storage system is connected to the system but doing nothing expect for charging if required. Renewable energy resources, which are one of 250kW solar PV generation and two of 750kW wind generations in

the system, are providing power following the power management method aforementioned. A 24 hours simulation of the proposed microgrid in grid-tie mode has been conducted. The solar irradiation and wind speed profiles as well as the load profiles are imported by using the real data shown in Chapter 2. The simulation results are shown in following figures.

Figure 4.14 shows the real and reactive power delivered by PV. The real power of the PV is not curtailed due to the more stable system compared with the islanded mode. The delivered reactive power is observed when the PV terminal voltage drops below 1 per unit. A hard limit of 0.5 per unit for reactive power is seen around 8pm to 10pm when there is no output real power. A 0.5 power factor limitation for reactive power management is observed around 8 am. (The power factor at 8am is approximately computed by $\cos(\arctan(\frac{Q}{P})) = \cos(\arctan(\frac{0.175}{0.1})) \approx 0.5$). The lowest voltage at PV terminal, which is about 0.95 per unit shown in Figure 4.15, occurs around 8pm to 10pm when there is no power generated by both PV and wind sources.

Figure 4.16 shows the real and reactive power of the 0.75 MW wind turbine connected to bus 840. The same power management approach is applied for two wind sources. By comparing with the power profile shown in Figure 2.7(in Chapter 2), the difference of real power is due to the power curtailment as the bus voltage violates the setting limit of 1.04 per unit and reactive power reaches constraints shown in equation 4.1.1 - 4.1.4. It is worthy to notice that the delivered real power has never

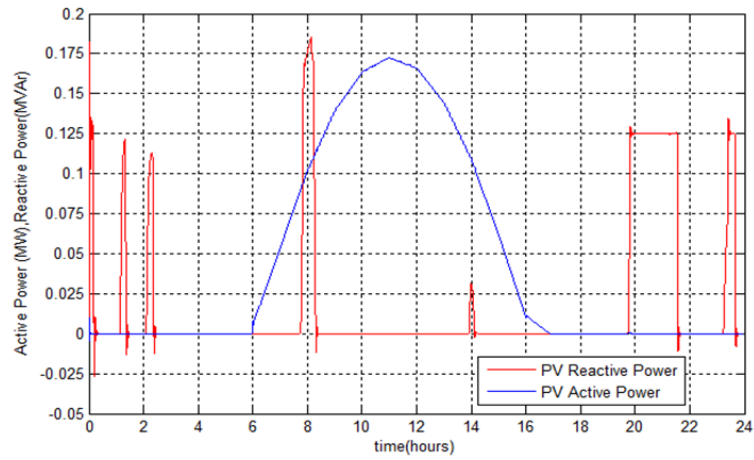


Figure 4.14: The real and reactive power of the solar PV in grid-tie mode.

reached the rated value of 0.75MW, which means the cables for delivering wind power need to be re-sized to reduce the voltage deviation affected by the required power flow.

The real and reactive power received from the grid at bus 800 is shown in Figure 4.17. A considerable amount of reactive power provided by the bulk grid is observed when the high voltages occur at the terminals of inverters of renewable resources, because the inverters absorb reactive powers to try to manage their terminal voltages. The worst voltage profile in this case is observed at bus 822 which is a single phase bus and is far from all the generations. Figure 4.18 shows the voltage profile of bus 822 in grid connected mode, which is in acceptable range.

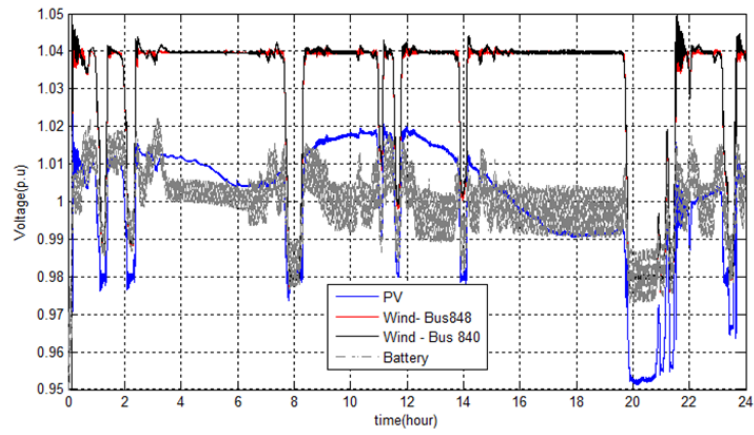


Figure 4.15: Voltages at renewable source buses in grid-tie mode.

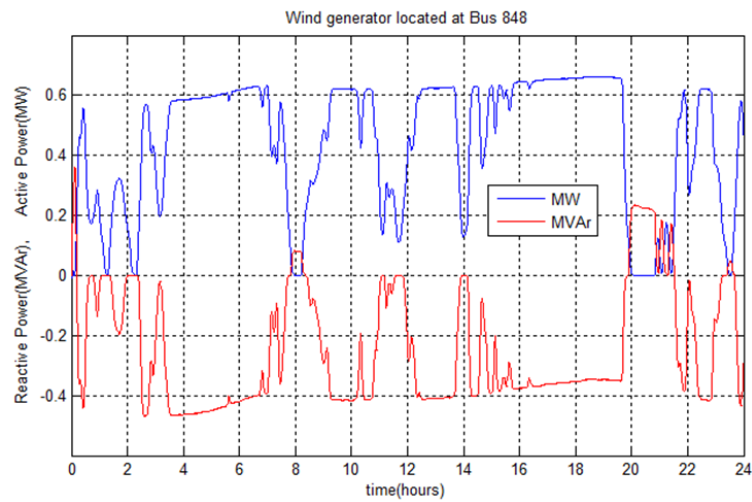


Figure 4.16: The real and reactive power of the wind turbine on bus 840 in grid-tie mode.

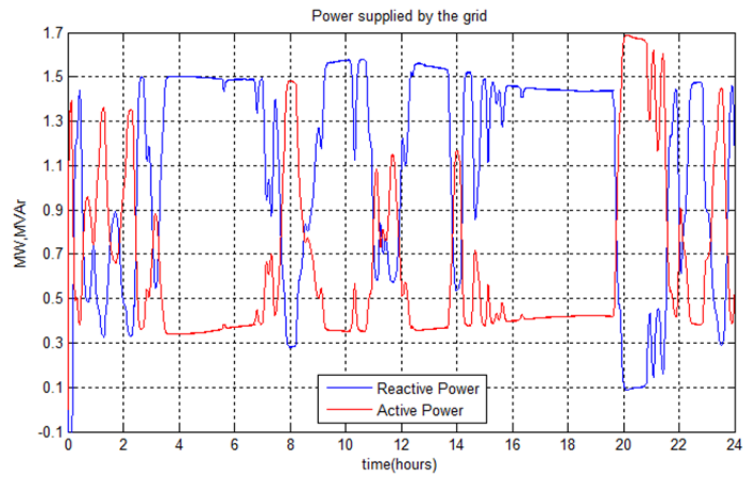


Figure 4.17: The real and reactive power delivered by the grid to the system.

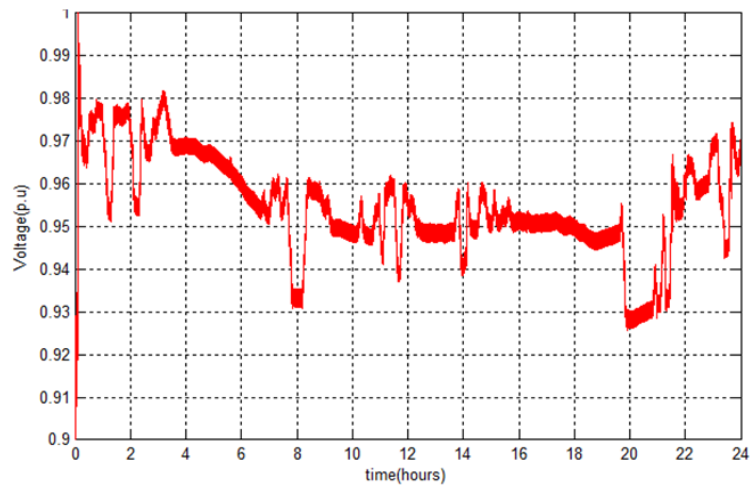


Figure 4.18: Voltage profile at bus 822 of the system during grid-tie mode.

4.3 Droop Control for Microgrid in Island Mode

To model the described microgrid system in island mode, the primary control is to adjust the real and reactive power of all the sources to regulate the frequency and voltage of the system. The secondary control is to maximize the power capture from the renewable energy resources thus to minimize the energy delivered by the natural gas generator. A droop control is designed for energy storage system (battery) and natural gas generator to coordinate the sources in order to regulate the system frequency. The natural gas generator power is forced to zero when the frequency reaches 61Hz as shown in Figure 4.19, which represents a condition of light load and high renewable energy. The maximum output power is reached when the frequency drops to 59Hz which indicates the system in a heavy load and a light renewable energy condition. The battery starts absorbing power when frequency exceeds 60.5 Hz and provides power when the frequency falls under 59.5Hz. However, the battery has a discharge rating of twice as its charging capability. A zero power region designed for battery in the frequency bandwidth between 59.5Hz and 60.5Hz is to reduce the charging and discharging cycles when the microgrid moves slightly up and down to the nominal situation. By this approach, the life time of battery will be apparently enlarged. A proportional integrator (PI) controller is designed to curtail the wind power when the frequency exceeds 60.8 Hz. For the solar PV, the curtailment starts at 60.9 Hz. The sources are divided into droop-controlled and PI-controlled in order

to prevent oscillations in the system frequency and to maximize the energy delivered by the renewable sources.

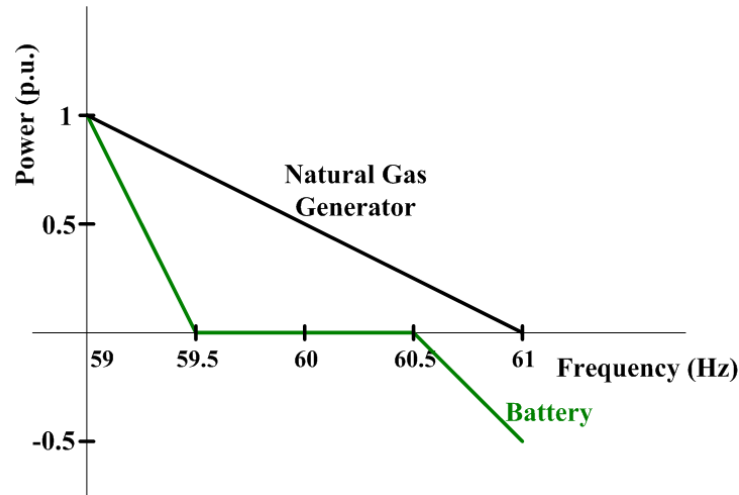


Figure 4.19: The real power droop mechanism for natural gas generator and battery in the microgrid.

When a source delivers real power, the voltage at its terminal and adjacent buses rises due to line impedances. However, if the source consumes reactive power, the terminal voltage may decrease due to line reactance. This concept has been utilized to regulate the bus voltages. A droop control mechanism has been defined for natural gas generator, solar PV and battery. The natural gas generator ceases to produce reactive power when its terminal voltage reaches 1.05 p.u., as shown in Figure 4.20. It will generate 1 p.u. of reactive power when the terminal voltage drops to 0.95 p.u. The battery inverter and solar PV inverter will also provide reactive power when their terminal voltages drop under 1 p.u. The solar PV inverter absorbs reactive power to lower the voltage when it exceeds 1 p.u.

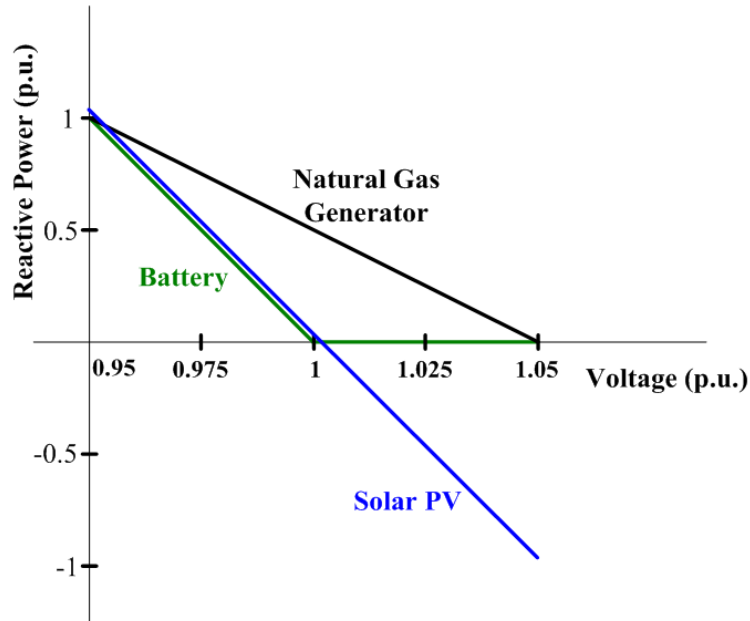


Figure 4.20: The reactive power droop mechanism for natural gas generator, solar PV and battery in the microgrid.

The reactive power of the wind generator is regulated using a PI controller in order to prevent fighting between sources to adjust the voltage. It controls the reactive power to adjust the terminal voltage at 1 p.u. The reactive power constraints aforementioned are always actively applied for all inverter interfaced generations.

A 24 hours simulation similar to grid-tie mode for the proposed microgrid is again conducted in the island mode, but with different controls. According to the transition issues between grid-tie and island will be discussed in the following section. The results for the island microgrid in 24 hours using the same power profiles with the grid-tie case are shown as follows.

Figures 4.21 - 4.24 show the real and reactive power delivered by the solar PV,

wind, storage, and natural gas generator. The solar PV power is almost at its maximum capability as shown in Figure 4.21. There are some instances (e.g. during noon) that PV has to provide reactive power in order to improve the voltage and consequently, it has to reduce the real power. The voltage problem is mainly caused by a fast varying wind power. All the sources including storage and natural gas generator contribute reactive power to improve the voltage at those instances.

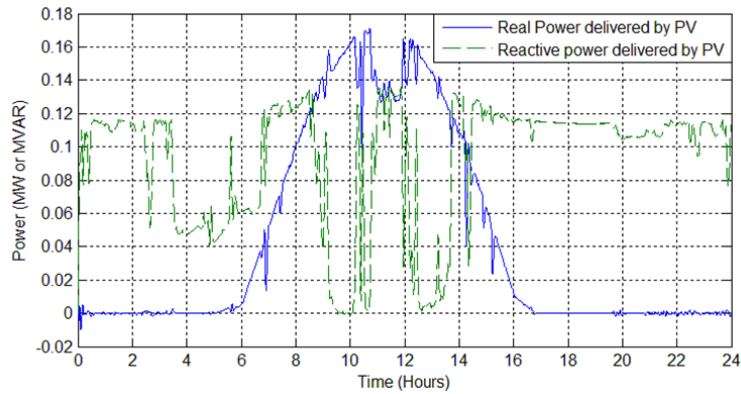


Figure 4.21: The real and reactive power delivered by 0.25MW solar PV.

It should also be noted that the inverter-based sources have a maximum current capability to protect the switches. When the system voltage drops, their capability to export real and reactive power drops proportionally. This can be seen at 8PM when the PV terminal voltage is low due to drop in wind power but the PV inverter cannot contribute 1 p.u. of reactive power since its terminal voltage is around 0.9 p.u.

The energy storage device charges and discharges to support the system frequency in different cases. For instance, after 8PM, the storage supports the system with full power since there is a large drop in wind power. When the wind energy is at maximum

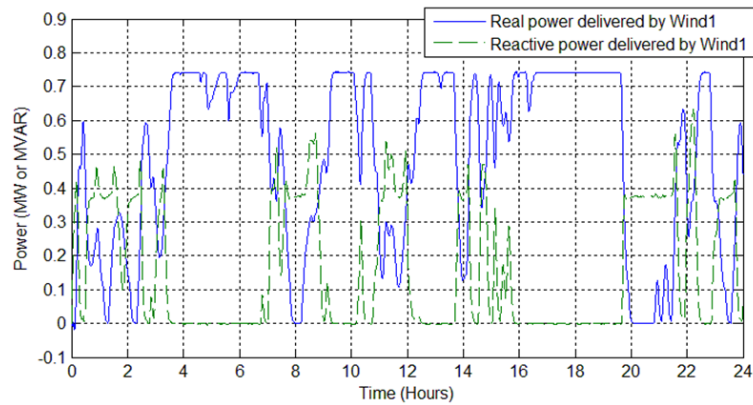


Figure 4.22: The real and reactive power delivered by one of the 750kW wind turbines.

(e.g. before 5AM), it absorbs power to adjust frequency.

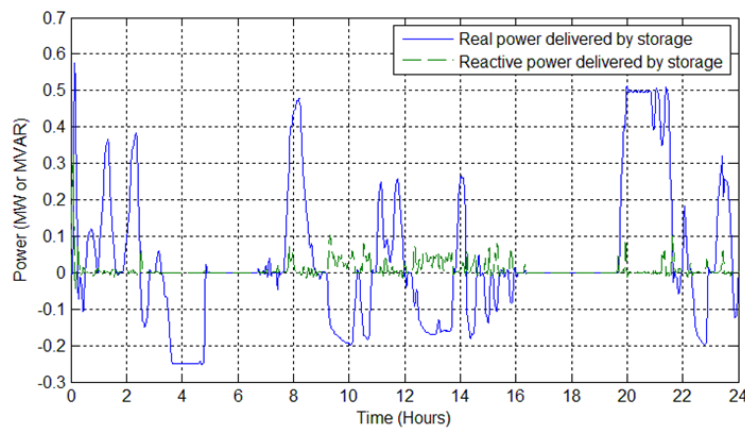


Figure 4.23: The real and reactive power delivered by two 250kW battery storage systems.

The natural gas generator supports the system when renewable energy systems do not provide enough power to support the demand. It also provides reactive power to support the voltage.

Figure 4.25 shows the voltage at bus 822, which experiences the lowest voltage profile in the system due to long lines. The voltage stays in the acceptable range

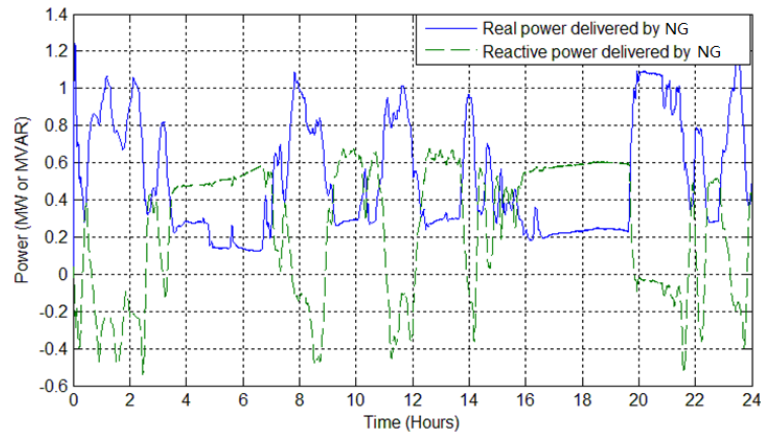


Figure 4.24: The real and reactive power delivered by 1.5MVA natural gas generator. during all 24 hours. However, voltages of solar PV and wind buses drop under 0.92 p.u. in several instances, as shown in Figure 4.26.

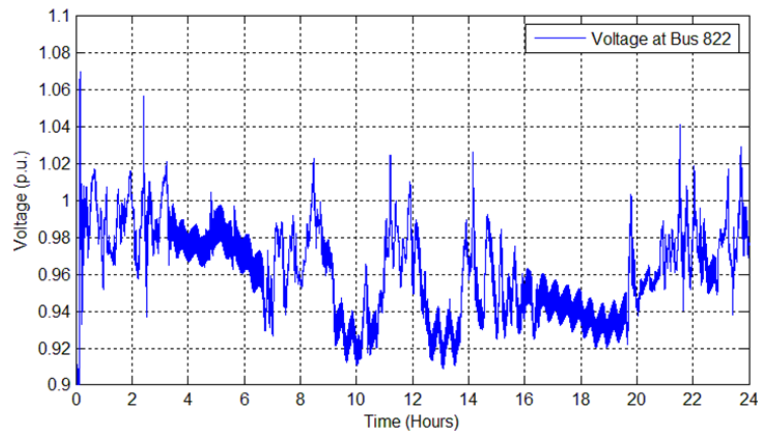


Figure 4.25: Voltage profile at bus 822 of the system.

To improve the voltage profile for the renewable sources, a voltage regulator has been added between buses 832 and 852. There are several impedance loads in the system as mentioned earlier. By improving the voltage, the demand of those impedance loads increases. Right after 8PM, when wind power decreases to zero, natural gas

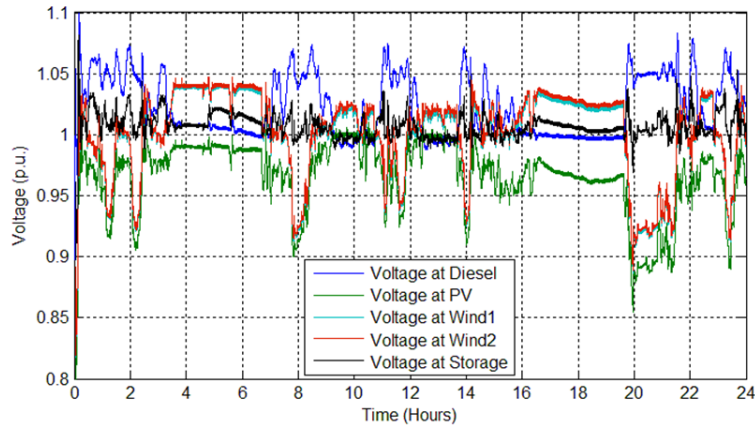


Figure 4.26: Voltage profile of all sources in the system.

and storage cannot meet the system demand. Therefore, the frequency of the system collapses as shown in Figure 4.27. Due to long transmission lines between natural gas generator and major loads, the loss in the system increases when renewable resources are not providing power. That adds more stress on the natural gas generator to supply the demand.

A solution to this problem and to improve the voltage near renewable energy sources is to move the energy storage device closer to these sources. For instance, if the storage is moved from bus 828 to bus 832, it can provide voltage support to renewable sources and supply the adjacent loads when power from these sources decrease. In addition, this will reduce the loss in the long distribution line between buses 852 and 854. Figure 4.28 shows the voltage profiles of the sources in the system when the storage is move to bus 832. All voltages remain in the acceptable range. However, the voltage of some loads, e.g. load at bus 822, drops under 0.88 p.u.

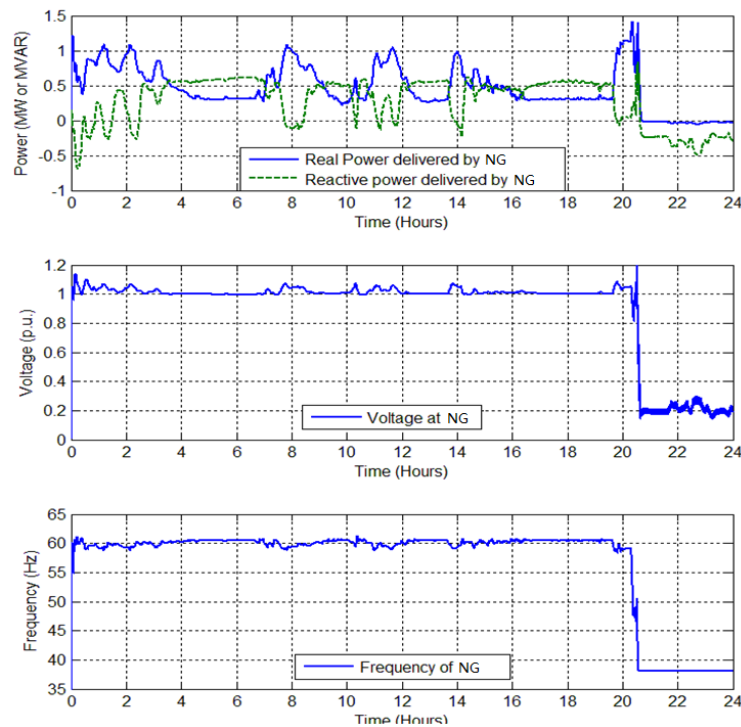


Figure 4.27: The real power, reactive power, voltage, and frequency of the natural gas generator when a collapse in the system occurs.

when there is a large drop in wind power. The voltage profile of bus 822 is provided in Figure 4.29. In addition, this method limits the energy delivery of wind turbine connected to bus 840.

An alternative solution to the problem is to move the storage to bus 832 but do not add the regulator between buses 832 and 852. This solution results in better voltage profile for the system and allows more energy delivery from renewable sources.

Figure 4.30 shows the voltage profile of the sources when the storage is moved to bus 832. All the voltages are again in acceptable range. The voltages of all loads are also in the acceptable range. Figure 4.31 shows the total load, generation, and loss in

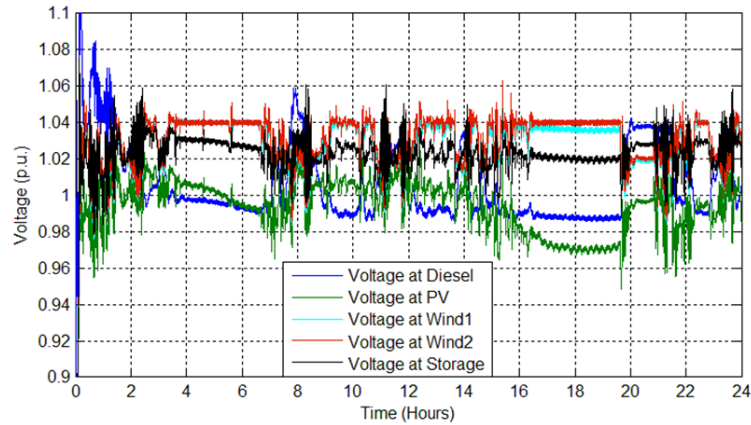


Figure 4.28: Voltage profile of sources when a regulator is added and storage is moved to bus 832.

the system. The total loss of the system is less than the case when storage is placed on bus 828.

Another solution to the problem is to apply load shedding at buses near renewable energy sources to improve voltage profile. This method is not desirable since it lowers the energy surety of the system and reduces the energy delivered by renewable resources.

The aforementioned studies about the location of battery indicate the importance of optimizing the battery placement. A power system planning study on optimal sizing and locating of energy storage system is continuing after this project. A method by using voltage sensitivity analysis has been proposed and will be published. A combination of voltage sensitivity analysis and particle swarm optimization is proposing and studying.

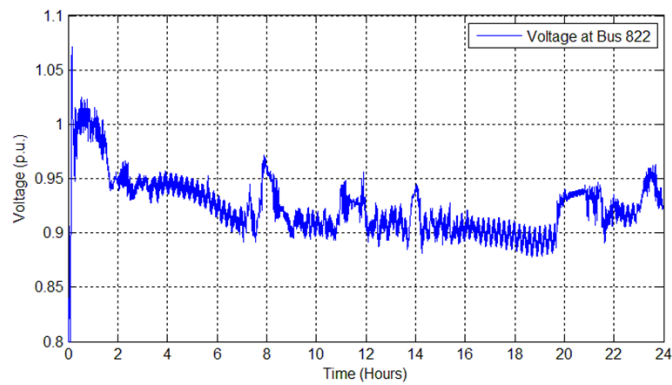


Figure 4.29: Voltage profile of bus 822 when a regulator is added to the system and energy storage is moved to bus 832.

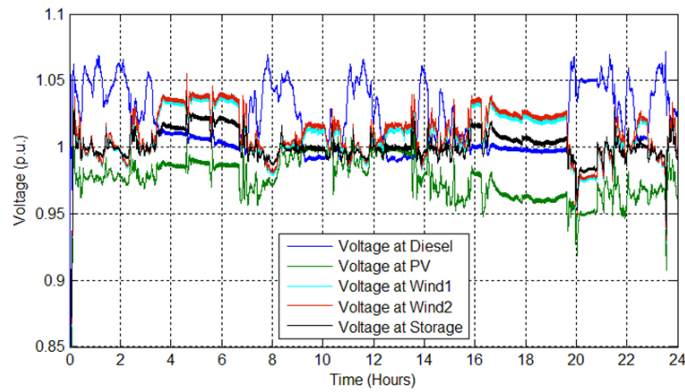


Figure 4.30: Voltage profile of sources when storage is moved to bus 832.

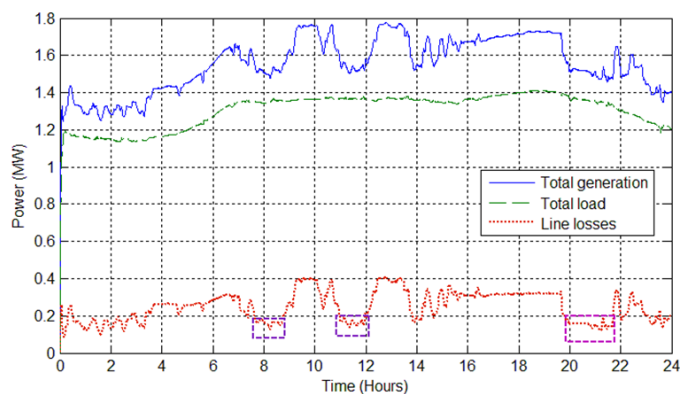


Figure 4.31: Total generation, load, and loss in the system when storage is moved to bus 832.

4.4 Supervisory Control for Microgrid Transitions Using Low Bandwidth Communication

In this section, a novel supervisory control scheme using low bandwidth communication is proposed. And the microgrid transition issues between grid-tie mode and island mode are studied and concluded. The section is divided into 5 sub-sections: An overview of the proposed supervisory control scheme, Matlab function interface design in PSCAD to emulate Supervisory Control Unit (SCU), microgrid islanding (include intentional islanding and unintentional islanding), microgrid reconnection and black start.

4.4.1 An Overview of the Proposed Supervisory Control Scheme

In the paper, an innovative and comprehensive power management for online microgrid operation is proposed and developed by combining the local control of each distributed generation (e.g. P/Q or v/f regulation or droop control) and a supervisory control with low bandwidth communication. The diagram of the proposed scheme is shown in Figure 4.32. The supervisory control unit (SCU) is designed for monitoring the microgrid all the time, but managing the microgrid only during transition processes. SCU is programmed in Matlab environment interfacing with microgrid modeled in PSCAD. The flow chart is shown in Figure 4.33. The benefits

of this approach are: (i) The loss of communication is a big concern in the microgrid development. This approach minimize the risks, repair costs and potential damages that are brought by the communication loss issue. Because the microgrid is able to survive in both grid-tie mode and island mode without communication, the online communication test and repair are allowed. Besides, if the communication signals are lost during intentional islanding or reconnection, the microgrid moves to grid-tie mode or island mode automatically.

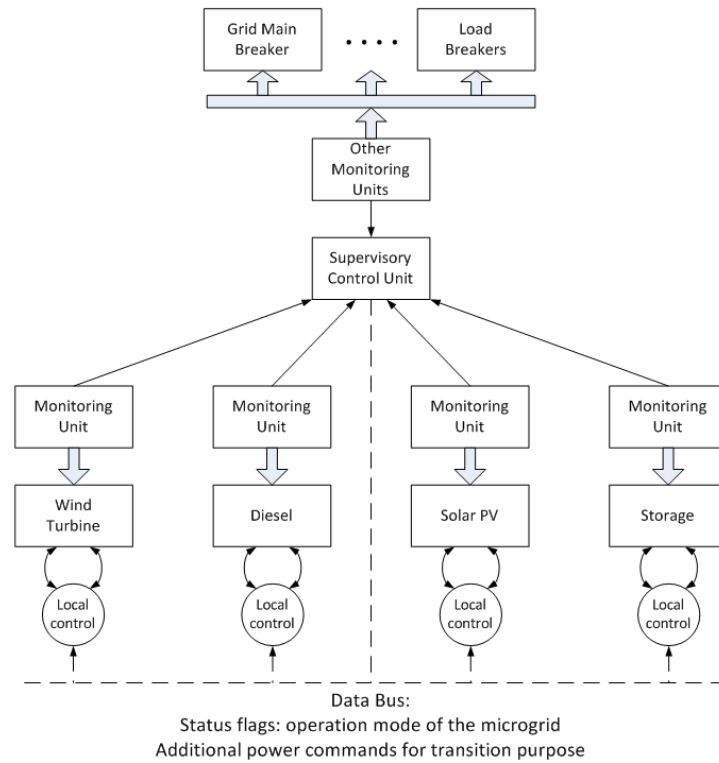


Figure 4.32: The diagram of proposed supervisory control scheme.

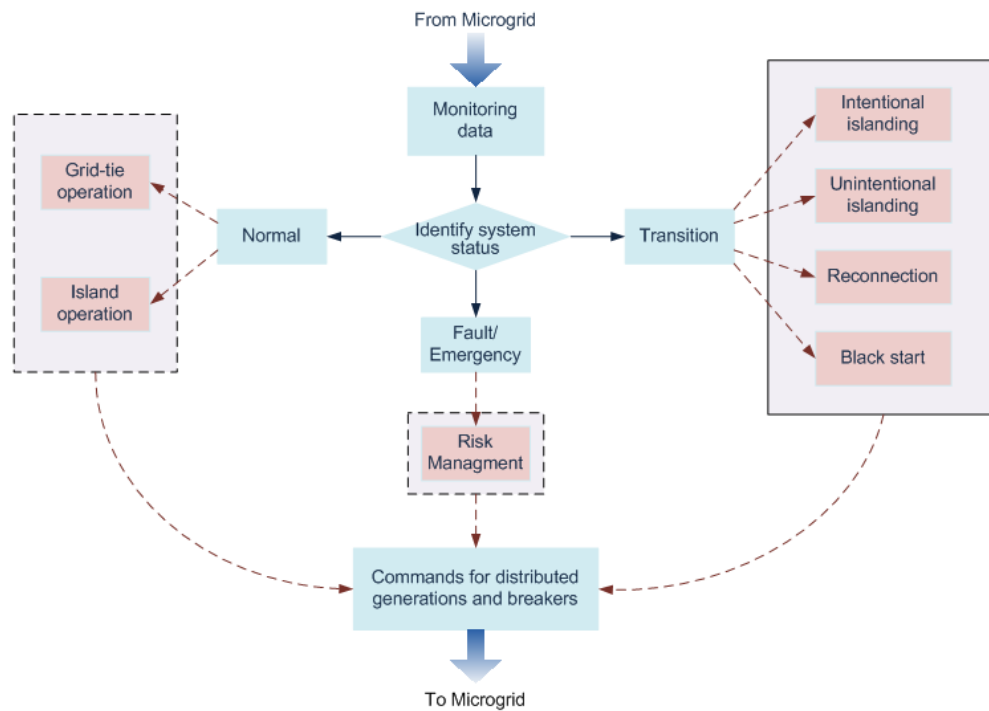


Figure 4.33: The flow chart of supervisory control unit.

(ii) The communication signals transmitted between supervisory control unit and generations and loads use compressed data format instead of real or normalized values. Each command signal may take 1-3 bits to represent the pre-defined information vary from different purposes. For instance, a regular power command needs only 2 bits to represent roughly or finely increase or decrease, instead of a 8-bit or 16-bit accuracy normalized value. An example of data format of signal transmitted from SCU to natural gas generator is given in Figure 4.34. A 16-bit word fully represents all required information (communication status, operation mode, start/stop) and commands (P, Q, v, f) for natural gas generator in the proposed supervisory control

algorithm. After receiving it, natural gas generator is able to judge and adjust its operation during microgrid transitions. For example, during intentional islanding, a command of #0200 (BCD code) tells natural gas generator to run in the mode of P/Q adjustment with roughly increasing of real power and finely decreasing of reactive power. The definition of data format is described in Table 4.1.

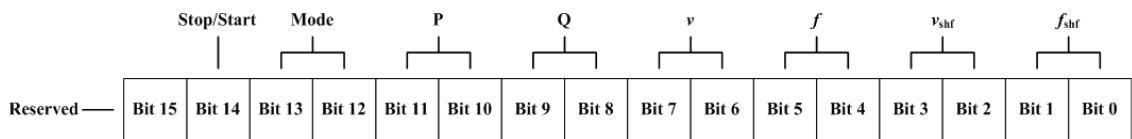


Figure 4.34: The proposed data format for the signal transmitted from SCU to natural gas generator.

Bit 15: Reserved bit for communication status (0-normal; 1-abnormal)

Bit 14: Stop/Start command for natural gas generator (0-start; 1-stop)

Bit 13-12: Operation mode selection

Bit 11-10: Real power adjustment command

Bit 9-8: Reactive power adjustment command

Bit 7-6: Voltage magnitude adjustment command

Bit 5-4: Frequency adjustment command

Bit 3-2: Shift command for voltage magnitude

Bit 1-0: Shift command for frequency magnitude

Table 4.1: The true table of commands for natural gas generator.

	Mode Selection (Bit 13-12)	$P, Q, v, f, v_{shi}, f_{shf}$ (Bit 11-0)
00	P/Q Adjustment	Up (Roughly)
01	v/f Adjustment	Up (Finely)
10	Shifting Droop	Down (Finely)
11	Reset v/f	Down (Roughly)

Lets approximately estimate and compare the minimum bandwidth for a traditional data format and the proposed data format. Assuming that there are 5 generations within the microgrid, and each generation needs 6 control commands of P, Q, v, f, v_{shf} and f_{shf} . 16-bit accuracy (0 65535 for unsigned value, and -32767 32768 for signed value) is adopted. A 10ms communication delay is employed. For a traditional data format, a minimum bandwidth of $5 \times 6 \times 16 \times (1/0.01) = 48,000$ *bps* is required, compared with $5 \times 16 \times (1/0.01) = 8000$ *bps* for that of proposed data format.

(iii) Although in the paper, the proposed supervisory control scheme is only employed for microgrid transition management, it is technically allowed to adjust distributed generations in grid-tie and island mode, so that any advanced optimal operations such as optimal load flow or economic dispatch are able to be applied to achieve better performance for the microgrid.

4.4.2 Matlab Interface Designed for PSCAD

The power system simulator product PSCAD provides Graphic Use Interface (GUI) for user to build the system. With built-in electric components, miscellaneous functions, and file I/O etc., researchers can easily establish the power system and do various analyses such as power flow, short-circuit, fault protection and so on. However, it is not as easy as other language based simulators to program to realize a complex algorithm. Fortunately, PSCAD is capable of interfacing with Matlab, so that, in the paper, the electrical circuits of microgrid and analog control blocks are built in PSCAD while the advanced control algorithms like supervisory control is programmed in Matlab function but called by PSCAD when the system is running. How to build a Matlab module in PSCAD is illustrated in the following example.

In this example, a single phase 1kV/60Hz power source is connected to a 1kW /0.5kVar load. By sending the voltage and current signal to Matlab interface module, the instantaneous power is calculated in Matlab environment. The result is returned to and plotted in PSCAD. The diagram in PSCAD is shown in Figure 4.35. The waveform of returned instantaneous power is shown in Figure 4.36.

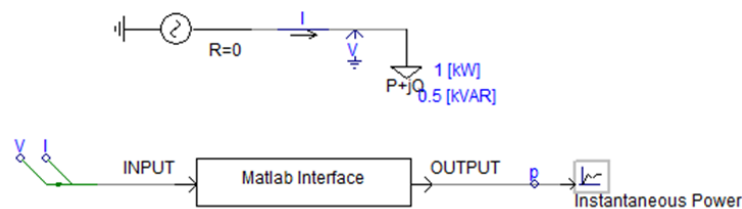


Figure 4.35: An example of Matlab interface module in PSCAD.

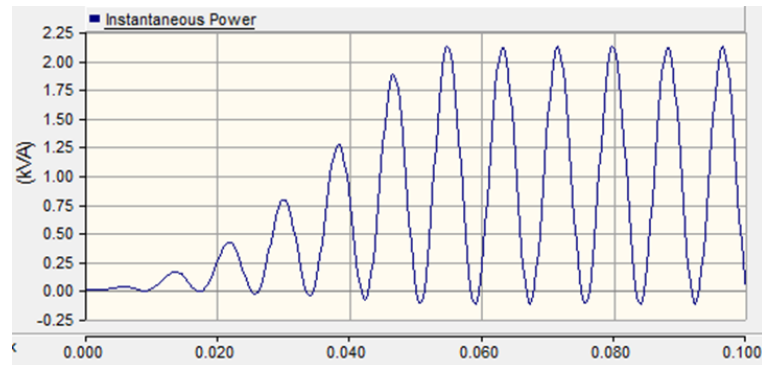


Figure 4.36: The result power waveform returned by Matlab and plotted in PSCAD.

Taking this case for example, the key steps of setup Matlab interface are as follows.

1. Create a component specifying input and output attributes such as name and number of ports, data dimensions, and data types.

2. Add three basic parameters for the module shown in Figure 4.37, which will let user configure the path and name of the .m files when double click the Matlab Interface module shown in Figure 4.38. It is worthy to notice that the last parameter Enabl allows PSCAD to enable or disable the module during simulation. By giving a 0-1 pulse signal to it, PSCAD is able to run asynchronously to Matlab.

Matlab File Name	Text
Description	Matlab File Name
Symbol	Name
Relative Path of .m File	Text
Description	Relative Path of .m File
Symbol	Path
Enable=1, Disable=0	Real
Description	Enable=1, Disable=0
Symbol	Enabl

Figure 4.37: Screenshot of the parameters setting for Matlab interface module.

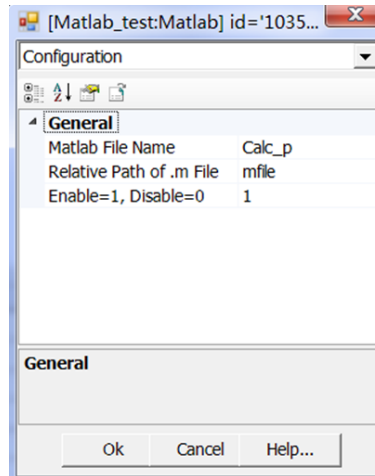


Figure 4.38: Screenshot of the configuration window for Matlab interface module.

3. Add following script to the Script property. Be aware of name and number of input and output variables.

```

!Assign memory for all variables
#STORAGE REAL:3
!Define Local variables
#LOCAL INTEGER I_CNT
    IF($Enabl.GT.0.9) THEN
        I_CNT = 1
!Assign memory for input variables
        DO WHILE(I_CNT.LE.2)
            STORF(NSTORF+I_CNT-1) = $input(I_CNT)
            I_CNT = I_CNT + 1
        END DO
!Call Matlab
        CALL MLAB_INT(":%Dir\$Path", "$Name", "R(2)", "R")
    ENDIF
!Assign memory for output variables
    $output = STORF(NSTORF+2)
!
    NSTORF = NSTORF+3

```

4. Create a file named Calc_p.m in Matlab and program as a function shown as follow. The name and the path of the file must match the configuration settings in PSCAD.

```
%Test of interfacing with PSCAD
function [output] = Calc_p(input)
%Data extraction
Volt=input(1);
Curr=input(2);
%Calculation
p=Volt*Curr;
%Return
output=p;
```

4.4.3 Microgrid Islanding

Both types of microgrid islanding, intentional and unintentional, are studied in this section. Intentional islanding may occur due to scheduled grid outage or maintenance issues. Unintentional islanding is a more complex case and may be required due to grid faults, unscheduled outages, and voltage or/and frequency transients.

Active and reactive controls functions for DGs are different in grid-tie and island modes. During transition, some changes in control functions must be applied. For instance, in grid-tie mode, natural gas generator is off, solar PV and wind are following Maximum Power Point Tracking (MPPT). At the same time, they react to voltage variations on their feeders by adjusting their reactive power. Energy storage operates in voltage mode but does not participate in droop functions.

In island mode, natural gas generator is connected. Battery and generator are

operating in voltage mode and their active power is following frequency droop control. Active power for renewable sources still follow MPPT, however, in some cases they may need to curtail their power to stabilize the voltage. Reactive power for all the sources follows voltage droop control. The active and reactive power control functions for energy storage and reactive power for renewable sources must change during transition.

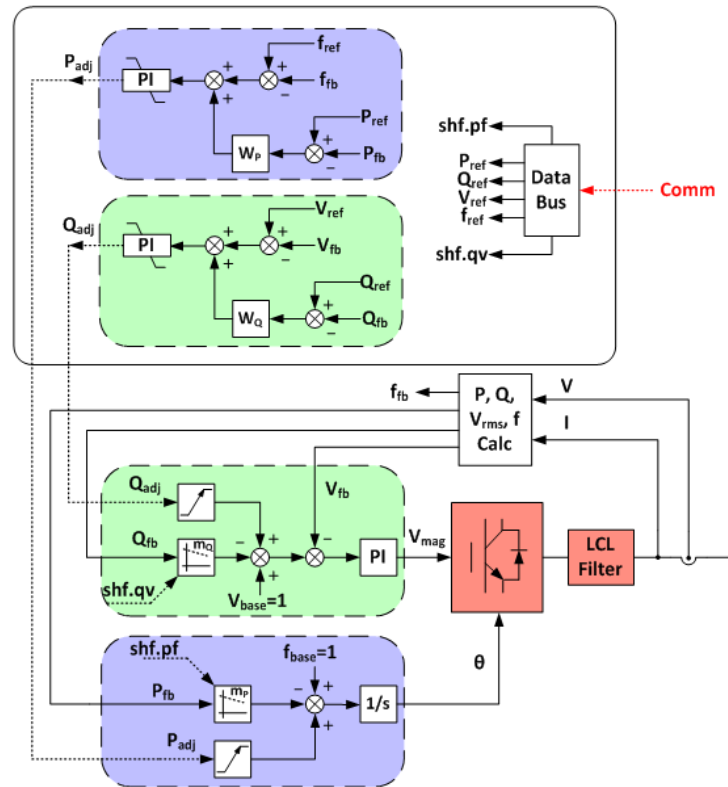


Figure 4.39: The block diagram of the controls for voltage and frequency of storage inverter.

Figure 4.39 shows the block diagram of the energy storage inverter control proposed and applied in this study. The active and reactive power delivered are adjusted

by regulating the output voltage magnitude and angle relative to microgrid bus voltage. The controller can adjust the output voltage (and consequently active and reactive power) according to measured voltage and frequency as well as commands from a supervisory controller.

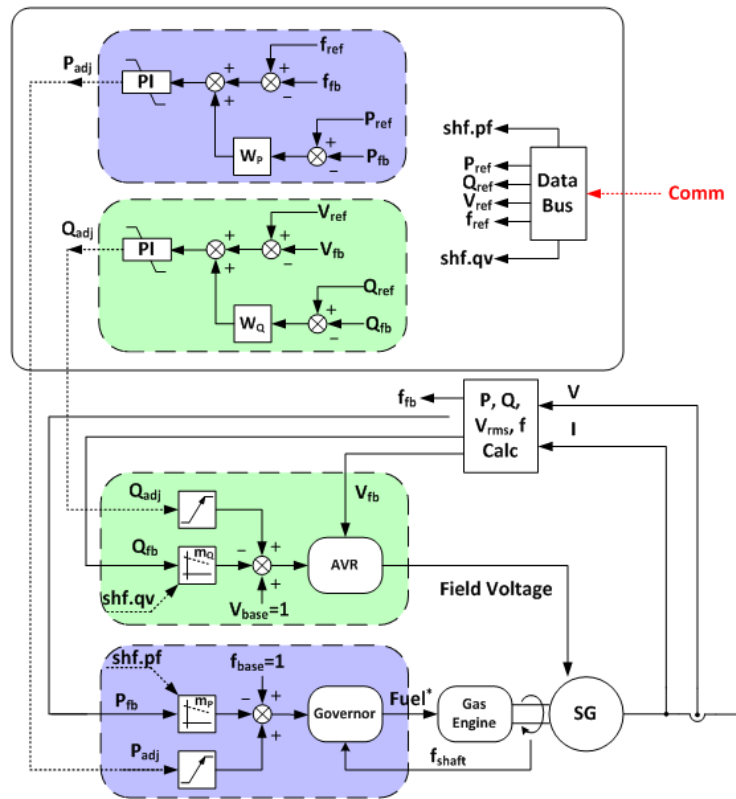


Figure 4.40: The block diagram of frequency and voltage controls for natural gas generator.

Figure 4.40 shows the voltage and frequency control diagram of natural gas generator. Similarly, the terminal voltage and frequency can be adjusted by the given voltage and frequency bias according to droop control as well as commands from a supervisory controller.

A. Intentional Islanding

Intentional islanding, which provides the capability for the microgrid to manually separate from the bulk grid, leads to potential issues of power balancing, voltage sag, and frequency oscillation [37]. To prevent the large transient that follows the loss of the bulk grid, the DGs within microgrid must be preplanned to switch their controls and share the local loads to minimize the impact of disconnection from the host utility.

In this paper, we apply a technique to achieve minimal transient condition to perform intentional islanding. The proposed algorithm adjusts the active and reactive power at point of grid connection to zero before the static switch is opened. Figure 4.41 illustrates the algorithm and procedure to minimize the transients. Power sharing algorithm is applied to support the loads and voltage through microgrid DG and energy storage. Before islanding is applied, the power and voltage calculations of the microgrid determines if there is need for natural gas generators to turn on, synchronize, and provide support. Due to very high penetration of renewable energy sources in this configuration, there are several cases where the load within microgrid is smaller than the power available from renewables and energy storage devices. However, due to the large impedance distribution lines and improper placement of DGs, the voltage at various buses may be violated if active and reactive power from natural gas generator are not available [38].

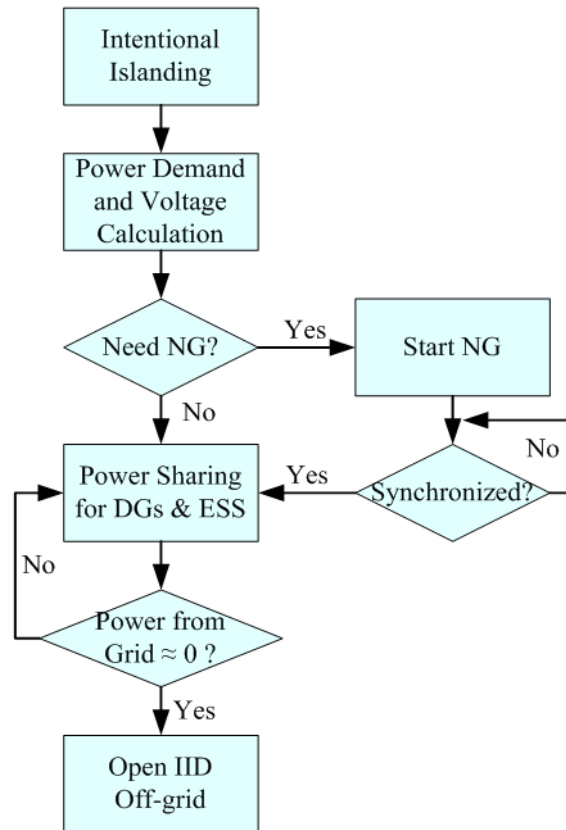


Figure 4.41: The general algorithm for microgrid intentional islanding.

Case 1: Peak Load without Renewable Energies

In this case, the maximum loading and zero power injection from renewable energies are selected as conditions for the study. The objective is to verify (i) the microgrid is able to be self-sustaining without renewable energies during intentional islanding and island mode; (ii) transients due to change in controls functions are acceptable; and (iii) system voltages and frequency are within the acceptable range during transition according to IEEE standard 1547.

Figure 4.42 shows the real and reactive power delivered by grid, natural gas generation and battery. The microgrid is intentionally islanded at 5 second. During time interval 2, natural gas generator starts up and synchronize to the microgrid, while the battery provide maximum output power to minimize the transition time. Once the natural gas generator is connected to the microgrid, it increases its output power according to the commands sent by Supervisory Control Unit (SCU) until the real and reactive power delivered by the grid reach nearly zero (in the simulation a power bandwidth of 1kW and 1kVar is set for opening static switch). There are some manageable transients as shown in time interval 3 due to change is system architecture.

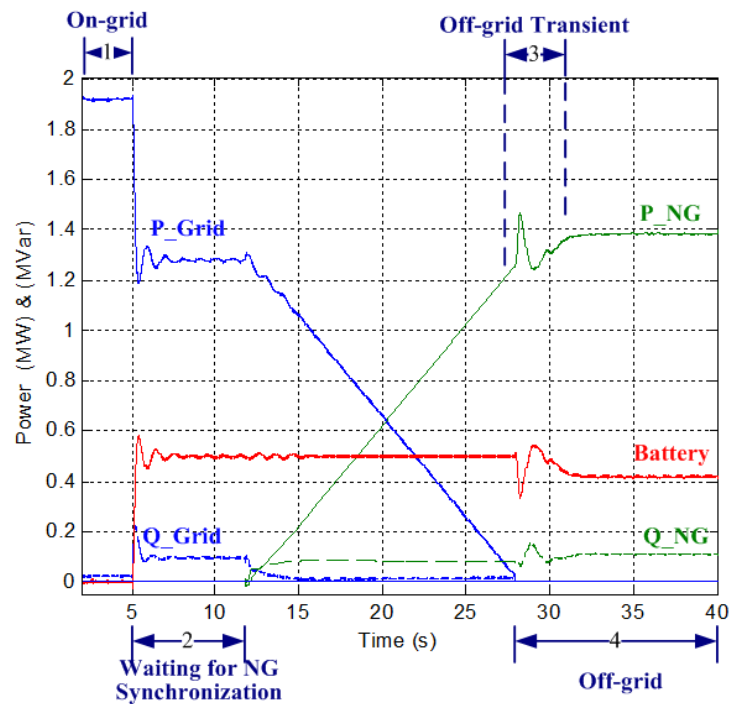


Figure 4.42: Real and reactive power delivered by grid, natural gas generator and battery during intentional islanding for case 1.

During intentional islanding, the SCU commands determines the output power of natural gas generator and energy storage using control block diagrams of Figures 4.39 and 4.40. In island mode, the voltage and frequency droop control of the same algorithm takes over the power control [38]. Using the identical control algorithm minimizes the transients introduced by the transition. The frequency in island mode drops from 60Hz (on-grid and off-grid transition) to 59.08Hz (off-grid) according to the frequency droop settings (peak load and no renewables) as shown in Figure 4.43. The voltages at load and renewable source terminals are improved in island mode compared with grid-tie mode due to the power provide by the storage element.

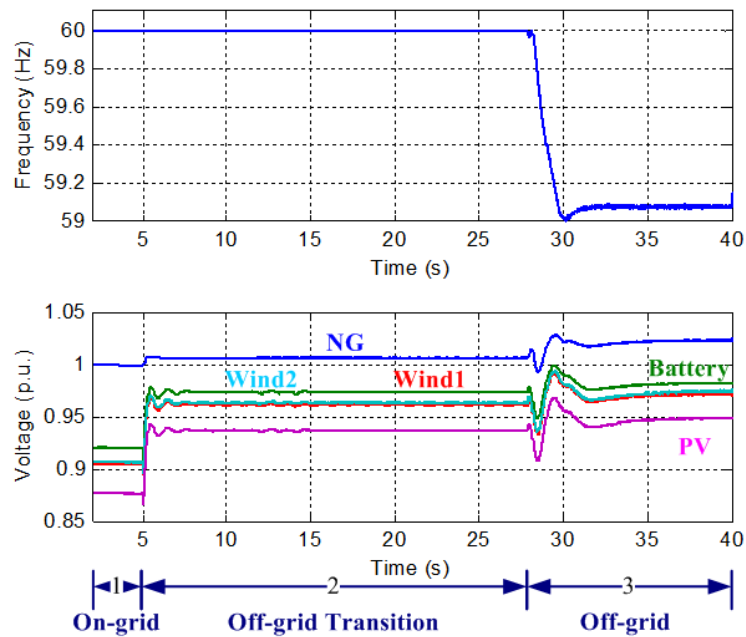


Figure 4.43: Profiles of voltage at source buses and frequency during intentional islanding for case 1.

Case 2: Minimum Load with 100% Renewable Energies

A totally different condition compared with case 1 is also studied to verify: (i) the microgrid is able to manage power and regulate the voltage within the safe range when renewable generation exceeds demand; (ii) power curtailment mechanism for renewable energies [38] works during intentional islanding, and (iii) the transients of voltages and frequency are acceptable during transition referring to IEEE standard 1547.

Figure 4.44 shows the real and reactive power delivered by grid, natural gas generator, battery, wind turbine 1, wind turbine 2, and solar PV. Notice that the nominal capacity for wind turbine 1 and 2 are 750kW. However, since their terminal voltages exceed the maximum threshold, their output powers are curtailed to limit the voltage.

In contrast with case 1, the system frequency increases from 60Hz (on-grid and off-grid transition) to 60.52Hz (off-grid) as shown in Figure 4.45. The voltages at renewable buses are above 1 p.u. but within the acceptable range. The voltages of battery and natural gas generator decrease according to the voltage droop control (they are supplying more reactive power to the system compared with case 1).

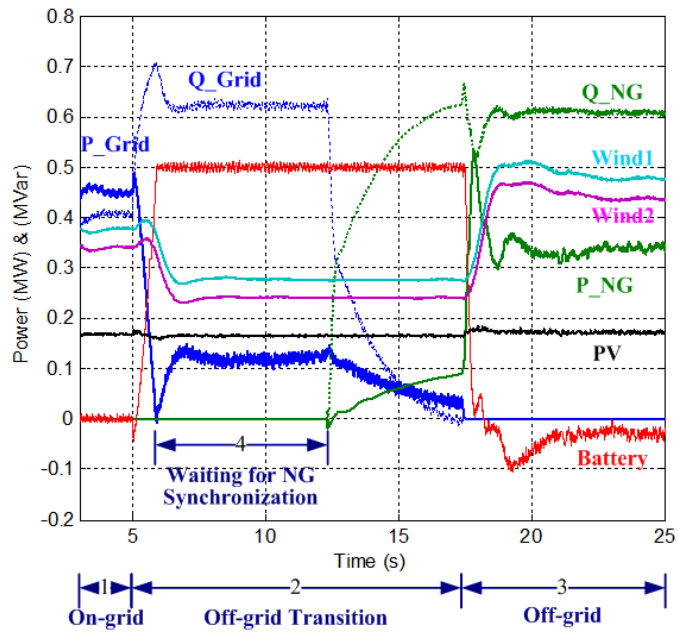


Figure 4.44: Real and reactive power delivered by the grid and five sources during intentional islanding for case 2.

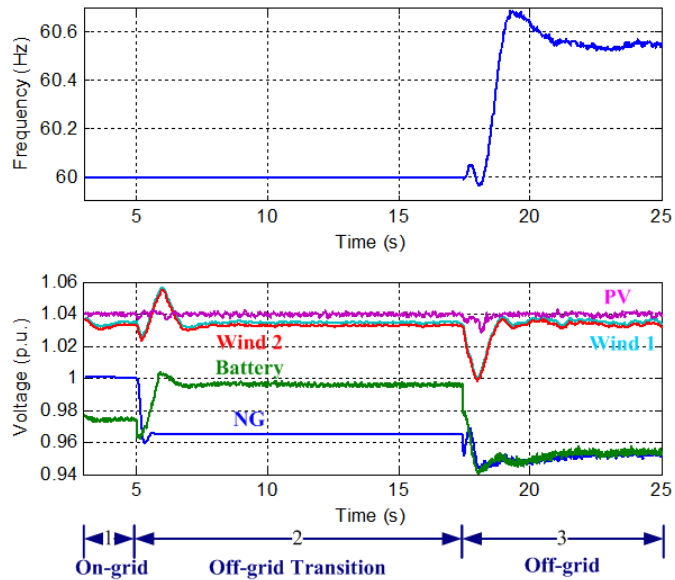


Figure 4.45: Profiles of voltage at source buses and frequency during intentional islanding for case 2.

B. Unintentional Islanding

When the main grid is lost or the static switch at the Point of Common Coupling (PCC) opens to prevent DGs from the faults at main grid, the unintentional islanding occurs, and the microgrid is exposed to voltage and frequency variations. To prevent large voltage and frequency transients during unintentional islanding, the microgrid needs to be configured so that the mismatched power can be immediately compensated by the dispatchable power sources, which requires them to operate in voltage control mode. Since the natural gas generation is off-line during grid-connected mode and the renewable sources are non-dispatchable, the energy storage system becomes the only power source to adjust the power flow during unintentional islanding and manage the voltage along with reactive power from renewable sources. Therefore the energy storage system is sized to be able to support the critical loads so that the critical loads are supplied in any extreme cases.

In the system studied here, there are a maximum total of 0.42 MW critical and 1MW non-essential loads. During unintentional islanding, all of the non-critical loads are shed regardless of the output power from renewable energies, until the natural gas generator is synchronized. Energy storage supports system voltage and frequency, waits for the synchronization of natural gas generator, and then shares power according to the pre-defined droop curves. Its charging or discharging procedure depends on the power delivered by renewable energies as well as its state of charge. To test

the unintentional islanding and load shedding, similar to intentional islanding, two extreme cases are studied.

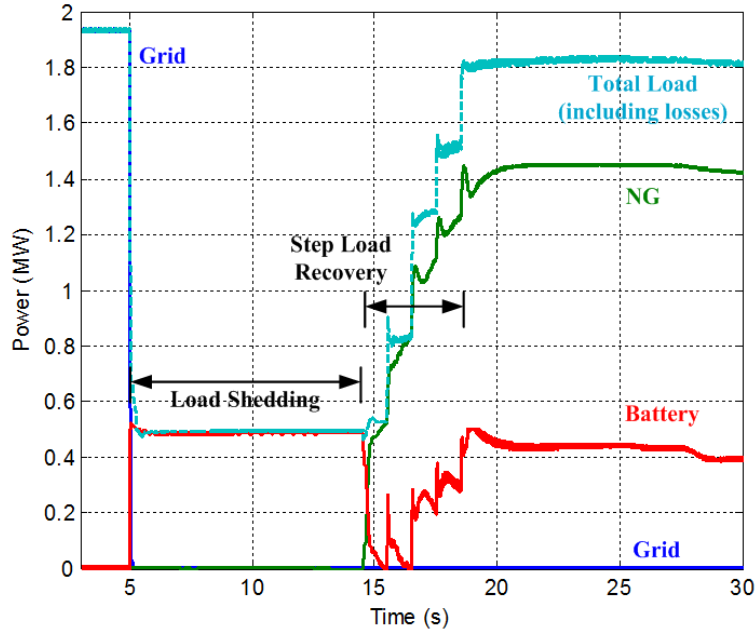


Figure 4.46: Unintentional islanding: total load (including losses) and real power delivered by grid, natural gas generator and battery for case 1.

Case 1: Peak Load without Renewable Energies

Figure 4.46 shows the total load (including losses) and real power delivered by grid, natural gas generator and battery. The transition of unintentional islanding is divided into two parts: load shedding and load recovery. When the islanding occurs, all the non-critical loads are shed at second 5. The storage supports the critical loads. Natural gas generator is synchronized before second 15. Then the non-critical loads are reconnected in steps and are picked up by storage and generator according

to the droop control. Figure 4.47 shows the system frequency and source voltages. Frequency has a 1.5Hz dip at 5 second because of a short period of power loss. On the contrary, the source voltages rise at the same moment due to excessive reactive power delivered by renewable sources. Referring to paper [38], renewable energies are providing or absorbing reactive power according to their terminal voltages. In this case, before islanding (5 second), they are providing reactive power to support the voltages. But when main grid disappears and the load shedding occurs, the reactive power demand drops suddenly and dramatically. The excessive reactive power lifts the system voltage and in result generations including renewable energies react to cease reactive power to regulate the voltage within the required range.

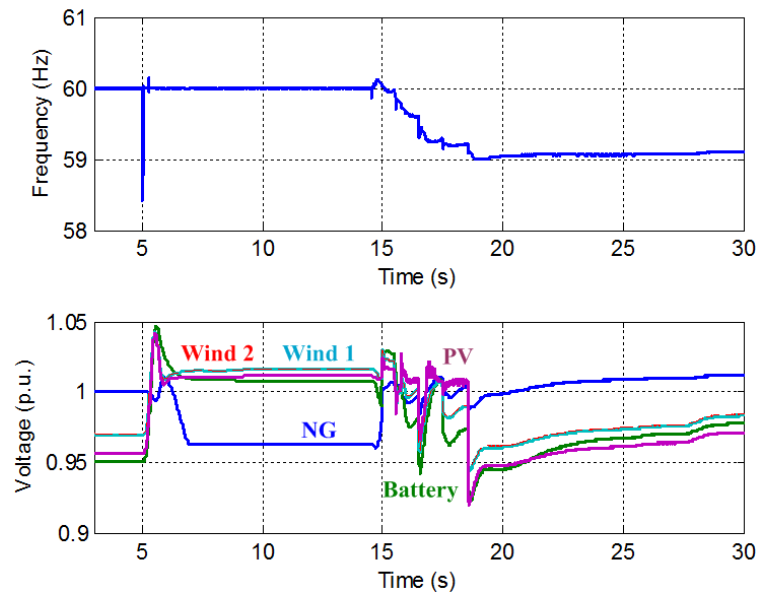


Figure 4.47: Profiles of voltage at source buses and frequency during unintentional islanding for case 1.

Case 2: Minimum Load with 100% Renewable Energies

Figure 4.48 shows the waveforms of the total load including losses and the real power delivered by grid, natural gas generator, battery, wind turbine 1, wind turbine 2 and solar PV. The frequency and voltage profiles are shown in Figure 4.49. Compared with case 1, the frequency at second 5 is increased slightly since the load shedding leads to excessive real power flowing in the system, which increases the frequency and terminal voltages of renewable sources.

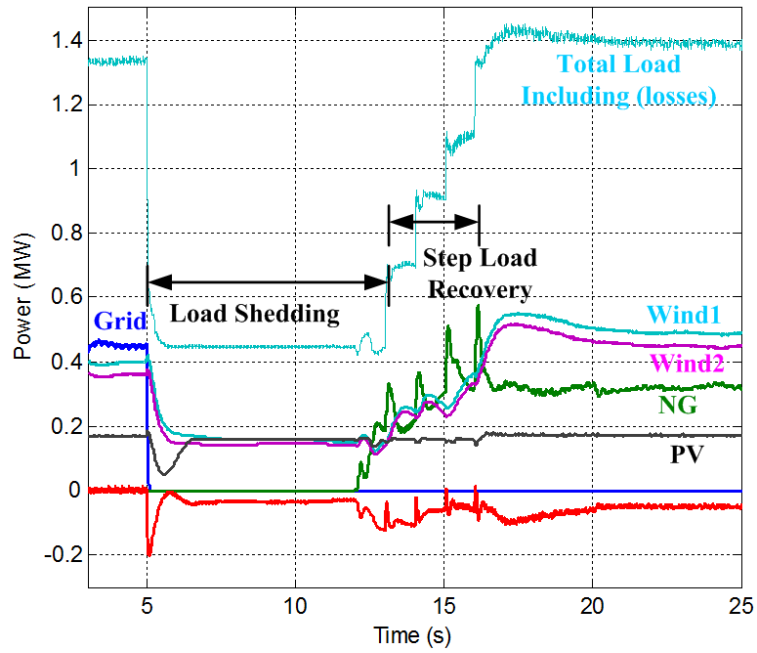


Figure 4.48: Unintentional islanding: total load (including losses) and real power delivered by grid and five sources for case 2.

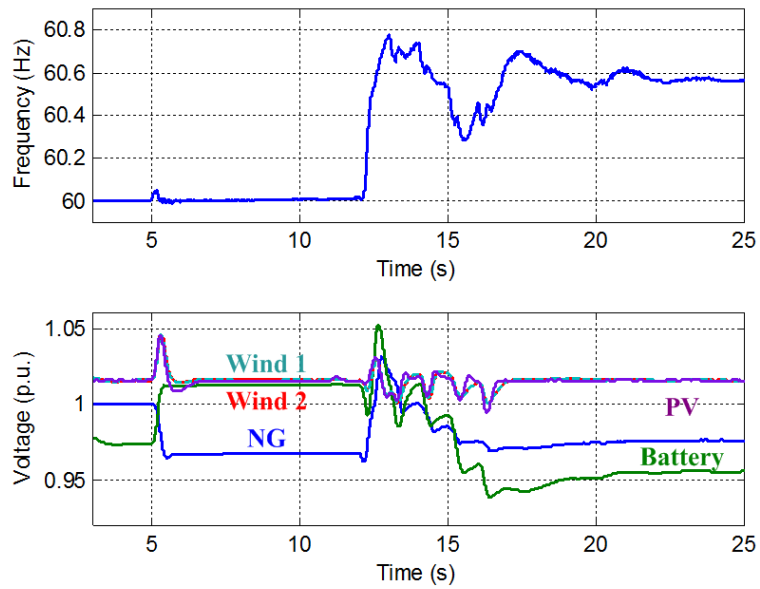


Figure 4.49: Profiles of voltage at source buses and frequency during unintentional islanding for case 2.

4.4.4 Microgrid Reconnection

Before connecting two energized AC power systems, the frequencies and voltages at both side of the point of common coupling must be the same to minimize the transients and avoid disturbance. Since a microgrid consists of more than one generation, adjusting system frequency and voltage becomes challenging.

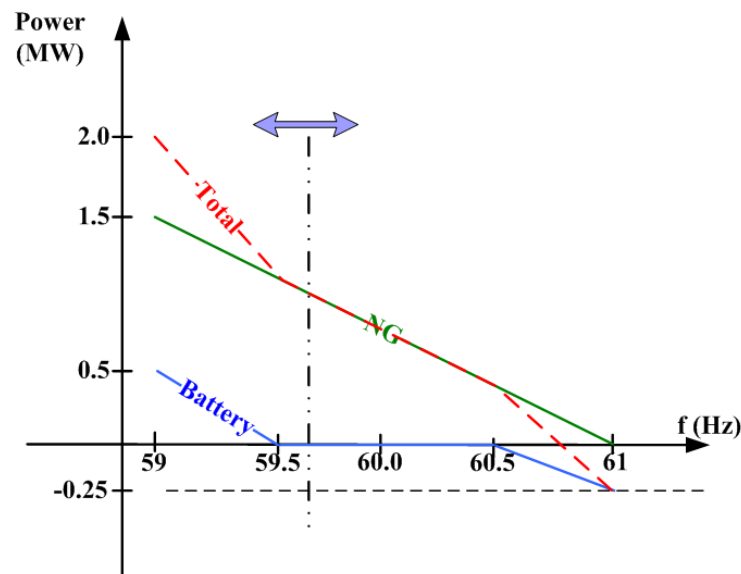


Figure 4.50: The shifting droop control diagram for active power and frequency during reconnection.

In this paper, a shifting droop control method is proposed to match the voltage and frequency of the microgrid with grid before reconnection. The diagram of the proposed method is shown in Figure 4.50. The idea is to shift the preset droop curves to change the operating frequency and voltage without changing the active/reactive power sharing between sources. By shifting the droop curves on frequency axis,

the power demands set points for the sources remain the same due to the same loading condition, while the actual frequency changes to a new value determined by the shifting offset value. The shift in voltage and frequency setting is applied using shf.pf and shf.qv. inputs in Figures 4.39 and 4.40. Each source still operates individually based on the droop control and the offset is provided by the SCU. One of the advantages of this method is that even in case of lost communications between SCU and sources during reconnection, the microgrid is still able to operate normally in island mode.

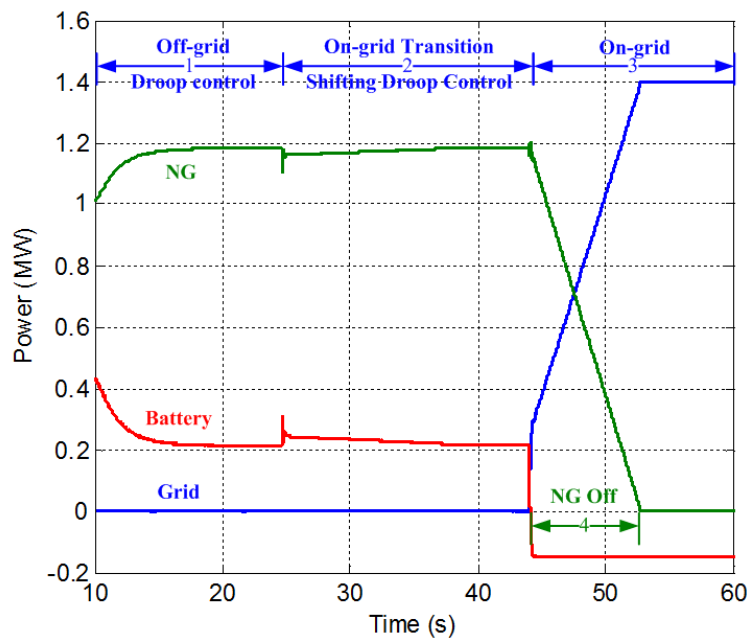


Figure 4.51: Waveforms of power delivered by grid, natural gas generator and battery during reconnection.

This shifting droop control algorithm has been tested and demonstrated in the

proposed microgrid. According to the droop control, natural gas generator and battery share the total load which is the summation of all 53 loads plus losses minus renewable energy generations. In order to analyze the performance of the proposed method, a total constant 1.4MW equivalent load is considered, with 1.2 MW loads, 0.2 MW losses, and zero renewable energy. The reasons for ignoring the renewable sources and choosing constant load in this test case are: (i) renewables are regarded as negative load since they are operating in current mode and (ii) any load variations which create frequency variations prolongs the reconnection process. When the phase angles at both side of PCC match, the synchronizer sends command to close the breaker. The frequency change affects the phase angle and makes it more difficult to equalize the phase angle at both sides.

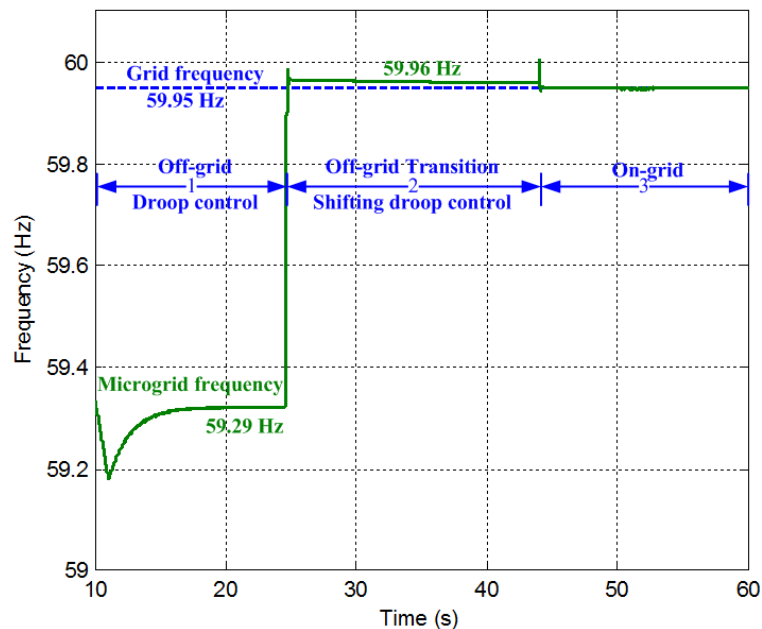


Figure 4.52: Frequencies of the main grid and microgrid during reconnection.

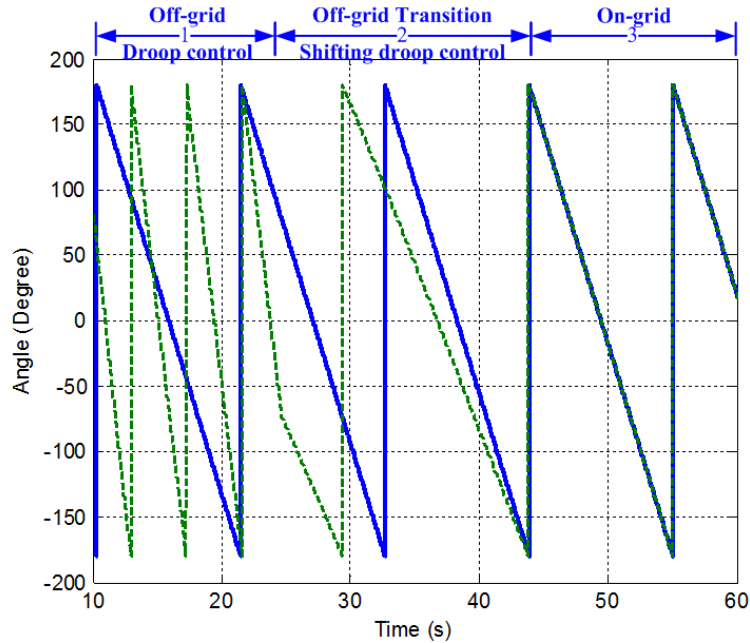


Figure 4.53: Instantaneous angle (Phase A) of the main grid and microgrid during reconnection.

Figure 4.51 shows the waveforms of the power delivered by grid, battery and natural gas generator. Three stages are marked in the figure: off-grid, on-grid transition (reconnection), and on-grid. The transients in between three stages are smooth and power sharing between natural gas generator and battery are kept almost the same. The natural gas generator power is ramped to zero when reconnection happens and the load is picked up by the main grid. Figure 4.52 shows the main grid and microgrid frequency profiles. The frequency set point for microgrid in off-grid mode is 59.3Hz which can be determined by the droop curves. The grid frequency is set to 59.95Hz in order to show the grid voltage phase A angle in a saw waveform. (In PSCAD, voltage angle is always referred to 60Hz and initial phase of zero). Around 25 second,

a big jump occurs from 59.29Hz to 59.96Hz according to shifting droop technique. The microgrid frequency is set at 0.01Hz above the grid frequency to adjust the phase angle. The waveforms of phase angles are shown in Figure 4.53.

4.4.5 Microgrid Black Start

A simple black start mechanism for the proposed microgrid is studied and tested in this paper. Energy storage, critical loads, non-renewable sources, non-critical loads, and renewable are started and connected to the system one by one. Specifically, in the proposed microgrid, initially the energy storage system is turned on to energize the transmission lines and transformers. All customers (loads) are disconnected. After a short period, the critical loads are connected and powered. At the same time, the natural gas generator starts up and begins synchronizing with the system. Once the natural gas generator is synchronized and connected to the system, the non-critical loads are powered step by step. At the end, the renewable energies are allowed to start and provide power. Figure 4.54 shows the total load and power from battery and natural gas generator. Figure 4.55 shows the waveforms of voltage and frequency at PCC.

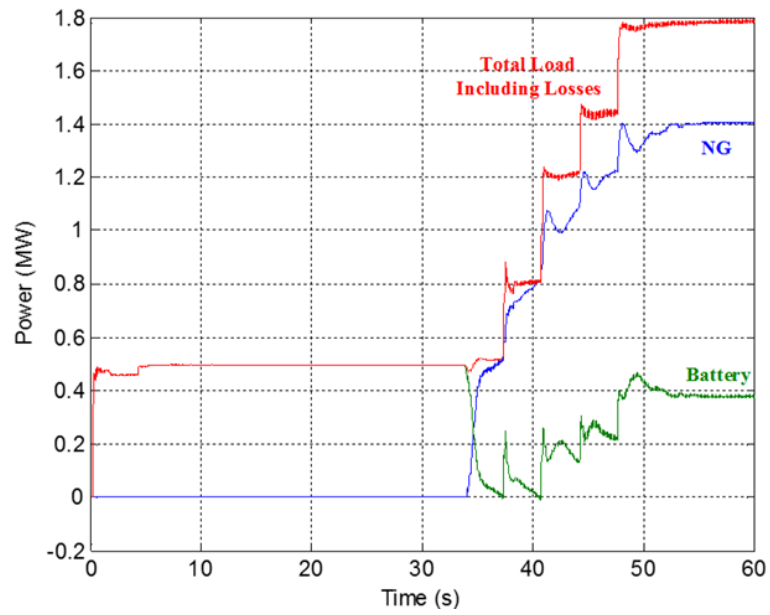


Figure 4.54: Real power of total load, battery and natural gas generator.

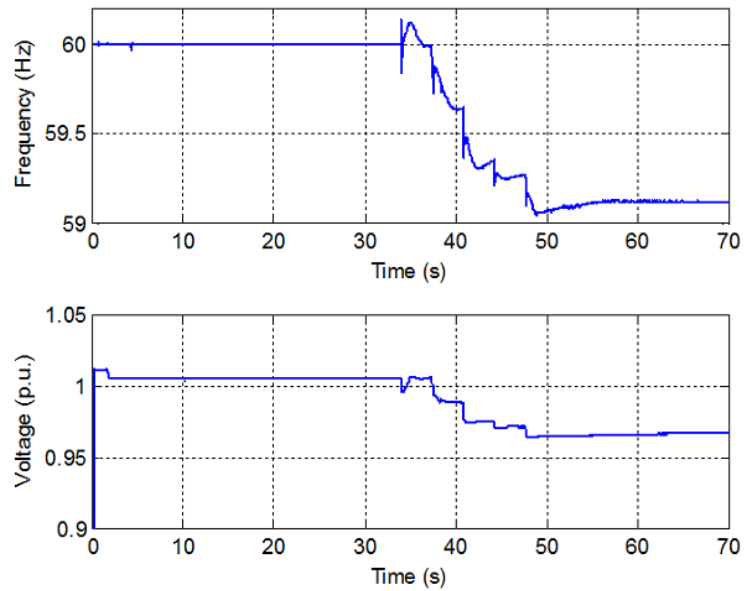


Figure 4.55: Waveforms of voltage and frequency at PCC.

Chapter 5

Power Quality and Reliability Assessment

By integrating a large amount of renewable energy to the power system, the intermittency of injected power from renewable energy raises concerns of instability and uncertainty in the power network. According to the specific microgrid studied in the project, where the penetration of renewable energy reaches 100%, it is necessary to assess the microgrid reliability and power quality, so that the performance of the microgrid is evaluated and the follow-up improvement studies are able to be started and compared.

In this chapter, the common used power quality indexes in utility companies are calculated for the proposed microgrid with controls and managements stated in previous chapters. The indexes are compared in different cases. Moreover, a probabilistic analysis for microgrid reliability is also introduced and developed to evaluate the voltage stability.

5.1 Power Quality Definition

Reliability assessment is very important in the design, planning and operation of electric power system, especially for distribution system. The performance of distribution systems are typically quantified by the following issues: evaluation of losses, power factor, overhead vs. underground designs [39–41]; counts of anomalous events [42–46]; and power quality at the point of end use [47, 48]. Reliability assessment is usually using the component reliability data obtained and observed from real system for the past monthly or yearly period, and applying them to the mathematic model of the evaluated system to predict and evaluate the reliability performance in future. By calculating and estimating the probability of a component or system to operate as expected or not to operate as expected, a reliability assessment tool is able to present and state the reliable level. Those of the common used indexes by utility companies, which represent the reliability level, are namely System Average Interruption Duration Index (SAIDI), System Average Interruption Frequency Index (SAIFI), and Customer Average Interruption Duration Index (CAIDI).

SAIDI is the average outage duration for each customer served. SAIDI is measured in units of time, often minutes. It is usually measured over the course of a year.

$$SAIDI = \frac{\textit{Total duration of customer interruptions}}{\textit{Total number of customers served}} \quad (5.1.1)$$

SAIFI is the average number of interruptions that a customer would experience. SAIFI is measured in units of interruptions per customer. It is also typically measured

over the course of a year.

$$SAIFI = \frac{\text{Total number of customer interruptions}}{\text{Total number of customers served}} \quad (5.1.2)$$

CAIDI is the Customer Average Interruption Duration Index and is described as:

$$CAIDI = \frac{\text{Total duration of customer interruptions}}{\text{Total number of customer interruptions}} = \frac{SAIDI}{SAIFI} \quad (5.1.3)$$

In North American distribution system, the typical ranges for these indexes are:

$$SAIDI = 1.5 \text{ to } 3.0 \text{ hours}$$

$$SAIFI = 1.1 \text{ to } 1.9 \quad (5.1.4)$$

$$CAIDI = 0.9 \text{ to } 2.6 \text{ hours}$$

5.2 Power Quality Assessment

The microgrid in the study has 53 loads and five generations. As described in Chapter 3 and 4, controls have been implemented for renewable sources and energy storage inverters to control the voltage in the system and increase the energy delivery of these sources. In the island mode, the natural gas generator and energy storage system regulate the system frequency and stabilize the voltage profiles according to the changes of the load. The renewable energies perform as negative loads providing active power transformed from natural resources. They also provide reactive power to help regulate their terminal voltage within acceptable range.

To evaluate power quality of proposed microgrid, several assumptions have been made. First, the microgrid system is tested only in the island mode, the grid-connected mode and transitions between them are not considered. Second, it's impossible to import data of a whole year and run the simulation for the course of a year, instead, a 24-hour real time load and generation data are used. The daily simulation results will be regarded as a typical daily profile and extended to a year. At last, no fault situation is considered when assessing power quality indexes.

As we know, the power system performance, which is mainly evaluated by voltage profiles, is varying from the configuration of the system. Particularly in the proposed microgrid, the locations of transformers (regulators) and energy storage system play an important role of regulating the overall bus voltages in the microgrid, and in result the power quality indexes are influenced. Therefore, to show the influence of system configuration, three cases are considered.

- 1) Case-1 without regulator between buses 832 and 852 and with storage element at bus 828
- 2) Case-2 with regulator and energy storage at bus 832
- 3) Case-3 without regulator and storage at bus 832

It is worthy to mention that, the locations for renewable energies are selected and are not supposed to be moved because they are typically installed at far end of the distribution system where people call them weak buses. Bus 848, 840 and 890 are

computed to be the weak buses to install wind turbine and solar PV. Moreover, by considering the flexibility of microgrid operation, that is to make the microgrid easy to connect to or disconnect from the bulk grid, natural gas generator is agreed to be installed at bus 800.

Voltage monitoring unites have been implemented on each bus to analyze the voltage profiles. Table 5.1 shows the power quality parameters for these three cases. A load is considered to be interrupted when its terminal voltage falls under 0.88 p.u. It also should be noted that these values only reflect the power quality when all the components of the system function normally. No scheduled or unscheduled component maintenance is considered. In addition, the results are only for a single wind and solar PV power profile. Other profiles may yield different results.

Table 5.1: Power quality parameters for three cases

	Case 1	Case 2	Case 3
SAIDI (hrs)	3.25	0.91	0
SAIFI	166	796	0
CAIDI (hrs)	0.0196	0.0011	0

In case 1, each customer has an average of 3.25 hours outage during a year with 166 times of interruption. Each interruption may last for 70.56 seconds (0.0196 hours). In case 2, each customer has less outage duration which is 0.91 hours during a year, however, with more interruptions which is 796 times of interruption. Each interruption lasts for 3.96 seconds (0.0011 hours). Case 3 is the best case, where there is no power outage during a year.

From the results, obviously, bus 832 is better than bus 828 to place the energy storage devices. Because geographically, bus 832 is much closer to renewable energies which provide large power intermittency to the system, and need to be smoothed by energy storage system. Moreover, in the original system, a regulator is placed between bus 852 and bus 832 to raise the voltage of the downstream of the system. However, in the modified system, since the renewable energies may provide sufficient power, the power flow in the line between bus 852 and bus 832 is not unidirectional anymore. The extra power will be transferred to upstream buses. Therefore the regulator is not necessary and even causes the voltage instability as the tap changer reacts very slow (0.25s).

This power quality assessment not only provides a way to evaluate the surety of the power system at customer end, it also enables a new approach to plan and improve the configuration of the system. One can follow the step below to approximately do a yearly power quality assessment: i) Various typical daily data for different season, temperature and other weather condition can be created, by analyzing a yearly load and generation profiles; ii) Calculate the weights for different selected daily data; iii) Apply each daily data to the simulation model of the power system, and calculate the power quality indexes. iv) Multiply the power quality indexes of different days with their weights, and sum them up.

5.3 Probabilistic Load Flow for Microgrid Reliability Assessment

Probabilistic load flow (PLF) is regarded as an effective analytical tool to plan and evaluate a power system, especially for a system with high penetration of renewable energies. Different from deterministic analyses, PLF opens a gate to look into the expected reliability of the power system by taking consideration of the uncertainty of natural resources. In the paper, two types of probabilistic analyses are presented in the following sections.

5.3.1 Data Based PLF Assessment

For an existed power system, where the load and generation data are available to use, we can mathematically model the system and evaluate the reliability straightforward by importing the real data. According to the proposed microgrid, which is modified from IEEE 34 bus system, our purpose is to convert the original system to be a microgrid by adding distributed generations and controls. Assuming that all the load, wind, and PV data are measured and recorded for the proposed system. When they are applied to the time series load flow, the bus voltages and branch power flows reflect not only deterministic performance of the system by looking at the time series values, but also probabilistic performance of the system by looking at the histogram

of the results.

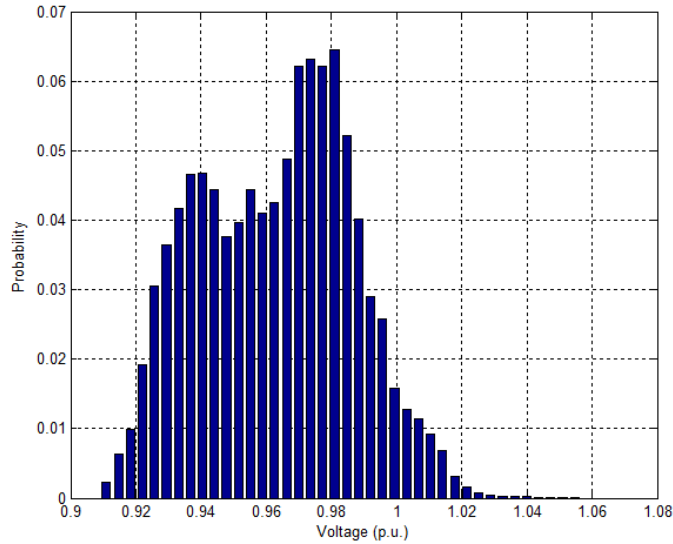


Figure 5.1: Histogram of voltage at bus 822.

The same three cases discussed above will be analyzed and compared in this section. First, let us consider the original case - Case 1. The simulation results of the microgrid in island mode has been shown in Chapter 4. Figure 4.25 shows the voltage profile at bus 822 for 24 hours time period. In another manner, If we draw the histogram of the selected bus voltage, it gives out a probability distribution of voltage in per unit shown in Figure 5.1. The corresponding cumulative distribution is shown in Figure 5.2. By this manner, we are able to calculate the probability when a selected bus voltage is lower than or higher than a specific value, so that a probabilistic assessment can be conducted. For instance, in this case, the probability when voltage at bus 822 is lower than 0.92 p.u. is computed to be 1.79%.

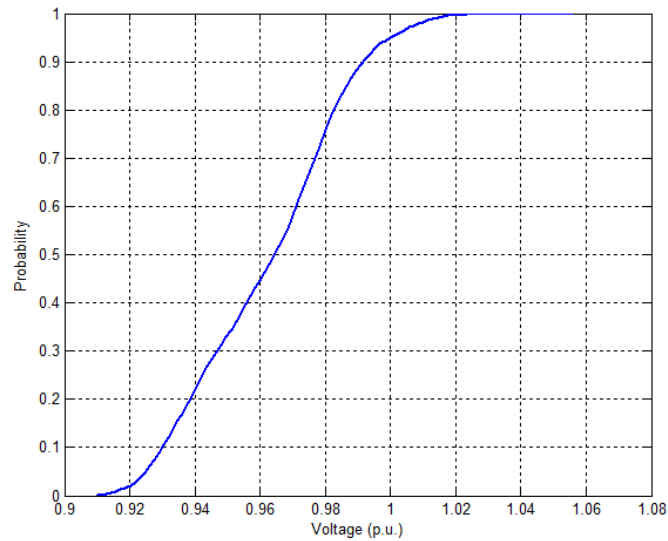


Figure 5.2: The cumulative distribution of voltage at bus 822.

In the study, the voltage magnitude is classified into four types: damageable low voltage, low voltage, normal voltage, and damageable high voltage. The probabilities of selected bus voltages in different classes are shown in table 5.2. From the table, we can easily find out which bus has high or low voltage issue, and which bus has a better power quality. For instance, Bus 890 (Solar PV generation) encounters low voltage problem more than other buses. Either a capacitor bank or a energy storage device is suggested to install nearby this bus to help improve the voltage. Bus 800 has a damageable high voltage issue. However, by looking at the system configuration, we know there is a Natural Gas generator installed at Bus 800, and it needs to adjust voltage higher than 1.05 pu to ensure other bus voltages in the heavy load condition. One may also conclude that bus 854 and bus 824 have a better power quality, because

over 99% their voltage are within normal range.

Table 5.2: Summary of classified probabilities of selected bus voltages in case 1

	Damageable Low Voltage (≤ 0.92)	Low Voltage ($0.92, 0.96]$)	Normal Voltage ($0.96, 1.05$)	Damageable High Voltage (≥ 1.05)
Bus 800	0	0	81.46%	18.54%
Bus 814	0	29.87%	68.85%	1.28%
Bus 818	0	12.99%	86.91%	0.1%
Bus 822	1.79%	42.14%	56.06%	0.01%
Bus 824	0	0	99.97%	0.03%
Bus 832	0.52%	14.78%	84.70%	0
Bus 840	2.25%	13.14%	84.61%	0
Bus 848	3.08%	12.56%	84.36%	0
Bus 854	0	1.5%	99.85%	0
Bus 890	10.33%	16.02%	73.65%	0

The similar analysis is conducted for case 2 and case 3 with the results shown in Table 5.3 and 5.4. Comparing case 2 with case 1, the low voltage problem for the downstream buses are improved dramatically, because a regulator has been installed between bus 832 and bus 854, moreover, the battery has been moved from bus 828 to bus 832 that the battery has more controllability to downstream buses. However, the upstream buses which is far from generations such as bus 818 and bus 822 encounter low voltage issues.

In case 3, the regulator is removed in order to improve the upstream voltage profiles. Although it may lower downstream voltage magnitudes, there are renewable energies and batteries which are capable of regulating downstream bus voltages. From the results, there is tiny chance of damageable low voltage issue occurs at bus 822 and bus 890, but overall, the system is operating within a reliable environment.

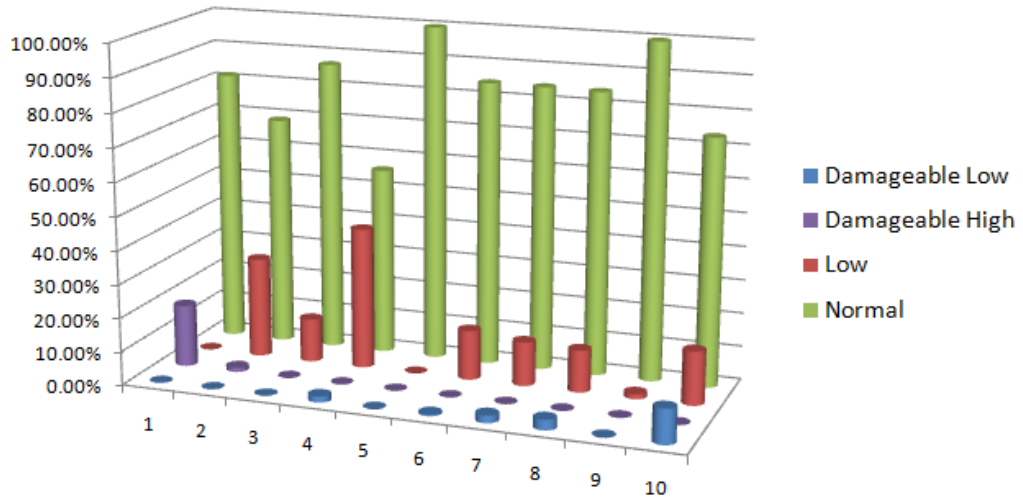
Table 5.3: Summary of classified probabilities of selected bus voltages in case 2

	Damageable Low Voltage (≤ 0.92)	Low Voltage (0.92,0.96]	Normal Voltage (0.96,1.05)	Damageable High Voltage (≥ 1.05)
Bus 800	0	0	96.90%	3.10%
Bus 814	2.50%	88.07%	9.24%	0.19%
Bus 818	5.46%	66.96%	27.58%	0
Bus 822	50.21%	42.99%	6.79%	0
Bus 824	0	0	100%	0
Bus 832	0	0	99.57%	0.43%
Bus 840	0	0	99.67%	0.33%
Bus 848	0	0	99.81%	0.19%
Bus 854	0	0.21%	99.79%	0
Bus 890	0	0.37%	99.63%	0

To intuitively show and compare the results, figure 5.3 - 5.5 depict the column charts of each case. Obviously, green column in case 3, representing normal operation, is overall higher than other two cases, while blue and purple columns (damageable low and high voltage) are lower.

Table 5.4: Summary of classified probabilities of selected bus voltages in case 3

	Damageable Low Voltage (≤ 0.92)	Low Voltage (0.92,0.96]	Normal Voltage (0.96,1.05)	Damageable High Voltage (≥ 1.05)
Bus 800	0	0	84.19%	15.81%
Bus 814	0	36.13%	63.87%	0
Bus 818	0	14.44%	85.56%	0
Bus 822	1.93%	41.16%	56.91%	0
Bus 824	0	0	100%	0
Bus 832	0	0.21%	99.79%	0
Bus 840	0	0.36%	99.64%	0
Bus 848	0	0.38%	99.62%	0
Bus 854	0	0	100%	0
Bus 890	0.13%	13.53%	86.34%	0



1	2	3	4	5	6	7	8	9	10
Bus 800	Bus 814	Bus 818	Bus 822	Bus 824	Bus 832	Bus 840	Bus 848	Bus 854	Bus 890

Figure 5.3: Column chart of case 1.

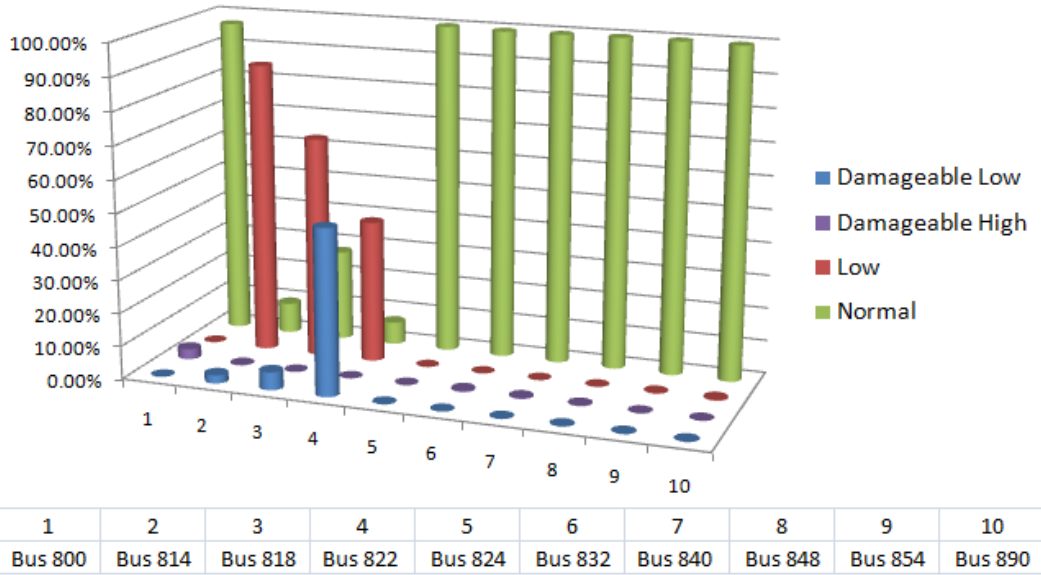


Figure 5.4: Column chart of case 2.

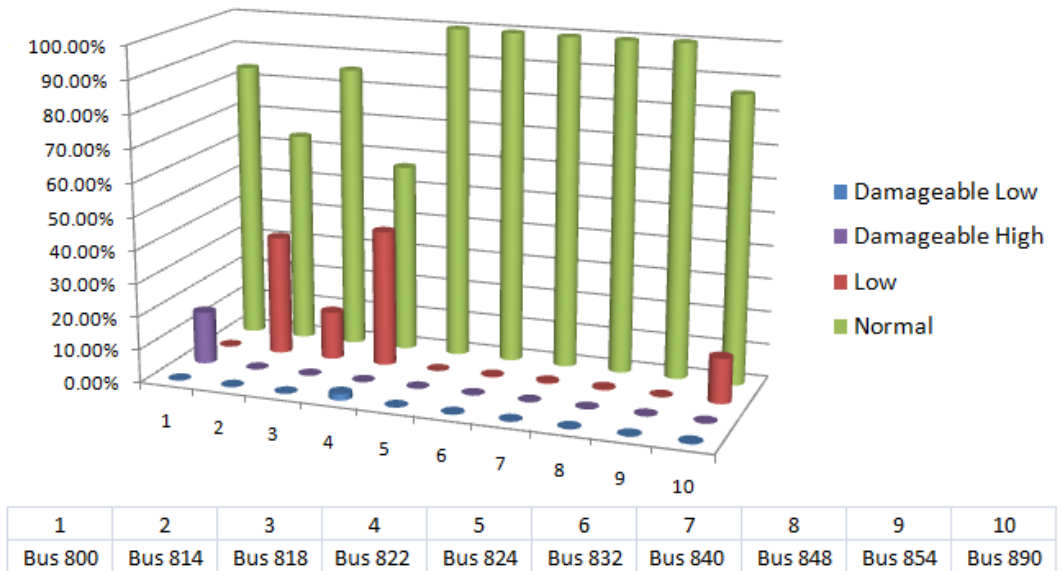


Figure 5.5: Column chart of case 3.

5.3.2 Model Based PLF Assessment

In this section, a model based PLF assessment tool is presented. As we know, in most cases when utility company plans for a power network, such as the placement of reactive power compensators, generations, and transformers etc., the time series load data for a long time period is impossible to have. In order to ensure the reliability of the power system, a nominal load or peak load condition is always regarded as a worst case to conduct the planning analysis. For example, a traditional VAR compensation optimization is always conducted under the worst case. However with the increasing of renewable energy penetration in power system, the planning analysis faces a new challenge that is the renewable energy is non-dispatchable and brings large power intermittency into the power system. This section offers a novel model based PLF algorithm to reflect a more accurate probabilistic nature of load flow with consideration of wind and solar powers. It can help system operators understand the load flow distribution and do the long term planning based on the results.

So far, various techniques for model based PLF analysis have been studied in the literatures. A new probabilistic load flow algorithm to account for input data uncertainties in the load flow calculation is proposed in [49]. The paper assumed the uncertainty of the line parameters and bus injections can be estimated or measured and showed how to estimate the true distributions of the solution of a load flow problem for networks with constant configuration. In [50], Borkowska studied

the network as a DC equivalent model, and accounted for nodal data uncertainty to find the distributions of branch flows. [51] proposed a method for probabilistic load flow in networks based on the properties of the cumulants of the probabilistic density functions (PDF) and the Cornish-Fisher expansion. The author compared the results to those obtained by using Gram Charlier expansion, and demonstrated that the Cornish-Fisher expansion is more suitable for non-Gaussian distribution. [52] presented a probabilistic model of wind farm generation that combines the wind turbine and induction wind generator models. In the model, the real power injected and reactive power absorbed by the wind turbine were described as the function of the voltage magnitude, the slip of the induction machine and circuit parameters of the wind turbines. Then the PLF equations can be solved by performing a unified iteration for original state variables and the slip. Another PLF method based on the point estimation is proposed in [53]. In the paper, a two-point estimation method is induced to solve for PLF problem. It stated that if the uncertain parameters considered can be measured or estimated, the distributions of all state variables and line-flow quantities can be accurately and efficiently evaluated with the proposed two-point estimate method through simple numerical computations. However, for better results, a larger number of estimate points could be used in the proposed method. Therefore, a 3-point estimation method and 5-point estimation method are developed in [54] and [55] respectively.

Based on the previous work in [55], a novel PLF assessment algorithm by using 5 point estimation method (5PEM) is proposed. Before applying the algorithm to the proposed microgrid, a IEEE 118 bus test system is adopted to perform power flow studies and verify the algorithm. In this test system, two wind farms are considered. The wind data for city of Milwaukee and Madison are utilized and fitted to Weibull distribution. The Cornish-Fisher expansion is applied to perform the probabilistic load flow in continuous PDF which is intuitive to power system operators. To actually represent the correlations between the wind farms, a bivariate distribution model based on the copula method is developed, and the spatiotemporal dependencies of two wind farms (located in Milwaukee and Madison) is discussed. The comparison of correlated and non-correlated situation demonstrates the significance of modeling wind farms with consideration of spatiotemporal dependencies.

Probabilistic Model for Wind Farm

Weibull distribution is considered to be the best probabilistic description of wind speed. The probability density function of the Weibull distribution is defined as follow,

$$f(x|\lambda, k) = \frac{k}{\lambda} \left(\frac{x}{\lambda}\right)^{k-1} e^{-\left(\frac{x}{\lambda}\right)^k} \quad (5.3.1)$$

Where k is called shape parameter, and λ is the scale parameter.

For analysis of probabilistic load flow (PLF), the injected power distribution of

wind turbine is needed, instead of wind speed distribution. Therefore, the power curve should be defined, which represents the relationship between the wind speed and the injected power of wind generator. In this paper, a VESTAS V82 type wind turbine is chosen. Figure 5.6 shows the power curve of V82.

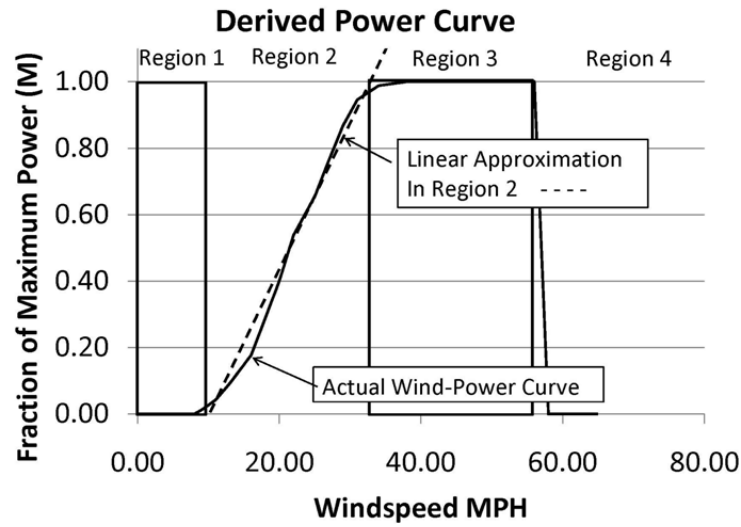


Figure 5.6: VESTAS V82 wind turbine power curve.

To simplify the problem, a linear approximation equation is used, which is shown in equation 5.3.2. Y is the injected power. X is actual wind speed. M is the maximum power of wind turbine. α and β are the linear parameters. V_{ci} , V_{co} and V_{no} , respectively, denote the cut-in wind speed, cut-out wind speed and nominal wind speed.

$$Y = \begin{cases} 0 & \text{if } X \leq V_{ci} \text{ or } X > V_{co} \\ \alpha + \beta X & \text{if } V_{ci} \leq X \leq V_{no} \\ M & \text{if } V_{no} \leq X \leq V_{co} \end{cases} \quad (5.3.2)$$

5-Point Estimation Method

To reduce computational efforts in PLF problems, the continuous probability distribution of input power generation source is replaced by a discrete distribution, sometimes known as the "Point Estimation" method. The basic idea behind the discretization scheme is to group the values of the continuous random variable into a finitely group.

Instead of a continuous PDF, the 5 points discrete probability mass function (PMF) is built to represent the injected power distribution. The basic algorithm is described as follows,

$$P_1 = Prob\{Y = 0\} = Prob(X \leq V_{ci}) + Prob(X > V_{co}) \quad (5.3.3)$$

$$P_5 = Prob\{Y = M\} = Prob(V_{no} \leq X \leq V_{co}) \quad (5.3.4)$$

For $V_{ci} \leq X \leq V_{no}$ redefine PDF of Y

$$\tilde{f}_Y(y|\lambda, k) = \frac{\frac{1}{\beta} f\left(\frac{y-\alpha}{\beta}|\lambda, k\right)}{1 - P_1 - P_5} \quad (5.3.5)$$

Notice that

$$\int_0^M \tilde{f}_Y(y|\lambda, k) dy = 1 \quad (5.3.6)$$

This fact will be used in the discretization of the continuous component of Y .

Define

$$\tilde{\mu}_Y = \int_0^M y \tilde{f}_Y(y|\lambda, k) dy \quad (5.3.7)$$

$$\tilde{\sigma}_Y^2 = \int_0^M (y - \tilde{\mu}_Y)^2 \tilde{f}_Y(y|\lambda, k) dy \quad (5.3.8)$$

$$\lambda_j = \int_0^M \left(\frac{y - \tilde{\mu}_Y}{\tilde{\sigma}_Y} \right)^j \tilde{f}_Y(y|\lambda, k) dy \quad (5.3.9)$$

$\tilde{\mu}_Y$ is the mean of Y ;

$\tilde{\sigma}_Y$ is the standard deviation of Y ;

λ_j is the j th central moment of Y ;

Let $z = \frac{y - \tilde{\mu}_Y}{\tilde{\sigma}_Y}$ denote the standardized value of Y .

The moment equations are given by

$$\sum_{i=2}^4 p_i z_i = \lambda_j \quad \text{for } j = 1, 2, 3, 4 \quad (5.3.10)$$

Where p_i is the probability corresponding to z_i .

Solve for above equation, we can obtain

$$\begin{cases} z_2 = \frac{\lambda_3}{2} - \sqrt{\lambda_4 - \frac{3\lambda_3^2}{4}} \\ z_3 = 0 \\ z_4 = \frac{\lambda_3}{2} + \sqrt{\lambda_4 - \frac{3\lambda_3^2}{4}} \end{cases} \quad (5.3.11)$$

$$\begin{cases} p_2 = \frac{-1}{z_2(z_4 - z_2)} \\ p_3 = 1 - p_2 - p_4 \\ p_4 = \frac{1}{z_4(z_4 - z_2)} \end{cases} \quad (5.3.12)$$

By use equation 5.3.11 and 5.3.12, we can estimate 3 point discrete distribution p_2 , p_3 and p_4 with corresponding location z_2 , z_3 and z_4 for \tilde{f}_Y . Then estimated point Y_i and associated probabilities P_i can be obtained as

$$\begin{cases} Y_2 = \tilde{\mu}_Y + \tilde{\sigma}_Y z_2 & \text{and } P_2 = p_2(1 - P_1 - P_5) \\ Y_3 = \tilde{\mu}_Y & \text{and } P_3 = p_3(1 - P_1 - P_5) \\ Y_4 = \tilde{\mu}_Y + \tilde{\sigma}_Y z_4 & \text{and } P_4 = p_4(1 - P_1 - P_5) \end{cases} \quad (5.3.13)$$

Cornish Fisher Expansion

By using 5-point estimation method, the load flow analysis only needs to be run 5 times instead of thousands of times by Monte Carlo method. However, the results are expressed in 5 distributed points, while the continuous PDF or cumulative distribution function (CDF) is more understandable and useful to illustrate the probabilistic load flow. So reconstructing the continuous distributions of nodes voltage and line flow is required. Theoretically, if we know the moments or cumulants of a random variable, it is possible to obtain its PDF or CDF. One approach is called Cornish Fisher expansion which is related to the Gram Charlier series. This approach provides an approximation of a quantile of a cumulative distribution function $F(x)$ in terms of the quantile of a normal $N(0,1)$ distribution and the cumulants of $F(x)$. [56]

Using first five cumulants, it can be expressed as:

$$\begin{aligned}
x(\alpha) \approx & \zeta(\alpha) + \frac{1}{6}(\zeta^2(\alpha) - 1)\kappa_3 + \frac{1}{24}(\zeta^3(\alpha) - 3\zeta(\alpha))\kappa_4 \\
& - \frac{1}{36}(2\zeta^3(\alpha) - 5\zeta(\alpha))\kappa_3^2 + \frac{1}{120}(\zeta^4(\alpha) - 6\zeta^2(\alpha) + 3)\kappa_5 \\
& - \frac{1}{24}(\zeta^4(\alpha) - 5\zeta^2(\alpha) + 2)\kappa_3\kappa_4 + \frac{1}{324}(12\zeta^4(\alpha) - 53\zeta^2(\alpha) + 17)\kappa_3^2
\end{aligned} \tag{5.3.14}$$

Where,

$$x(\alpha) = F^{-1}(x) \tag{5.3.15}$$

$$\zeta(\alpha) = \Phi^{-1}(\alpha) \tag{5.3.16}$$

κ_i is the i th cumulants, which are defined as follows:

$$\begin{aligned}
\kappa_1 &= \mu \\
\kappa_2 &= \mu_2 \\
\kappa_3 &= \mu_3 \\
\kappa_4 &= \mu_4 - 3\mu_2^2 \\
\kappa_5 &= \mu_5 - 10\mu_3\mu_2
\end{aligned} \tag{5.3.17}$$

Where, $\mu = E(x)$, $\mu_r = E[(x - \mu)^r]$.

Copula Method for Modeling Joint Distribution

Since power systems may have more than one wind farm, it is necessary to consider the wind speed dependencies. In this paper, a bivariate distribution of two wind farms (located in Milwaukee and Madison respectively) is constructed by using of the copula

method. The Copulas are functions that join or couple multivariate distribution functions to their one-dimensional marginals. Alternatively, copulas are multivariate distribution functions whose one-dimensional marginals are uniform on the interval $[0,1]$. [57]

Let F_{XY} denote the joint cumulative distribution function with marginals $F_X(x)$ and $F_Y(y)$. Then there exists a copula C such that for all x and y ,

$$F_{XY}(x, y) = C(F_X(x), F_Y(y)) \quad (5.3.18)$$

In the paper, a Clayton copula function is chosen such that

$$F_{XY}(x, y) = (F_X(x)^{-a} + F_Y(y)^{-a} - 1)^{-\frac{1}{a}} \quad (5.3.19)$$

Where a is the correlation coefficient. Then the bivariate probability density function can be obtained

$$\begin{aligned} f_{XY}(x, y) &= \frac{\partial^2 F_{XY}(x, y)}{\partial x \partial y} \\ &= (1 + a)F_X(x)^{-a-1}F_Y(y)^{-a-1} \\ &\quad \cdot (F_X(x)^{-a} + F_Y(y)^{-a} - 1)^{-\frac{1}{a}-2} f_X(x)f_Y(y) \end{aligned} \quad (5.3.20)$$

The injected power is in the form of mixed distribution model (zero power and max power are defined by cut-in, cut-out and nominal wind speed), therefore, the

continuous part of distribution can be redefined as:

$$\begin{aligned}
f_{XY}(\tilde{x}, \tilde{y}) &= \frac{(1+a)}{\beta_1 \beta_2 p_{11-33}} \left(\exp\left(-\frac{\tilde{x}-\alpha_1}{\beta_1 \lambda_1}\right)^{k_1} \right)^{-a-1} \left(\exp\left(-\frac{\tilde{y}-\alpha_2}{\beta_2 \lambda_2}\right)^{k_2} \right)^{-a-1} \\
&\cdot \left(\left(\exp\left(-\frac{\tilde{x}-\alpha_1}{\beta_1 \lambda_1}\right)^{k_1} \right)^{-a} + \left(\exp\left(-\frac{\tilde{y}-\alpha_2}{\beta_2 \lambda_2}\right)^{k_2} \right)^{-a} - 1 \right)^{-\frac{1}{a}-2} \quad (5.3.21) \\
&\cdot f\left(\frac{\tilde{x}-\alpha_1}{\beta_1} | \lambda_1, k_1\right) f\left(\frac{\tilde{y}-\alpha_2}{\beta_2} | \lambda_2, k_2\right)
\end{aligned}$$

Where, $p_{11-33} = \int_{ci1}^{cr1} \int_{ci2}^{cr2} f_{XY}(x, y)$ denotes the weight of linear region of power curve.

Then the central moments can be obtained by:

$$\lambda_{ij} = \int_0^{M1} \int_0^{M2} \left(\frac{\tilde{x}-\mu_x}{\sigma_x} \right)^i \left(\frac{\tilde{y}-\mu_y}{\sigma_y} \right)^j f(\tilde{x}, \tilde{y} | \lambda_1, k_1, \lambda_2, k_2) dx dy \quad (5.3.22)$$

Similarly, by applying equations 5.3.10 - 5.3.13, we can obtain 25 points joint distribution of injected power of two wind farms. The load flow analysis, thus, can be performed by using these discretized points.

Simulation Results in IEEE 118 Bus System

A. Simulation conditions and assumptions

The performance of the proposed method is tested on IEEE 118 bus system (refer to Power Systems Test Case Archive [31]), modified to include 2 wind farms which are located at Bus 10 and Bus 12. The research is based on the assumption that all wind turbines in the same wind farm have similar wind speed distribution such that we can regard each wind farm as an aggregated wind turbine which meets the

approximately linear power curve shown in Figure 5.6. The parameters of four wind farms are shown in Table 5.5.

Table 5.5: Parameters of two wind farms

	k	λ	α	β	Max Power
Bus10	2.6668	13.0065	-163.64	45.76	450MW
Bus12	2.5034	10.0434	-30.91	8.64	85MW

In the paper, the voltage at the bus 38 and the line flows in the Branch 54 (from Bus 30 to Bus 38) are selected to illustrate the performance of the proposed PLF algorithm, because they are the worse cases in the results.

B. Comparison of 5PEM with Monte Carlo Method

In this simulation, the performance of 5-point estimation (5PEM) method is tested by comparing with 1000 times of Monte Carlo (MC) method. In this case, only Bus 10 is selected as random source.

Figure 5.7 (a) shows the histogram of wind speed (1000 points), and (b) gives the corresponding injected power. By performing load flow analysis 1000 times, the line flow and voltage distribution can be plotted in Matlab. Picture (c) is 5 points distribution of injected power generated by 5PEM method which has equivalent moments and cumulants to the distribution shown in (b). By using Cornish-Fisher expansion, we can reconstruct the continuous PDF of 5 points distribution, shown in (d).

By carrying out load flow analysis, both MC method and 5PEM method give out the distribution of voltages and line flows. Figure 5.8 shows the CDF of bus 38

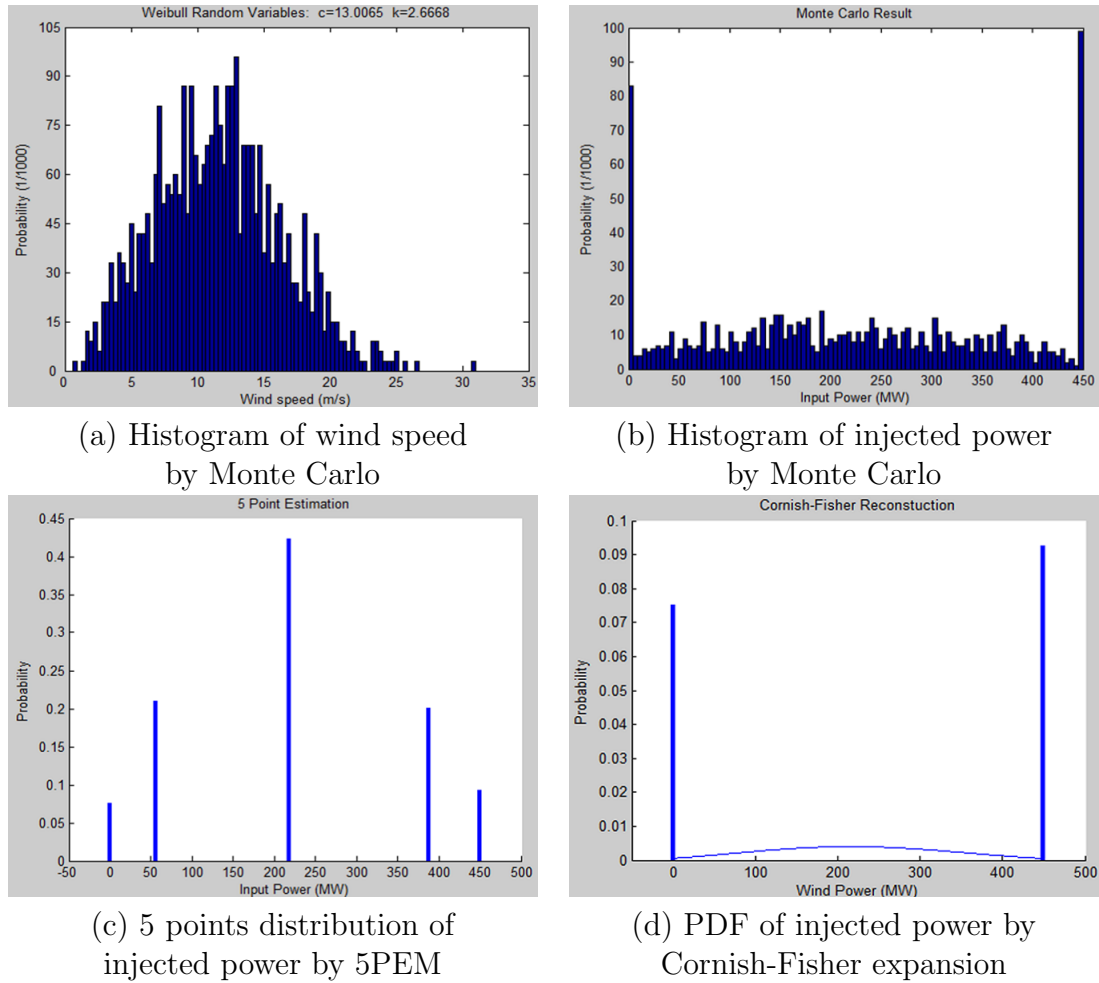
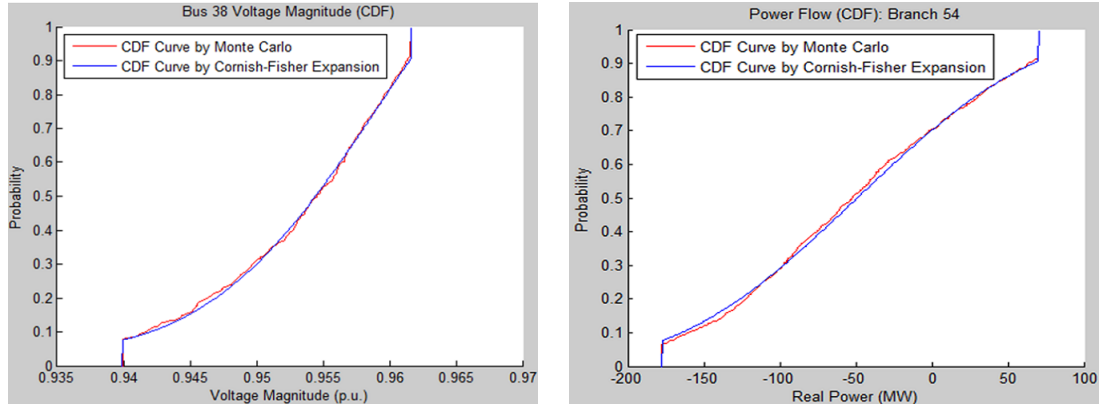


Figure 5.7: Wind farm modeling by Monte Carlo and 5PEM

voltage magnitude and the CDF of branch 54 (from bus 30 to bus 38) real power flow. From the figures we can easily find that the proposed 5PEM method shows a high accuracy by comparing the results with those from MC method. In addition, by calculating the root mean square (RMS) error, the difference between 5PEM and MC method is shown in Table 5.6. However, MC requires to run load flow 1000 times while the proposed 5PEM method requires only 5 times.



(a) The CDF comparison of bus 38 voltage magnitude

(b) The CDF comparison of branch 54 real power flow

Figure 5.8: The results comparison between MC and 5PEM

Table 5.6: RMS error between MC and 5PEM		
	Bus 38 voltage	Branch 54 Line Flow
RMS error(%)	0.1223	0.1892

C. Effects of VAR Compensation

In the power system, reactive power compensation or called VAR compensation is widely used to regulate bus voltage, reduce energy loss, and enhance reliability. PLF could be an assessment tool for VAR compensation. A simple example is shown in Figure 5.9 which gives the probabilities of voltage magnitude at Bus 38 when it is lower than 0.95 per unit and greater than 0.96 per unit. In the original case, the probability of the voltage lower than 0.95 is 30.8%. If it is necessary to improve Bus 38 voltage, we can simply add shunt capacitor at Bus 38. For instance, after adding 40 MVAR, that probability decreases to 0%.

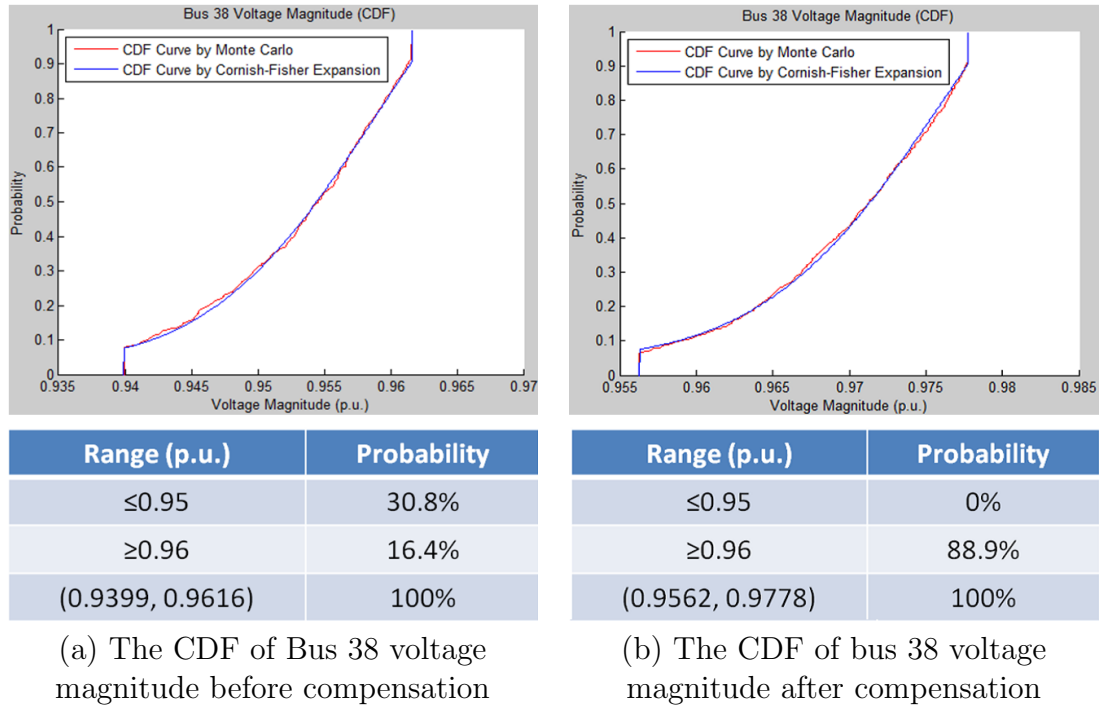
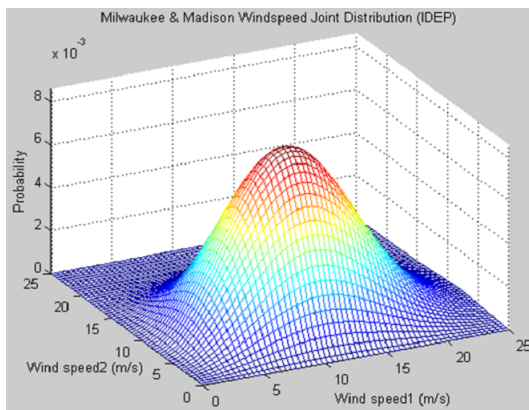


Figure 5.9: The comparison of CDF of bus 38 voltage magnitude before and after VAR compensation.

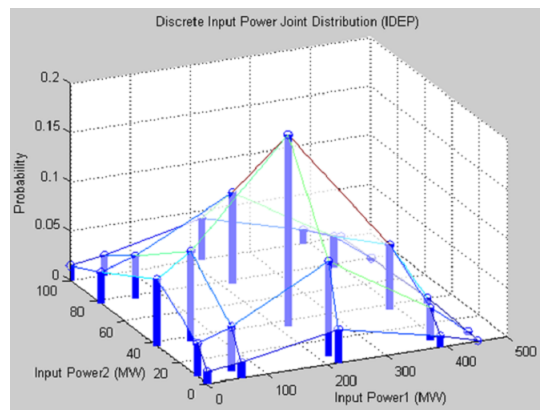
D. Simulation of PLF Considering Spatiotemporal Dependencies of Two Wind Farms

Based on the copula method discussed above, a simulation of the PLF considering two interdependent wind farms is carried out. Bus 10 and Bus 12 are selected as random sources. The wind speed parameters are obtained from two observatories located in Milwaukee and Madison, WI. The correlation coefficient is fitted by the real data. Figure 5.10 (a) and (c) show the continuous bivariate PDF of wind speed assuming dependent and independent. (b) and (c) shows the 25 points distribution of injected power using 5PEM method, also assuming dependent vs independent. By

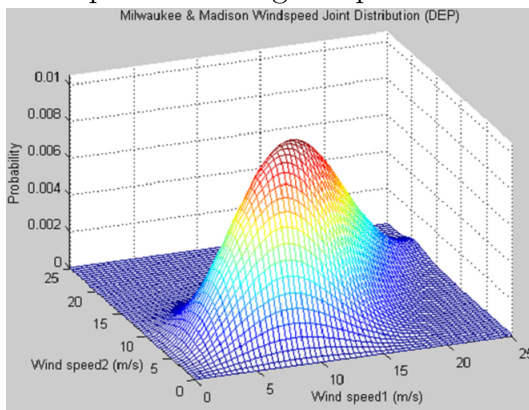
comparing of (a) and (c), we can see that the dependent joint distribution tend to concentrate on the diagonal, which means that the wind speed at location 1 tends to be not too much difference of location 2. For instance, if the average wind speed at Milwaukee is 10 m/s, the most possible average wind speed at Madison is around 10 m/s.



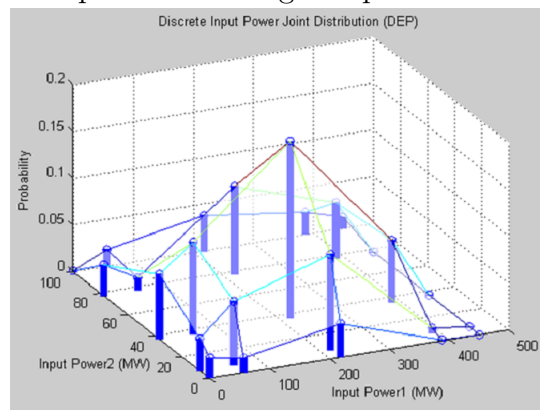
(a) The bivariate PDF of wind speed assuming independent



(b) The bivariate PDF of injected power assuming independent



(c) The bivariate PDF of wind speed assuming dependent



(d) The bivariate PDF of injected power assuming dependent

Figure 5.10: Bivariate distribution model for wind farms

By performing load flow analysis using these 25 points and applying Cornish-Fisher expansion, the probability distribution of bus voltage and line flow can be obtained. Figure 5.11 shows the comparison of CDF assuming independent and dependent. Obviously, the results indicate a significantly difference that demonstrates the importance of modeling wind farms with considering spatiotemporal dependencies.

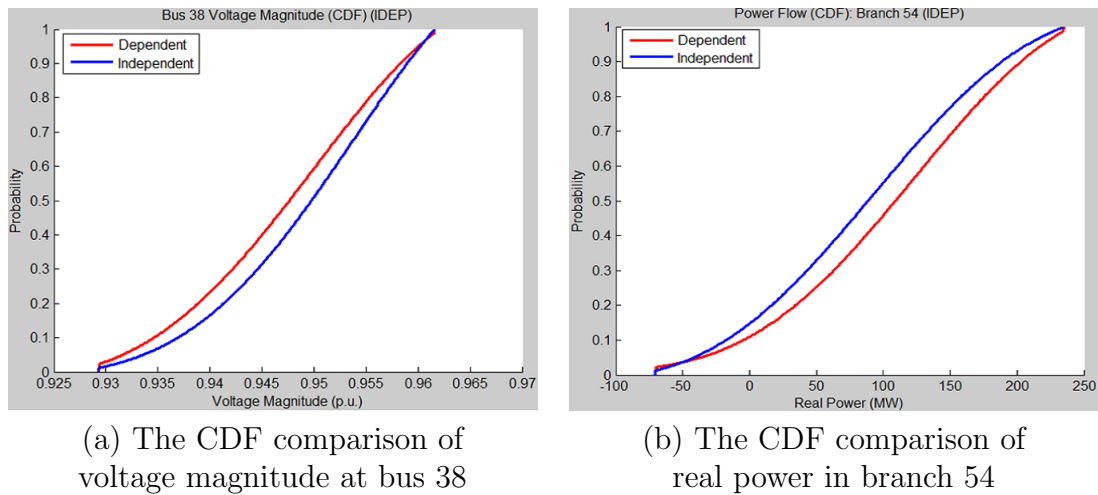


Figure 5.11: The CDF comparison between dependent and independent situation.

PLF Assessment for Microgrid

In this section, the model based PLF assessment discussed above is applied to the proposed microgrid. The main purpose is to evaluate the impact of wind power on the microgrid with different system configuration. There are several assumptions made in this study: 1) A peak load condition is considered since we assume that no time series load information are available; 2) Solar PV is ignored; 3) two wind generations are

considered to be located far from each other with different wind speed distributions. In this study, 10 year wind data for city of Milwaukee and Madison are fitted by Weibull distributions, which are applied for two wind turbines (Each one is 750kW rated).

Following the equations 5.3.1-5.3.22 as stated above, a 25-point distribution of two dependent wind turbines are obtained shown in Table 5.7.

Table 5.7: 25 point distribution of two dependent wind turbines

	Prob. W1	W1 Power (kW)	Prob. W2	W2 Power(kW)	Joint Prob.
1	0.075153	0	0.160093	0	0.022347
2	0.075153	0	0.21362	54.2458	0.034373
3	0.075153	0	0.458035	275.964	0.069287
4	0.075153	0	0.154801	581.9281	0.032807
5	0.075153	0	0.01345	750	0.001277
6	0.209602	94.00282	0.160093	0	0.016054
7	0.209602	94.00282	0.21362	54.2458	0.068152
8	0.209602	94.00282	0.458035	275.964	0.097781
9	0.209602	94.00282	0.154801	581.9281	0.013577
10	0.209602	94.00282	0.01345	750	0.018056
11	0.422509	363.4498	0.160093	0	0.035576
12	0.422509	363.4498	0.21362	54.2458	0.101615
13	0.422509	363.4498	0.458035	275.964	0.189226
14	0.422509	363.4498	0.154801	581.9281	0.094056
15	0.422509	363.4498	0.01345	750	0.037562
16	0.200057	645.7523	0.160093	0	0.001163
17	0.200057	645.7523	0.21362	54.2458	0.005157
18	0.200057	645.7523	0.458035	275.964	0.0656
19	0.200057	645.7523	0.154801	581.9281	0.059326
20	0.200057	645.7523	0.01345	750	0.023555
21	0.09268	750	0.160093	0	1.20E-05
22	0.09268	750	0.21362	54.2458	0.000305
23	0.09268	750	0.458035	275.964	0.000614
24	0.09268	750	0.154801	581.9281	0.000291
25	0.09268	750	0.01345	750	0.012228

After importing these data into the microgrid model in PSCAD, we are able to have the steady state power flow solutions for all bus voltages. The same selected bus voltages are listed in the following tables for three cases.

25 POINTS LOAD FLOW RESULTS OF SELECTED BUS VOLTAGES IN CASE 1

Point	Bus 800	Bus 814	Bus 818	Bus 822	Bus 824	Bus 832	Bus 840	Bus 848	Bus 854	Bus 890
1	1.040287	0.971764	0.981717	0.955905	1.003539	0.965269	0.958832	0.956737	0.988676	0.963544
2	1.041093	0.977631	0.986897	0.961311	1.010339	0.975685	0.970475	0.968082	0.996844	0.969429
3	1.044251	0.982852	0.992335	0.966713	1.018163	0.985841	0.98788	0.982296	1.005269	0.974263
4	1.042942	1.004644	1.016076	0.988882	1.018416	1.010888	1.018838	1.006621	1.013571	0.982295
5	1.039851	0.990521	0.998786	0.971757	1.013316	1.000344	1.010179	0.995935	1.006488	0.975828
6	1.034996	0.949755	0.964097	0.937844	1.000951	0.950944	0.946192	0.944862	0.981726	0.956071
7	1.037197	0.95547	0.966379	0.940393	1.007575	0.961148	0.957702	0.955919	0.989444	0.96105
8	1.043716	0.988606	0.99612	0.970641	1.016456	0.989355	0.992529	0.98745	1.005416	0.975526
9	1.040464	1.006847	1.00568	0.980758	1.016778	1.015684	1.023671	1.011592	1.013779	0.983089
10	1.035171	0.984844	0.985054	0.95931	1.011931	1.000058	1.010812	0.997213	1.005135	0.974795
11	1.048481	0.97401	0.981193	0.955538	1.006937	0.963881	0.9651	0.967421	0.989888	0.962618
12	1.044016	0.973231	0.985809	0.959371	1.006732	0.968624	0.970932	0.972692	0.991351	0.963811
13	1.044238	0.998586	0.999387	0.97433	1.02153	1.006207	1.016252	1.013747	1.013726	0.981165
14	1.041162	0.999638	1.013222	0.985005	1.015563	1.010783	1.022829	1.013873	1.011341	0.980051
15	1.029898	0.991591	1.003456	0.975135	1.014375	1.015432	1.031761	1.021309	1.012276	0.981622
16	1.037553	0.977188	0.984546	0.959174	1.012401	0.981875	0.986037	0.990669	1.000071	0.971748
17	1.044374	0.990804	1.001916	0.97597	1.019163	0.995566	1.000725	1.004744	1.009208	0.97778
18	1.043608	1.005186	1.005594	0.980515	1.019027	1.014937	1.022437	1.019997	1.015097	0.982878
19	1.010243	0.967456	0.967385	0.941517	1.002231	1.005705	1.02166	1.015474	1.000207	0.974409
20	0.991572	0.944152	0.948932	0.922326	0.998606	1.004061	1.025465	1.016006	0.996994	0.972931
21	1.028838	0.96627	0.977439	0.950515	1.009795	0.985569	0.986859	0.990687	0.999043	0.969789
22	1.03365	0.978154	0.983897	0.957497	1.008296	0.989406	0.991989	0.995534	0.999437	0.971169
23	1.035754	0.99509	1.00203	0.976108	1.017659	1.01457	1.022686	1.021725	1.013988	0.982365
24	0.996879	0.9508	0.968671	0.939323	1.006635	1.008641	1.026013	1.022376	1.004894	0.977873
25	0.989356	0.946635	0.958161	0.931084	0.999516	1.008842	1.033622	1.025717	0.999665	0.97611

25 POINTS LOAD FLOW RESULTS OF SELECTED BUS VOLTAGES IN CASE 2

Point	Bus 800	Bus 814	Bus 818	Bus 822	Bus 824	Bus 832	Bus 840	Bus 848	Bus 854	Bus 890
1	1.042574	0.958235	0.967503	0.941221	0.996798	1.029279	1.022249	1.020014	0.980126	0.995507
2	1.033469	0.94864	0.956382	0.930113	0.992978	1.026141	1.018845	1.016787	0.97662	0.991942
3	1.031588	0.942857	0.955165	0.928393	0.994588	1.021957	1.020773	1.016067	0.977512	0.986685
4	1.019063	0.936596	0.937007	0.910379	0.991678	1.015569	1.020183	1.009796	0.978257	0.972799
5	1.020052	0.941524	0.935152	0.90802	0.991707	1.004628	1.014493	1.0008	0.979912	0.95757
6	1.04267	0.945827	0.95182	0.925666	0.992306	1.01567	1.011042	1.009904	0.971815	0.982389
7	1.042314	0.949489	0.961426	0.934825	0.996778	1.025487	1.021728	1.01982	0.977969	0.990867
8	1.022826	0.933717	0.942117	0.915645	0.989348	1.024427	1.023776	1.019267	0.972743	0.988414
9	1.023888	0.94784	0.946533	0.91936	0.993631	1.009536	1.015846	1.005219	0.982443	0.963695
10	1.019114	0.940497	0.946636	0.918989	0.987619	1.018543	1.030117	1.018369	0.975601	0.975951
11	1.025591	0.936995	0.947097	0.920545	0.992701	1.021295	1.017913	1.019562	0.976048	0.985761
12	1.037765	0.942473	0.94754	0.921228	0.997405	1.019324	1.019203	1.019631	0.978078	0.98389
13	1.021278	0.931204	0.937446	0.910663	0.986578	1.016369	1.020732	1.018338	0.970066	0.978192
14	0.998063	0.912766	0.927373	0.898792	0.974275	1.015439	1.02587	1.019391	0.961913	0.973037
15	0.999563	0.924983	0.921388	0.894384	0.987516	1.014315	1.03082	1.02059	0.978337	0.968422
16	1.030146	0.945393	0.946028	0.919686	0.991985	1.012328	1.01433	1.017994	0.976347	0.974154
17	1.015951	0.926919	0.937476	0.91037	0.984275	1.019209	1.02124	1.023569	0.968383	0.981845
18	0.999129	0.910628	0.91844	0.890554	0.973777	1.014239	1.020684	1.020811	0.960235	0.972612
19	0.986067	0.909419	0.920959	0.892413	0.976663	1.021475	1.036724	1.031758	0.968701	0.973895
20	0.988245	0.922152	0.924079	0.895185	0.981985	1.018011	1.037773	1.030489	0.977711	0.967378
21	1.014756	0.927195	0.934772	0.907733	0.991102	1.017222	1.019504	1.023596	0.975978	0.97847
22	1.016439	0.934383	0.939623	0.912897	0.991276	1.015413	1.019074	1.023068	0.977658	0.976068
23	0.999874	0.920373	0.928204	0.900615	0.977282	1.009521	1.018384	1.019718	0.966535	0.965433
24	0.988586	0.920073	0.925487	0.896087	0.983294	1.018889	1.035938	1.032299	0.978201	0.968966
25	0.985179	0.918242	0.937024	0.90705	0.9794	1.019551	1.03748	1.033205	0.975422	0.969348

25 POINTS LOAD FLOW RESULTS OF SELECTED BUS VOLTAGES IN CASE 3

Point	Bus 800	Bus 814	Bus 818	Bus 822	Bus 824	Bus 832	Bus 840	Bus 848	Bus 854	Bus 890
1	1.040287	0.971764	0.981717	0.955905	1.003539	0.965269	0.958832	0.956737	0.988676	0.963544
2	1.041093	0.977631	0.986897	0.961311	1.010339	0.975685	0.970475	0.968082	0.996844	0.969429
3	1.044251	0.982852	0.992335	0.966713	1.018163	0.985841	0.98788	0.982296	1.005269	0.974263
4	1.042942	1.004644	1.016076	0.988882	1.018416	1.010888	1.018838	1.006621	1.013571	0.982295
5	1.039851	0.990521	0.998786	0.971757	1.013316	1.000344	1.010179	0.995935	1.006488	0.975828
6	1.034996	0.949755	0.964097	0.937844	1.000951	0.950944	0.946192	0.944862	0.981726	0.956071
7	1.037197	0.95547	0.966379	0.940393	1.007575	0.961148	0.957702	0.955919	0.989444	0.96105
8	1.043716	0.988606	0.99612	0.970641	1.016456	0.989355	0.992529	0.98745	1.005416	0.975526
9	1.040464	1.006847	1.00568	0.980758	1.016778	1.015684	1.023671	1.011592	1.013779	0.983089
10	1.035171	0.984844	0.985054	0.95931	1.011931	1.000058	1.010812	0.997213	1.005135	0.974795
11	1.048481	0.97401	0.981193	0.955538	1.006937	0.963881	0.9651	0.967421	0.989888	0.962618
12	1.044016	0.973231	0.985809	0.959371	1.006732	0.968624	0.970932	0.972692	0.991351	0.963811
13	1.044238	0.998586	0.999387	0.97433	1.02153	1.006207	1.016252	1.013747	1.013726	0.981165
14	1.041162	0.999638	1.013222	0.985005	1.015563	1.010783	1.022829	1.013873	1.011341	0.980051
15	1.029898	0.991591	1.003456	0.975135	1.014375	1.015432	1.031761	1.021309	1.012276	0.981622
16	1.037553	0.977188	0.984546	0.959174	1.012401	0.981875	0.986037	0.990669	1.000071	0.971748
17	1.044374	0.990804	1.001916	0.97597	1.019163	0.995566	1.000725	1.004744	1.009208	0.97778
18	1.043608	1.005186	1.005594	0.980515	1.019027	1.014937	1.022437	1.019997	1.015097	0.982878
19	1.010243	0.967456	0.967385	0.941517	1.002231	1.005705	1.02166	1.015474	1.000207	0.974409
20	0.991572	0.944152	0.948932	0.922326	0.998606	1.004061	1.025465	1.016006	0.996994	0.972931
21	1.028838	0.96627	0.977439	0.950515	1.009795	0.985569	0.986859	0.990687	0.999043	0.969789
22	1.03365	0.978154	0.983897	0.957497	1.008296	0.989406	0.991989	0.995534	0.999437	0.971169
23	1.035754	0.99509	1.00203	0.976108	1.017659	1.01457	1.022686	1.021725	1.013988	0.982365
24	0.996879	0.9508	0.968671	0.939323	1.006635	1.008641	1.026013	1.022376	1.004894	0.977873
25	0.989356	0.946635	0.958161	0.931084	0.999516	1.008842	1.033622	1.025717	0.999665	0.97611

By using Cornish-Fisher expansion, an estimated continuous distribution for all bus voltages in three cases are able to be obtained. Figure 5.12 shows a comparison of cumulative distribution functions of Bus 822 voltage in three cases. The same voltage classification is defined as damageable low voltage, low voltage, normal voltage, and damageable high voltage, so that the probabilities of each class in three cases are obtained. Table 5.8-5.10 list selected bus voltages probabilities for three cases, respectively.

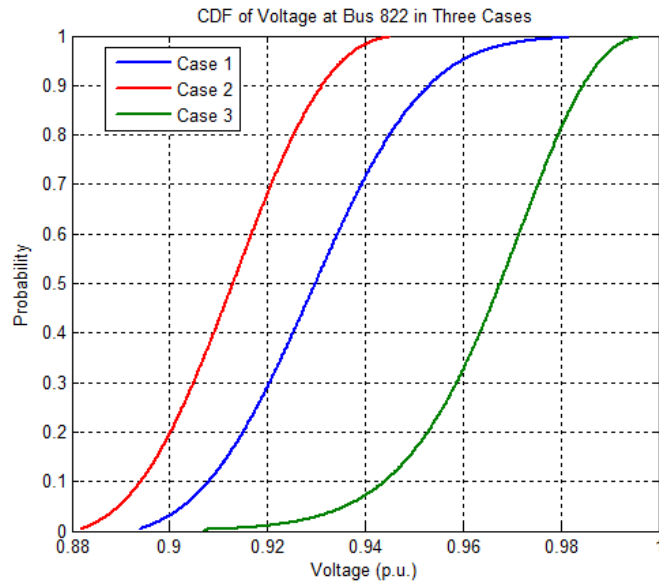


Figure 5.12: The comparison of cumulative distribution of voltage at bus 822 in three cases.

Table 5.8: Summary of classified probabilities of selected bus voltages in case 1

	Damageable Low Voltage (≤ 0.92)	Low Voltage (0.92,0.96]	Normal Voltage (0.96,1.05)	Damageable High Voltage (≥ 1.05)
Bus 800	0	0	94.63%	5.37%
Bus 814	4.09%	59.21%	36.70%	0
Bus 818	0.02%	58.32%	41.66%	0
Bus 822	29.12%	65.94%	4.94%	0
Bus 824	0	0	1	0
Bus 832	0	0	1	0
Bus 840	0	0	1	0
Bus 848	0	1.04%	99.96%	0
Bus 854	0	0	1	0
Bus 890	0	8.85%	91.15%	0

Table 5.9: Summary of classified probabilities of selected bus voltages in case 2

	Damageable Low Voltage (≤ 0.92)	Low Voltage (0.92,0.96]	Normal Voltage (0.96,1.05)	Damageable High Voltage (≥ 1.05)
Bus 800	0	0	1	0
Bus 814	20.33%	79.67%	0	0
Bus 818	7.08%	86.11%	6.81%	0
Bus 822	67.72%	32.28%	0	0
Bus 824	0	0	1	0
Bus 832	0	0	1	0
Bus 840	0	0	1	0
Bus 848	0	0	1	0
Bus 854	0	3.75%	96.25%	0
Bus 890	0	0	1	0

Table 5.10: Summary of classified probabilities of selected bus voltages in case 3

	Damageable Low Voltage (≤ 0.92)	Low Voltage (0.92,0.96]	Normal Voltage (0.96,1.05)	Damageable High Voltage (≥ 1.05)
Bus 800	0	0	94.52%	5.48%
Bus 814	0	8.69%	91.31%	0
Bus 818	0	4.09%	95.91%	0
Bus 822	1.04%	31.23%	67.72%	0
Bus 824	0	0	1	0
Bus 832	0	5.59%	94.41%	0
Bus 840	0	6.81%	93.19%	0
Bus 848	0	7.08%	92.92%	0
Bus 854	0	0	1	0
Bus 890	0	5.26%	94.74%	0

From tables above, the conclusions similar to data based analysis can be drawn that are 1) case 2 has a little bit improvement on downstream bus voltages but it impairs the upstream voltage profiles. 2) case 3 has an overall better voltage performance among three cases. 3) Wind power has more impact on bus 814, bus 818 and bus 822. Figure 5.13- 5.15 illustrate three cases in column charts.

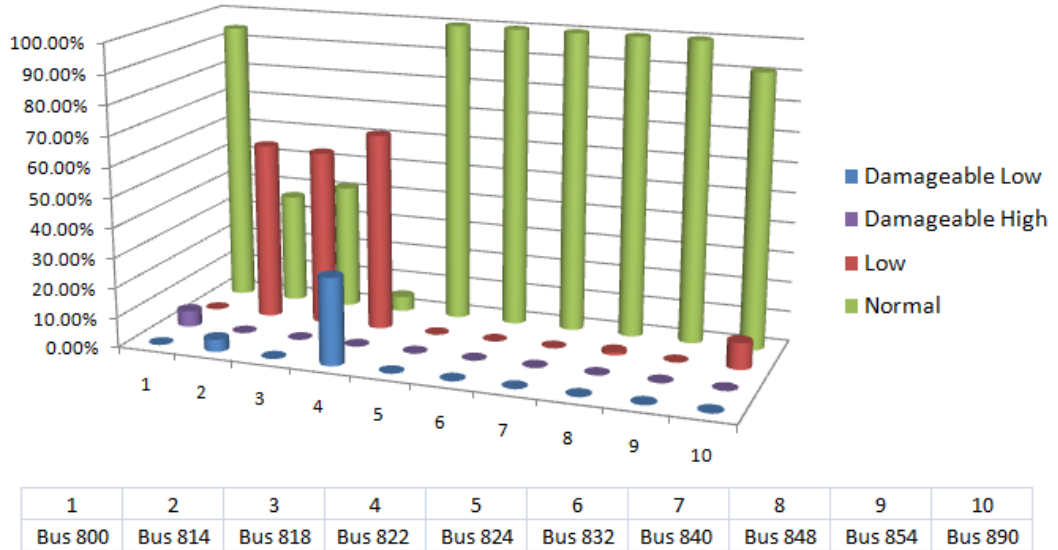


Figure 5.13: The column chart of case 1.

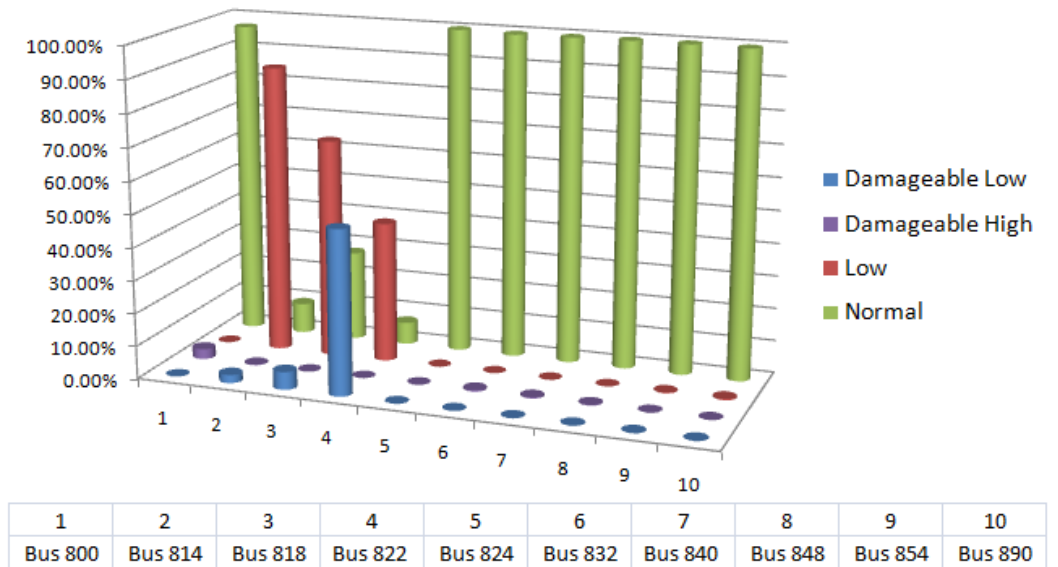


Figure 5.14: The column chart of case 2.

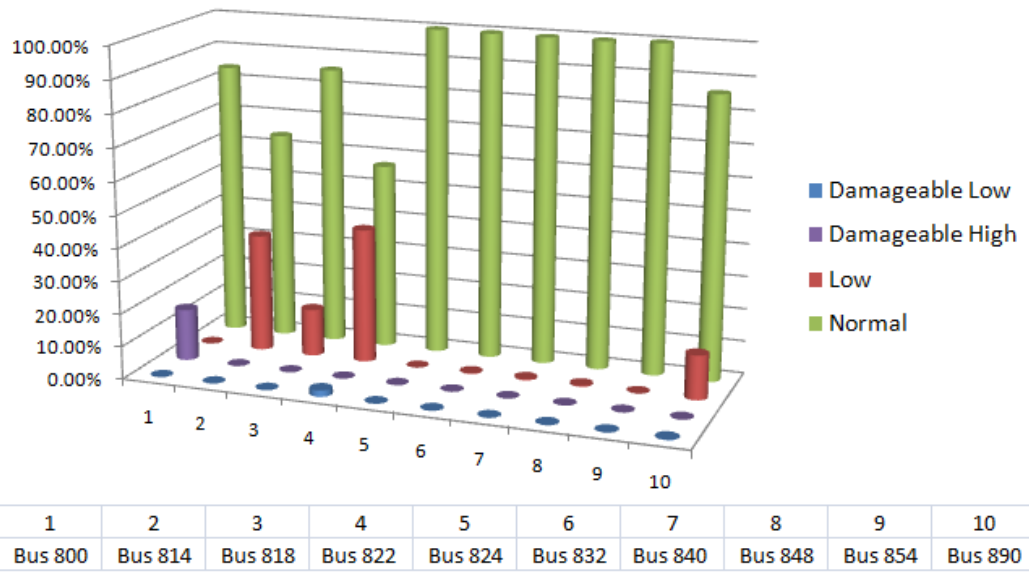


Figure 5.15: The column chart of case 3.

Chapter 6

Extended Research

The proposed microgrid discussed above serves as a benchmark for microgrid analysis and development. The mathematical models of microgrid components and their controls as well as system level operation and management have been presented. In this chapter, an in building microgrid at City of Fort Sill, OK., is modeled by following a similar procedure. The Fort Sill Microgrid (FSMG) consists of 2 natural gas generator, a wind turbine, a Solar PV panel, and a battery. The microgrid components are modified and scaled from the models discussed in chapter 3 to meet the requirements of FSMG. Several simulations for FSMG operation are conducted. Moreover, an initial research for extended FSMG and the concept of multi-microgrid have been introduced and discussed. At last, a 1MW multi-inverter based microgrid built at Eaton Power Lab is presented and various experiments have been conducted.

6.1 Modeling of Fort Sill Microgrid

The FSMG configuration is shown in Figure 6.1. The main bus is rated at 480V/60Hz. The nominal capacity of FSMG is 630kW. It is connected to the utility grid through a 0.48kV/13.20kV transformer and a static switch. The generations in this microgrid include two natural gas generators each rated at 190 kW, one 30 kW solar PV system, a 2.5 kW wind turbine and a 250 kW energy storage device. The solar PV and wind turbine generators are connected to the system through inverters operating in current mode and the energy storage inverter is operated in voltage mode. The system also includes various motor loads and variable power loads. Motor loads mainly include chillers, water pumps and air compressors. This microgrid can operate in grid-tie mode and island mode. The energy storage system is always connected to the microgrid with a capability of providing maximum 400kW for 3 mins (250kW for continuous).

Since all the FSMG components are modeled similar to IEEE 34 bus microgrid, the detailed models are not necessarily presented in the paper. The parameters of natural gas generator is listed in Table 6.1.

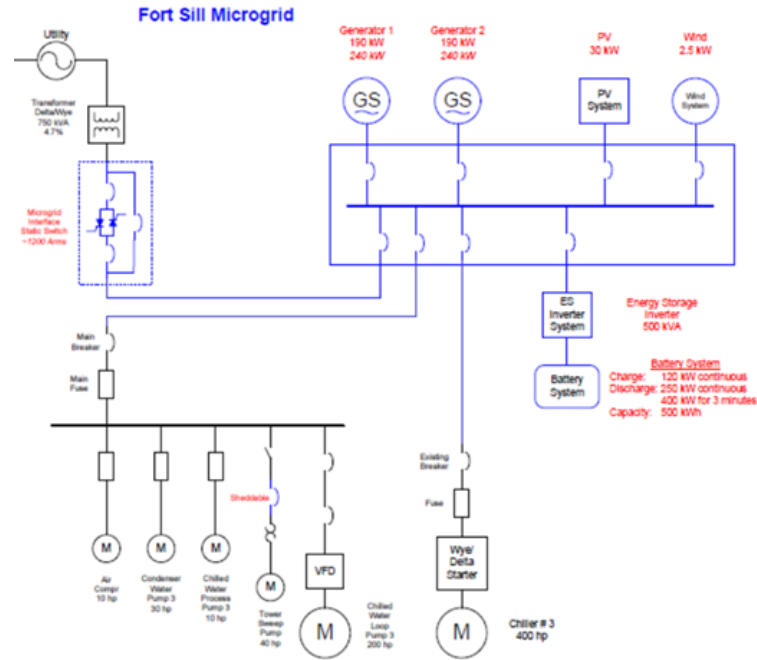


Figure 6.1: The one-line diagram of Fort Sill Microgrid.

Table 6.1: Parameters of 240kVA natural gas generator used in FSMG

Rated Line-to-Neutral Voltage	V_r	277 [V]
Rated Line Current	I_r	288 [A]
Inertia Constant	H	0.64 [s]
Armature Time Constant	T_a	0.017 [s]
Potier Reactance	X_p	0.147 [pu]
Unsaturated Reactance d-axis	X_d	2.877 [pu]
Unsaturated Transient Reactance	X'_d	0.184 [pu]
Unsaturated Transient Time (Open)	T'_{do}	1.46 [s]
Unsaturated Sub-transient Reactance	X''_d	0.166 [s]
Unsaturated Sub-transient Time (Open)	T''_{do}	0.162 [s]
Unsaturated Reactance Q-axis	X_q	1.415 [pu]
Unsaturated Sub-transient Reactance	X''_q	0.15 [pu]
Unsaturated Sub-transient Time (Open)	T''_{qo}	0.162 [s]

Simulation Condition

Same wind speed and solar irradiation profiles have been applied shown in Figures 6.2 and 6.3. The power ratings have been scaled to 50kW and 30kW for wind and solar generations respectively. A constant peak load with 0.85 power factor is considered.

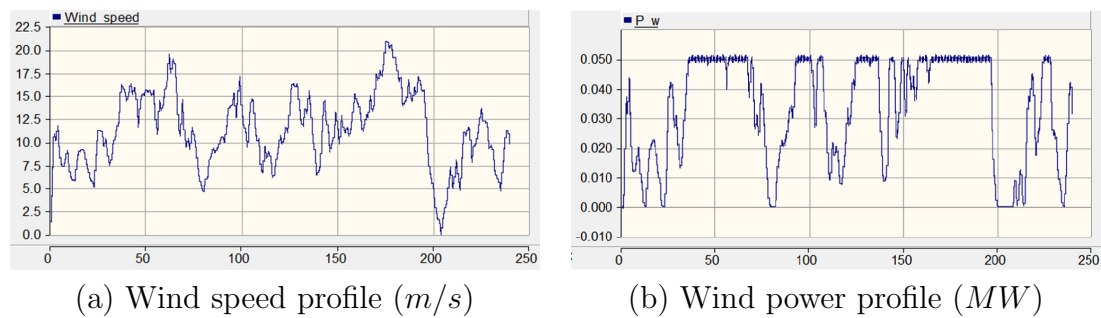


Figure 6.2: Measured wind speed data and corresponding power delivered by wind turbine.

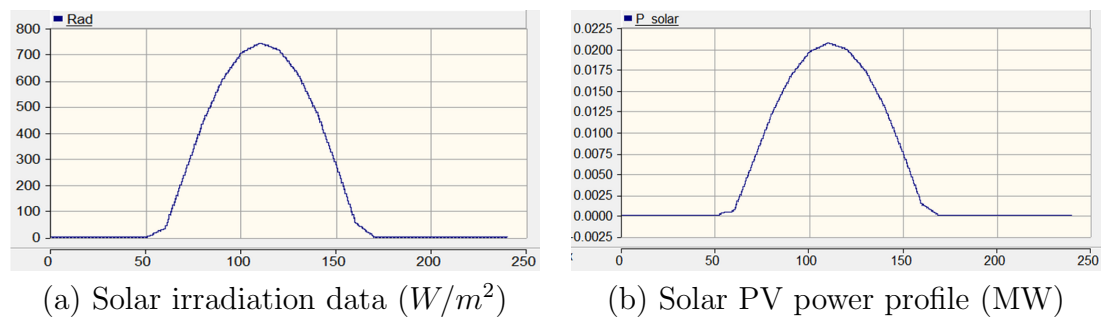


Figure 6.3: Measured solar irradiation data and corresponding power delivered by Solar PV.

Simulation in Island Mode

The selected simulation results are depicted in Figures 6.4 and 6.5.

P_d & Q_d - The real and reactive power delivered by natural gas generator 1.

P_b & Q_b - The real power and reactive delivered by battery.

P_w & Q_w - The real power and reactive delivered by wind turbine.

P_{pv} & Q_{pv} - The real power and reactive delivered by Solar PV.

Frequency - microgrid frequency measured at main bus.

VM - Voltage at Main bus.

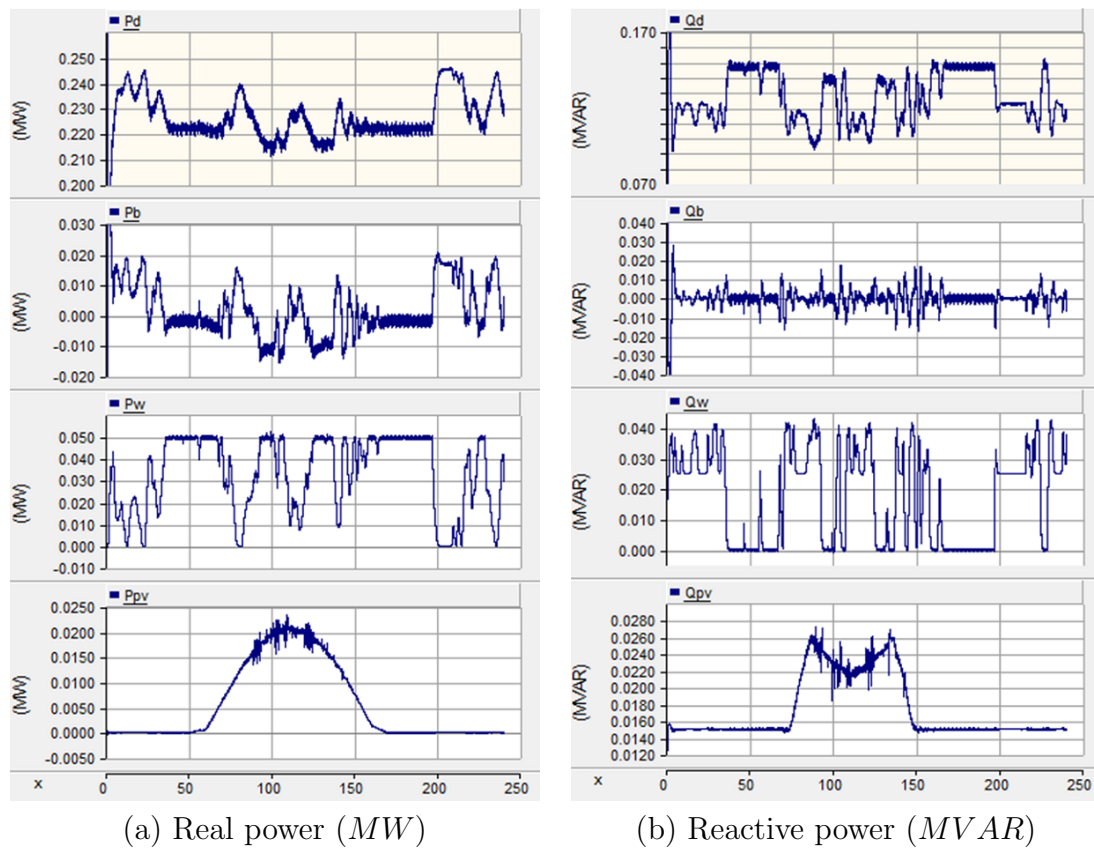


Figure 6.4: Real and reactive power delivered by natural gas generator, battery, wind turbine and Solar PV.

The low frequency oscillations (about 1-2 Hz) of voltage magnitude and frequency are caused by the motor loads, and mismatch of exciter and governor controls between

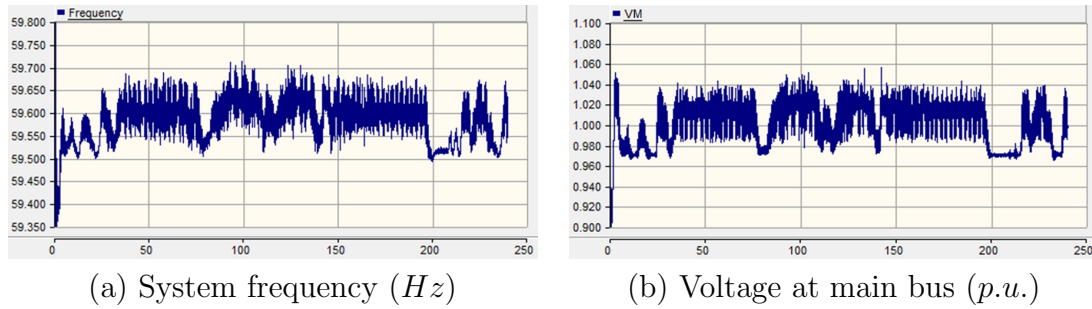


Figure 6.5: Waveforms of system voltage and frequency.

two generators. It is necessary to develop Power System Stabilizer (PSS) [58] for two generators in future to compensate these low frequency oscillations.

Simulation Results of Microgrid Transitions

The seamless transition management proposed in Chapter 4 is applied to FSMG. Two tests have been conducted. Figure 6.6 and 6.7 show a full microgrid operation from on-grid \Rightarrow intentional islanding \Rightarrow off-grid \Rightarrow re-synchronization \Rightarrow on-grid. Figure 6.8 and 6.9 show another case of microgrid operation from on-grid \Rightarrow unintentional islanding \Rightarrow off-grid \Rightarrow re-synchronization \Rightarrow on-grid.

1, 2, 3, and 4 in mode waveform represent for on-grid, islanding, off-grid, and re-connection respectively. From results, the microgrid has smooth transitions according to the change of operation.

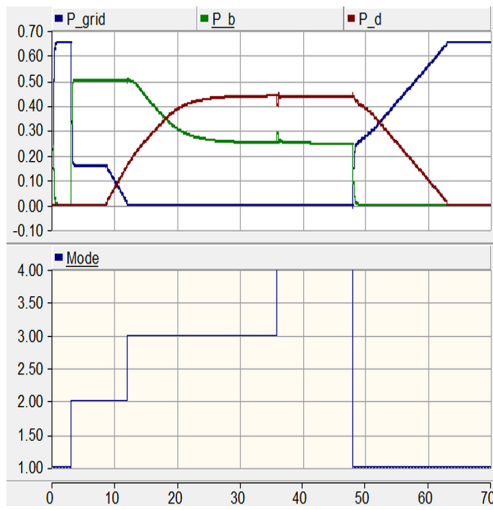


Figure 6.6: Real power delivered by grid, battery and natural gas generators (upper); Operation mode in case of intentional islanding (lower).

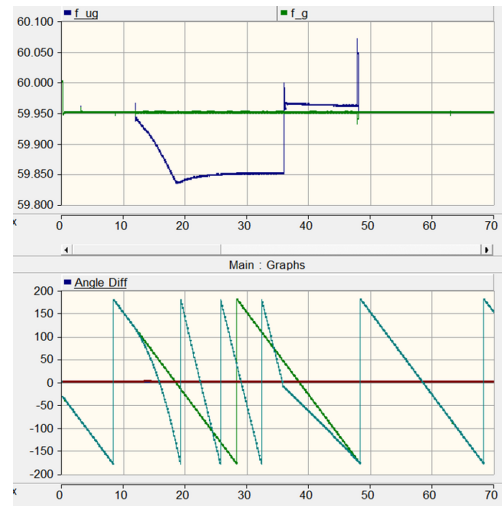


Figure 6.7: The microgrid and bulk grid frequencies (upper); Difference of instantaneous phase angles between left and right side of static switch (lower).

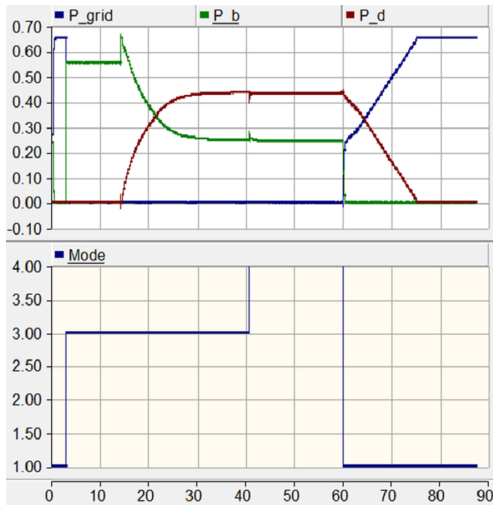


Figure 6.8: Real power delivered by grid, battery and natural gas generators (upper); Operation mode in case of unintentional islanding (lower).

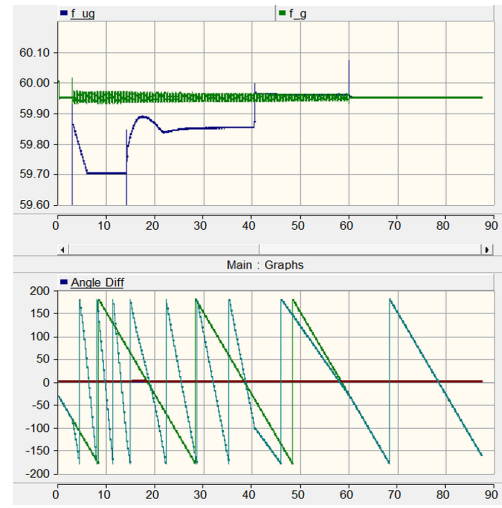


Figure 6.9: The microgrid and bulk grid frequencies (upper); Difference of instantaneous phase angles between left and right side of static switch (lower).

6.2 Modeling of Extended FSMG

FSMG represents the building 5900 which is connected to 13.2kV feeder via an AC Flex-Bus Inverter. There are other buildings and a 2 MW Waste Water Treatment Plant (WWTP) under 13.2kV substation. The whole system is illustrated in Figure 6.10, namely Extended Fort Sill Microgrid (EFSMG).

The main components of extended FSMG are listed in Table 6.2. The total nominal load is around 2MW. The power rating for Solar PV increases to 200kW which will be installed at the roof of building 5900. And a 100kW wind turbine will be added to the system about 1.5 miles away from the building.

Table 6.2: List of capacities of main components within EFSMG

Devices	Capacity
G1	410kW (0.8 P.F.)
G2	410kW (0.8 P.F.)
G3	350kW (0.8 P.F.)
G4	350kW (0.8 P.F.)
FSMG (Building 5900)	830kW (G) / 460kW (L)
Building 5970	300kW (Tentative)
Building 6050	300kW (Tentative)
Building 5950	300kW (Tentative)
Building 5960	300kW (Tentative)
Building 5800	300kW (Tentative)
Wind (1.5 miles away)	100kW
Natural Gas 1 (FSMG)	190kW (0.8 P.F.)
Natural Gas 2 (FSMG)	190kW (0.8 P.F.)
Storage System (FSMG)	250kW(cont.)/400kW(3 mins)
Wind (FSMG)	2.5kW
PV (FSMG)	200kW
AC Flex-Bus Inverter	600kVA / 300kVA

The AC flex-bus inverter is a key to operate EFSMG. It serves as a power coordinator between two AC networks. Its key features include 1) independently managing voltages, frequencies, and phase angles for two AC networks; 2) playing a role of a short-term storage to smooth power intermittencies caused by renewable energy or interruptible loads; 3) isolating two AC networks by transformers and DC-link and preventing fault current flowing from one side to the other side.

Several initial studies and tests have been conducted. Figure 6.11 - 6.13 show a case of islanding the 13.2kV feeder from upstream grid with opening power of 200kW. The EFSMG moves to droop control with 0.3% frequency dip. The power delivered by WWTP, FSMG and Grid before and after the island are listed in Table 6.3.

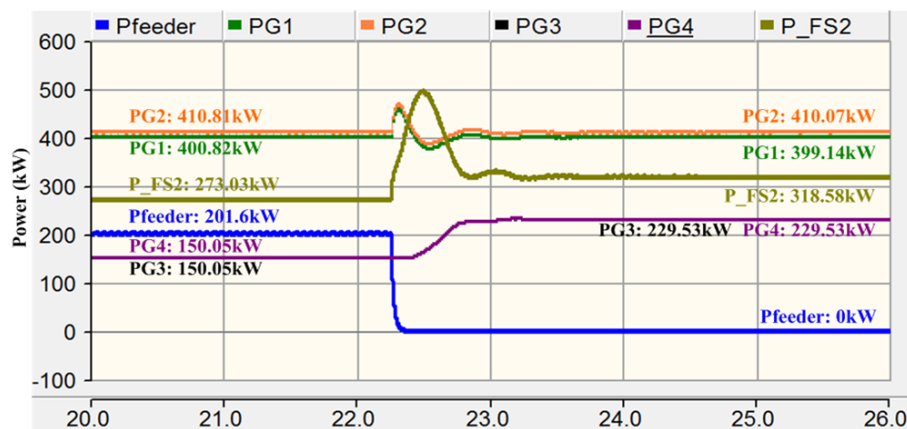


Figure 6.11: Power curves during islanding with 200kW opening power.

Figure 6.14 - 6.16 show a case of islanding the 13.2kV feeder from upstream grid with opening power of 550kW. Before islanding, FSMG providing 66.9kW because of low load condition. The EFSMG moves to island management with 0.65% frequency

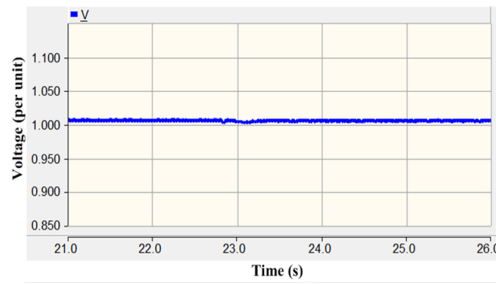


Figure 6.12: Voltage at 13.2kV feeder.

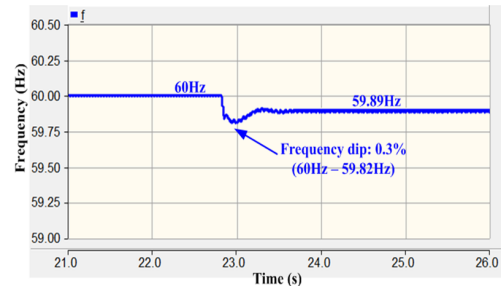


Figure 6.13: System frequency.

Table 6.3: Power delivered by WWTP, FSMG and Grid before and after islanding

Gen	Before	After
G1	401kW	399kW
G2	411kW	410kW
G3	150kW	230kW
G4	150kW	230kW
FSMG	273kW	319kW
Grid	202kW	0kW
Total	1587kW	1588kW

dip. The power delivered by WWTP, FSMG and Grid before and after the island are listed in Table 6.4.

Table 6.4: Power delivered by WWTP, FSMG and Grid before and after islanding

Gen	Before	After
G1	400kW	400kW
G2	410kW	410kW
G3	150kW	280kW
G4	150kW	280kW
FSMG	-67kW	219kW
Grid	544kW	0kW
Total	1587kW	1589kW

A step load test in island mode is conducted to illustrate how AC flex-bus inverter reacts. Figure 6.18 shows simulation result of two step load within FSMG. The Load

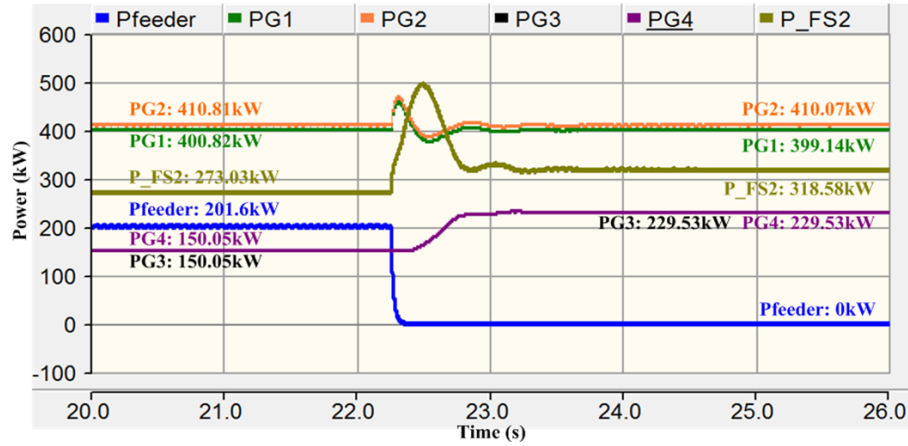


Figure 6.14: Power curves during islanding with 550kW opening power.

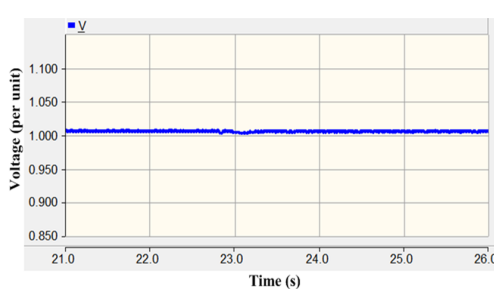


Figure 6.15: Voltage at 13.2kV feeder.

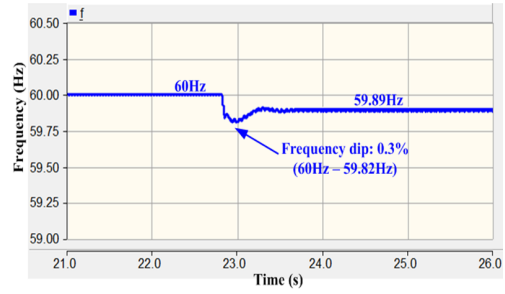


Figure 6.16: System frequency.

level is changing from 150.8kW to 452.1kW around 35 second and to 602kW as peak load around 39 second. The power delivered from AC Flex-bus inverter named as P_FS2 to other buildings doesn't change after first load step, because the generations within FSMG are able to provide up to 800kW. When the local load raises to 602kW, the output of AC Flex-bus inverter has to drop to avoid overload issue.

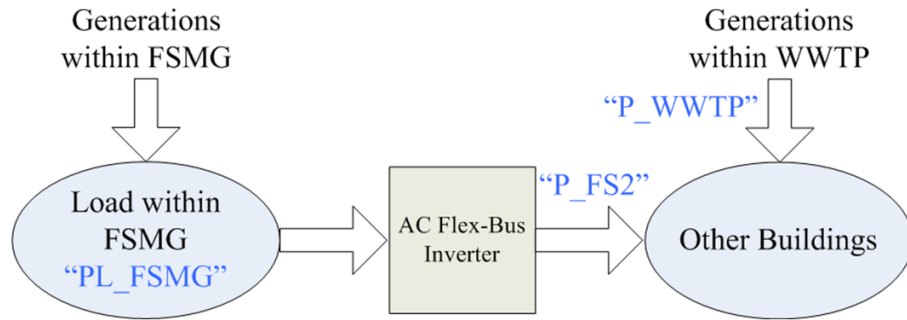


Figure 6.17: Diagram of power flow between FSMG and WWTP via AC flex-bus inverter.

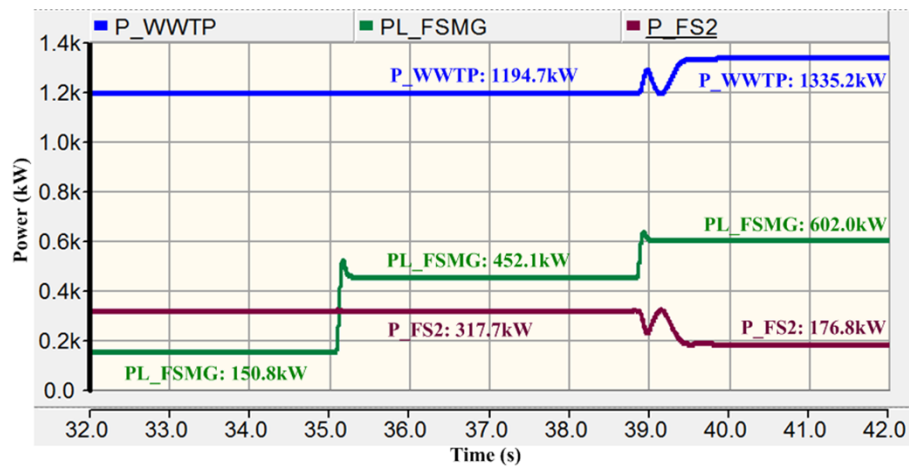


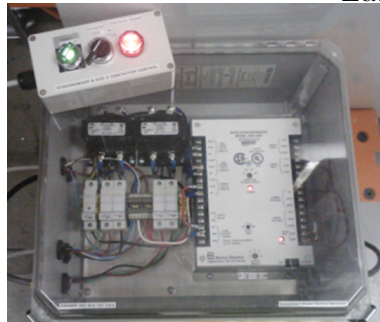
Figure 6.18: Real power delivered by AC flex-bus inverter and WWTP, and local load within FSMG.

6.3 Testing of A 1MW Multi-Inverter Based Microgrid

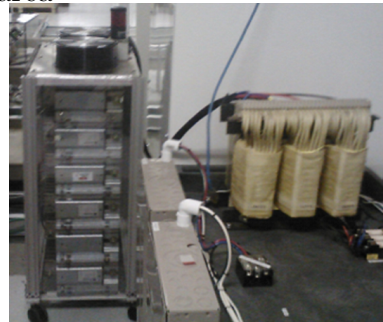
A multi-inverter based 1MW microgrid has been built at Eaton's Power Lab. Several experiments have been conducted to test and verify the algorithms proposed in chapter 4. The schematic of the setup is shown in Figure 6.20 and pictures of the lab area, synchronizer and passive loads are shown in Figure 6.19. The system includes three 250kW, 480V inverter based sources, passive loads, grid synchronizer and grid connection. The switching frequency of the inverters is at 3kHz. Two inverter-based energy storage emulators are built to provide DC voltage at 250kW for the inverters. Inverter 1 models a renewable source, inverter 2 models the energy storage device, and inverter 3 models the natural gas generator. The block diagram of Figure 4.39 has been implemented for the energy storage inverter. The storage inverter adjusts its output current in maximum five switching periods (1.67 ms). Similar dynamic response is applied for inverter 1 emulating a renewable source. The SCU is a computer, which communicates with inverters through Mod BUS and provides active and reactive power commands. The control diagrams of Figures 4.39 and 4.40 are built in the inverters and techniques for transition managements are implemented in the computer.



Lab area



Synchronizer



Passive loads

Figure 6.19: A picture of the test setup, synchronizer and passive loads for the experimental setup.

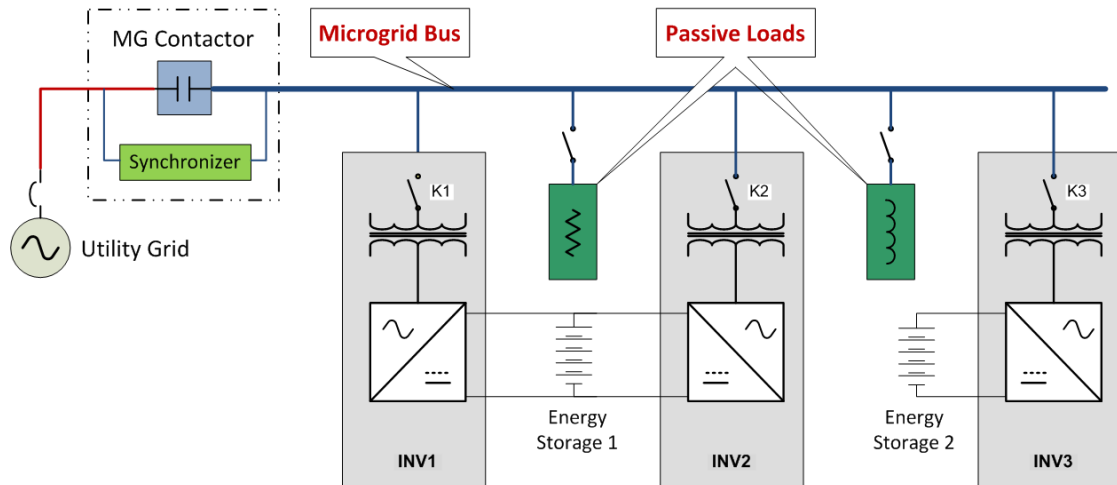


Figure 6.20: The schematic of the experimental test setup.

Figure 6.21 shows the waveforms of the voltage, frequency and output power of two inverters when the system transitions from grid-tie mode to off-grid. Inverter 1 is in current mode and its output power remains constant during both modes. Inverter 2 is in voltage mode and its power changes from 15kW to 35kW. During transition, the frequency drops to 59.35Hz before recovering to 59.85Hz in island mode. Figure 6.22 shows the instantaneous waveforms of load and grid currents, as well as the microgrid and grid voltages. As we can see, the load current (red) remain constant during transition, while the current from the grid (light blue) goes to zero when the contactor is opened. Voltages of the grid and microgrid become asynchronous after islanding occurs because they have different frequencies. Since the storage operates in voltage mode in both grid tie and island modes, the load does not experience significant voltage transients.

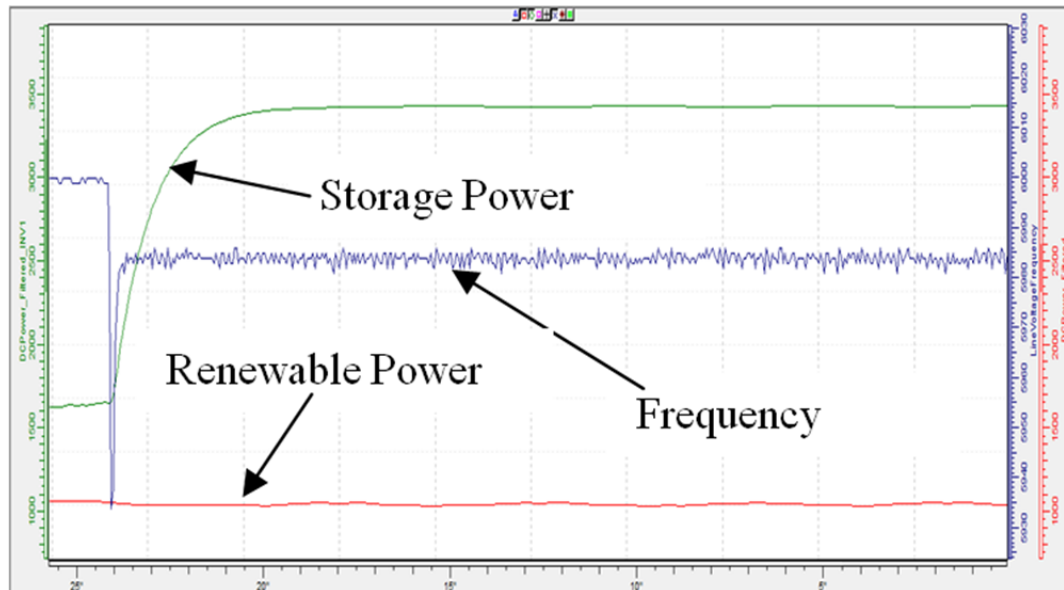


Figure 6.21: Traces of microgrid frequency and output power of energy storage and renewable during unintentional islanding when transitioning from grid-tie to island mode.

Figure 6.23 shows the system starting in black start and then moving to island mode and reconnection to the grid. The waveforms of the voltage, frequency and output power of emulators for storage inverter and natural gas generator are provided. The energy storage device starts the system and establishes voltage and frequency reference. Then, the natural gas generator is synchronized and provides power. When the system moves to grid-tie mode, the generator power is reduced to zero and the storage inverter is charging the storage with 20kW according to the power settings.

Figure 6.24 shows the waveforms of system voltage and frequency when the microgrid is again started from zero voltage (black start) and operated in an island mode. The traces for energy storage and NG generator emulator power are also

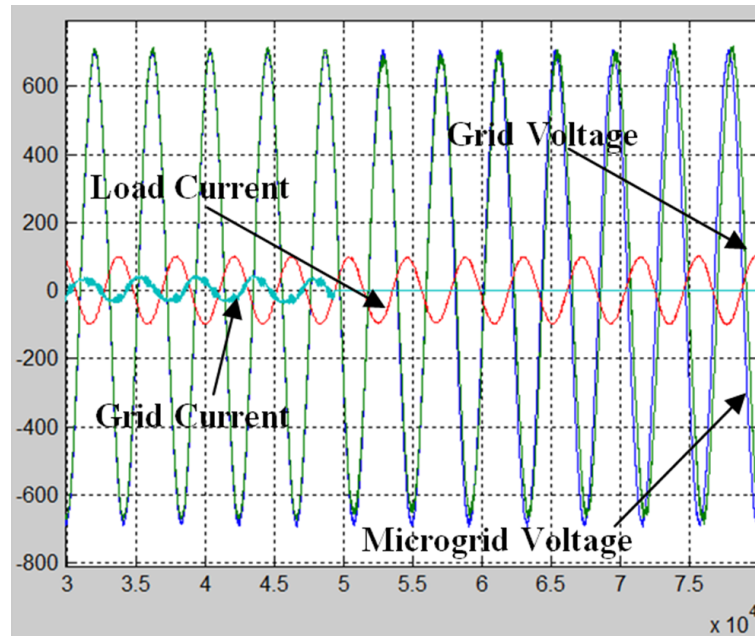


Figure 6.22: Instantaneous waveforms for voltage, load current (red), and grid current (light blue) during unintentional islanding.

shown. Initially the energy storage provides power to the load and then NG generator is synchronized to support. Several step loading and unloading are applied. The system adjusts the power of the energy storage and NG generator according to the droop settings.

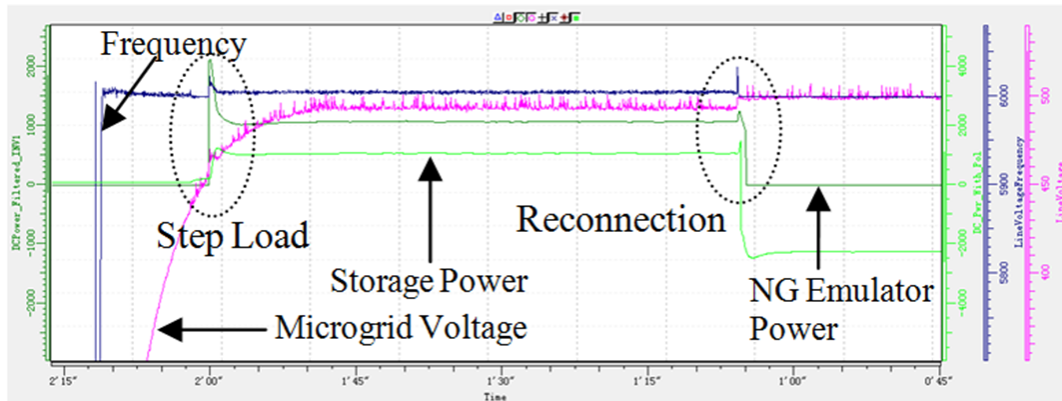


Figure 6.23: Traces of microgrid voltage, frequency, and generator and storage power in black start moving to island and grid tie modes.

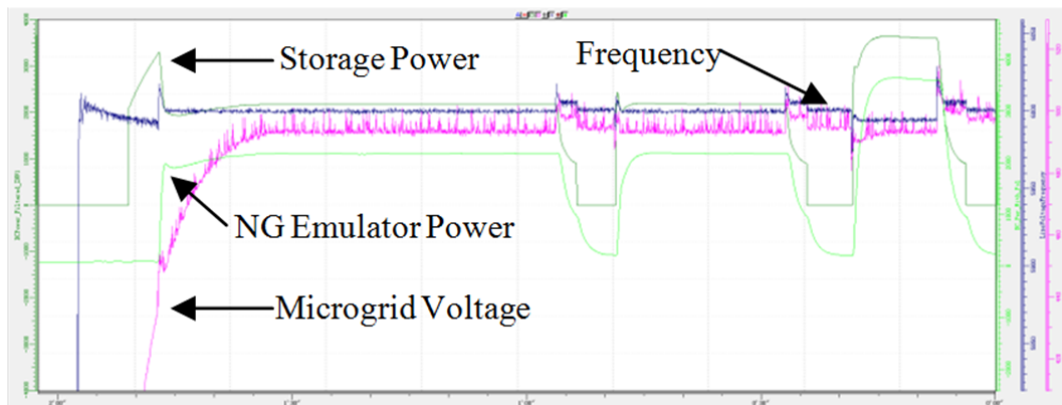


Figure 6.24: Microgrid operation from black start to island mode under step loading conditions.

Chapter 7

Conclusion

In this paper, a general-purpose microgrid modified by IEEE 34-Bus distribution system is modeled, analyzed and evaluated. To sum up, the following conclusions can be drawn from this thesis:

The modification and scaling of IEEE 34-bus distribution system is presented. The configuration of the proposed microgrid, the measured daily power profiles for generations and loads and their capacity sizing issues are discussed and analyzed.

Average and detailed models for the sources have been implemented to run the whole system using PSCAD software for 24 hours. Control techniques have been introduced to control the active/reactive power of the renewable sources, natural gas generator, and energy storage inverters in order to minimize the transients. Detailed modeling results have been presented and confirmed on a multi-inverter based experimental test setup.

The power management for renewable energies and the power constraints applied

to the control of renewable energies are proposed. A comprehensive supervisory control scheme is proposed and developed for microgrid operation and management. The autonomous control and droop control for microgrid operation in grid-tied mode and islanded mode are presented. A collapse case of island operation is discussed and solved. The transition management for microgrids between various modes of operation including islanding, reconnection, and black start are presented. Two extreme cases are discussed and tested for intentional/unintentional islanding. The shifting droop control is proposed and developed for microgrid reconnection. A compact data format considering low bandwidth communication is also proposed and used for the control commands sent by supervisory control unit to generations.

The power quality of the proposed microgrid is evaluated by calculating the indexes in different cases. A novel probabilistic assessment approach is proposed to evaluate microgrid reliability. The data based method and model based method are proposed and compared.

Some extended researches based on the algorithms and techniques proposed in the thesis are presented at last. An in-building Fort Sill Microgrid is modeled and studied. The concept of AC Flex-bus inverter is introduced. A 1MW multi-inverter based microgrid experimental test setup is established at EATON power lab. Several experiments including microgrid transitions have been conducted and presented in the thesis.

References

- [1] F. Blaabjerg, Z. Chen, and S. B. Kjaer. "Power electronics as efficient interface in dispersed power generation systems". *IEEE Transactions On Power Electronics*, 19(5):1184 – 1194, 2004.
- [2] T. Degner, J. Schmid, and P. Strauss. "*Distributed Generation With High Penetration of Renewable Energy Sources Final Public Report of Dispower Project*". ISBN 3-00-016584-3, 2006.
- [3] "AWEA US wind industry annual market report year ending 2010". Available: <http://awea.org>.
- [4] U.S. Department of Energy. "20% Wind Energy by 2030. Increasing Wind Energy's Contribution to U.S. Electricity.
- [5] American Wind Energy Association. "U.S. Wind Industry: Market Update". Available: <http://awea.org>.
- [6] L. Sherwood. "U.S. solar market trends, 2010", Integrated Renewable Energy Council, Jun 2011.
- [7] American Council of Civil Engineers. "2013 Report Card for America's Infrastructure". Available: <http://www.infrastructurereportcard.org/>.

- [8] J. Huang, C. Jiang, and R. Xu. "A review on distributed energy resources and microgrid". *Renewable Sustainable Energy Rev.*, 12(9):2472 – 2483, 2008.
- [9] N. Saito, T. Niimura, K. Koyanagi, and R. Yokoyama. "Trade-off analysis of autonomous microgrid sizing with pv, diesel, and battery storage". In *Proc. IEEE Power Energy Soc. Gen. Meet*, 2009.
- [10] R. H. Lasseter and P. Paigi. "Microgrid: a conceptual solution". In *Proc. Power Electronics Specialist Conference*, volume 6, pages 4285 – 4290, 2004.
- [11] P. Paigi and R. H. Lasseter. "Autonomous control of microgrids". In *Proc. IEEE Power Energy Soc. Gen. Meet*, 2006.
- [12] J. Eto, R. Lasseter, B. Schenkman, J. Stevens, D. Klapp, H. Volkommer, E. Linton, H. Hurtado, and R. Roy. "Overview of the certs microgrid laboratory test bed". In *CIGRE/IEEE PES Joint Symposium Integration of Wide-Scale Renewable Resources Into the Power Delivery System*, 2009.
- [13] R. H. Lasseter. "Extended CERTS microgrid". In *Proc. IEEE Power Energy Soc. Gen. Meet - Conversion and Delivery of Electrical Energy in the 21st Century*, pages 1–5, 2008.
- [14] C. Marnay, H. Asano, S. Papathanassiou, and G. Strbac. "Policymaking for microgrids". *IEEE Power and Energy Magazine*, 6(3):66 – 77, 2008.
- [15] C. L. Moreira and Pecas Lopes J. A. "MicroGrids dynamic security assessment". In *International Conference on Clean Electrical Power*, pages 26 – 32, 2007.
- [16] M. D. Johnson and R. A. Ducey. "Overview of U.S. Army microgrid efforts at fixed installations". In *Proc. IEEE Power Energy Soc. Gen. Meet*, pages 1 – 2, 2011.

- [17] A. K. Basu, S. Chowdhury, and S. P. Chowdhury. "Strategic deployment of CHP-based distributed energy resources in microgrids". In *Proc. IEEE Power Energy Soc. Gen. Meet*, pages 1 – 6, 2009.
- [18] P. Agrawal. "Overview of DOE Microgrid Activities", June 2006.
- [19] M. P. Razanousky. "MICROGRIDS: an assessment of the value, opportunities and barriers to deployment in new york state", Available at: www.nyserda.ny.gov.
- [20] King D. E. "The regulatory environment for interconnected electric power micro-grids: insights from state regulatory officials". In *Carnegie Mellon Electricity Industry Center Working Paper CEIC-05-08*, Available at: www.cmu.edu/electricity.
- [21] C. Marnay, N. DeForest, and J. Lai. "A green prison: The santa rita jail campus microgrid". In *Proc. IEEE Power Energy Soc. Gen. Meet*, pages 22 – 26, 2012.
- [22] J. Stamp. "SPIDERS: Smart power infrastructure demonstration for energy, reliability, and security". In *Advanced Microgrid Concepts and Technologies Workshop*, 2012.
- [23] US Army Installation Management Energy Portfolio. http://armyenergy.hqda.pentagon.mil/docs/energy_portfolio_15_sep_10.pdf, retrieved on oct 15, 2012.
- [24] J. Kelly and D. V. Dollen. "The Illinois Institute of Technology's Perfect Power System Prototype". In *Advanced Microgrid Concepts and Technologies Workshop*, 2007.
- [25] C. Ma and Y. Hou. "Classified overview of microgrids and developments in china". In *IE Conference & EXPO*, 2012.

- [26] J. Y. Kim, J. H. Jeon, S. K. Kim, and S. M. Kwon. "Test result of microgrid management function in keri pilot plant". In *IEEE International Conference Power Electronics and ECCE Asia*, pages 825 – 832, 2011.
- [27] K. Yukita, K. Ban, Y. Goto, K. Ichiyanagi, K. Hirose, T. Ushirokawa, Y. Okui, and H. Takabayashi. "Power supply system of dc/ac micro grid system". In *IEEE International Conference Power Electronics and ECCE Asia*, pages 228 – 234, 2011.
- [28] N.W.A. Lidula and A. D. Rajapakse. "Microgrids research: A review of experimental microgrids and test systems". In *Int. J. Renewable and Sustainable Energy Reviews*, volume 15, pages 186 – 202, 2011.
- [29] R.C. Dugan and W. H. Kersting. "Induction machine test case for the 34-bus test feeder description". In *IEEE Proc. on Power Engineering Society General Meeting*, 2006.
- [30] N. Samaan, T. McDermott, B. Zavadil, and J. Li. "Induction machine test case for the 34-bus test feeder - steady state and dynamic solutions". In *IEEE Proc. on Power Engineering Society General Meeting*, 2006.
- [31] Power Systems Test Case Archive, Available at: <http://www.ee.washington.edu/research/pstca>.
- [32] E. Manla, A. Nasiri, C.H. Rentel, and M. Hughes. "Modeling of Zinc Bromide Energy Storage for Vehicular Applications". *Industrial Electronics, IEEE Transactions on*, 57(2):624 – 632, Feb 2010.
- [33] A. Esmaili and A. Nasiri. "Energy storage for short-term and long-term wind energy support". In *IEEE Proc. on IECON*, 2010.
- [34] Annual Energy Outlook 2011. Energy Information Administration, Available at: <http://www.eia.doe.gov/oiaf/aeo/index.html>.

- [35] V. Bhavaraju, A. Nasiri, and Q. Fu. "Multi-Inverter Controls and Management of Energy Storage for Microgrid Islanding". *The Electricity Journal*, 25(8):36 – 44, Oct 2012.
- [36] A.M. Hava, U. Ayhan, and V.V. Aban. "A DC bus capacitor design method for various inverter applications". In *Energy Conversion Congress and Exposition (ECCE), 2012 IEEE Conference on*, pages 4592 – 4599, Sept 2012.
- [37] Z. Ye, R. Walling, N. Miller, P. Du, and K. Nelson. "Facility Microgrid", May 2005. Available at: www.nrel.gov/docs/fy05osti/38019.pdf.
- [38] Q. Fu, L. F. Montoya, A. Solanki, A. Nasiri, V. Bhavaraju, T. Abdallah, and D. C. Yu. "Microgrid Generation Capacity Design with Renewable and Energy Storage Addressing Power Quality and Surety". *Smart Grid, IEEE Transactions on*, 3:2019–2027, 2012.
- [39] S. Mandal and A. Pahwa. "Optimal selection of conductors for distribution feeders". *IEEE Trans. on Power Systems*, 17(1):192 – 197, Feb 2002.
- [40] R. E. Brown, S. Gupta, R. D. Christie, S. S. Venkata, and R. D. Fletcher. "Automated primary distribution system design: reliability and cost optimization". *IEEE Trans. on Power Delivery*, 12(2):1017 – 1022, Apr 1997.
- [41] H. L. Willis. "*Power Distribution Planning Reference Book*".
- [42] D. A. Kowalewski. "A comparable method for benchmarking the reliability performance of electric utilities". In *Proc. IEEE Power Engineering Society Summer Power Meeting*, pages 646 – 649, July 2002.
- [43] S. Knezevic, D. Skrlec, and M. Skok. "The impact of reliability indices in the process of planning radial distribution networks". In *Proc. International Conference on Using a Computer as a Tool*, pages 244 – 248, Sept 2003.

- [44] H. Falaghi and M-R. Haghifam. "Distributed generation impacts on electric distribution systems reliability: sensitivity analysis". In *Proc. International Conference on Using a Computer as a Tool*, pages 1465 – 1468, Nov 2005.
- [45] N. Balijepalli, S. S. Venkata, and R. D. Christie. "Modeling and analysis of distribution reliability indices". *IEEE Trans. on Power Delivery*, 19(4):1950 – 1955, Oct 2004.
- [46] E. Carpaneto, A. Mosso, A. Ponta, and E. Roggero. "Comparison of reliability and availability evaluation techniques for distribution network systems". In *Proc. Annual Reliability and Maintainability Symposium*, pages 563 – 568, Jan 2002.
- [47] H. Herath, V. Gosbell, and S. Perera. "Power quality (PQ) survey reporting: discrete disturbance limits". *IEEE Trans. on Power Delivery*, 20(2):851 – 858, Apr 2005.
- [48] Horak J. "Power quality: measurements of sags and interruptions". In *Proc. IEEE Transmission and Distribution Conference*, pages 733 – 739, May 2006.
- [49] C. Su. "a new probabilistic load flow method". In *IEEE Power Engineering Society General Meeting*, pages 389 – 394, July 2005.
- [50] B. Borkowska. "Probabilistic load flow". *IEEE Trans. on Power Apparatus and Systems*, 93:752 – 759, 1974.
- [51] J. Usaola. "Probabilistic load flow with wind production uncertainty using cumulants and cornish-fisher expansion". In *Power Systems Computation Conference (PSCC)*, pages 474 – 481, Oct 2008.
- [52] X Li, J. Pei, and S. Zhang. "A probabilistic wind farm model for probabilistic load flow calculation". In *IEEE Power and Energy Engineering Conference (APPEEC)*, pages 1 – 4, 2010.

- [53] C. Su. "Probabilistic load-flow computation using point estimate method". *IEEE Trans. on Power Systems*, 20(4):1843 – 1851, 2005.
- [54] D. Outcalt. "Probabilistic load flow for a system with high wind penetration based on a 3-point estimation method". In *Wind power Conference*, 2008.
- [55] D. Outcalt. "*Probabilistic load flow for high wind penetrated power systems based on a five point estimation method*". PhD thesis, University of Wisconsin - Milwaukee, Department of Electrical Engineering, 2009.
- [56] S. Blinnikov and R. Moessner. "Expansions for nearly gaussian distributions". *Astronomy & Astrophysics Supplement Series*, 130(1):193 – 205, 1998.
- [57] C. Genest and J. MacKay. "The joy of copulas: Bivariate distributions with uniform marginals". *The American Statistician*, 40(1):280 – 283, 1986.
- [58] W Zhang, F. Xu, W. Hu, M. Li, W. Ge, and Z. Wang. "Research of coordination control system between nonlinear robust excitation control and governor power system stabilizer in multi-machine power system". In *IEEE Proc. on Power System Technology*, pages 1–5, 2012.

Curriculum Vitae

Qiang Fu, Ph.D. Candidate

Department of Engineering, University of Wisconsin-Milwaukee

EDUCATION

Ph.D. - Electrical Engineering August 2013

University of Wisconsin - Milwaukee

Dissertation: Modeling, Analyses and Assessment of Microgrds
Considering High Renewable Energy Penetration

Major advisor: Dr. David C. Yu

Co-advisor: Dr. Adel Nasiri and Dr. Vijay Bhavaraju

Master of Science - Power Electronics June 2009

Chongqing University, China

Dissertation: Research of Sensorless PMSM Control Based on
Sliding Mode Observer for Automobile Air-conditioner

Advisor: Dr. Heping Liu

Bachelor of Science - Electrical Engineering June 2006

Chongqing University, China

Dissertation: Research on One Cycle Control Three-level
Single Phase Power Factor Correction

Advisor: Dr. Luowei Chow

ACADEMIC EXPERIENCE

Fort Sill Microgrid

1MW Multi-Inverter Based Microgrid

IGBT Reliability in High Junction Temperature

Probabilistic Load Flow for Power System Planning

2kW PMSM drive for the application of vehicle air-conditioner

20kW BLDC drive for an electric golf cart

EMPLOYMENT

Research Assistant	2009.09 - 2013.08
University of Wisconsin - Milwaukee, Milwaukee, WI	
Software Engineer	2012.05 - 2012.08
Eaton Corp. Innovation Center - Milwaukee, WI	
Hardware Engineer	2011.05 - 2011.08
Rockwell Automation - Mequon, WI	

SELECTED PUBLICATIONS

Q. Fu, A. Nasiri, V. Bhavaraju, T. Abdallah, D. C. Yu, "Microgrid Generation Capacity Design With Renewable and Energy Storage Addressing Power Quality and Surety," IEEE Trans. Smart Grid, vol. 4, pp. 2019-2027, 2012.

Q. Fu, A. Solanki, L. F. Montoya, A. Nasiri, V. Bhavaraju, and D. Yu, "Transition Management of Microgrids with High Penetration of Renewable Energy", IEEE Transaction On Smart Grid.

V. Bhavaraju, A. Nasiri, Q. Fu "Multi-Inverter Controls and Management of Energy Storage for Microgrid Islanding", Electricity Journal, vol. 25, pp. 36-44, 2012.

H. Liu, P. Liu, Y. Hu, Q. Fu, "Control Scheme of Bi-Directional Z-Source Inverter in Improving the Dynamic Performance of Electrical Vehicles", Transactions of China Electrotechnical Society, 27(02), pp. 139-145, 2012.

H. Liu, P. Liu, Q. Guo, Q. Fu, "Effects of battery direct power supply on driving performance of electric vehicles", Electric Machines and Control , 15(11), pp. 27-32, 2011.

Q. Fu, D. C. Yu, J. Ghorai, "Probabilistic Load Flow Analysis for Power Systems with Multi-correlated Wind Sources", in Proc. IEEE Power & Energy Society General Meeting, 2011, Detroit, MI.

Q. Fu, H. Liu, Y. Chen, "Research on Sensorless PMSM Control with Sliding Mode Observer for Vehicle Air-condition Based on Freescale DSP 56F8346", Micromotors, 43(04), pp. 56-59, 2010.